THESE de DOCTORAT DE l' INSA Lyon
membre de l'Université de Lyon

Ecole Doctorale N° EDA162
Mécanique, Energétique, Génie Civil, Acoustique

Spécialité/ discipline de doctorat : Génie Mécanique

Soutenue publiquement le 16 décembre 2022, par :
Julien CHAPELAT

Optimisation de forme multi-critère d'une structure non-linéaire complexe

Devant le jury composé de :

Moës, Nicolas	PR	Ecole Centrale de Nantes	Rapporteur
Jouve, François	PR	Université Paris Diderot	Rapporteur
Lleras, Vanessa	MCF	Université de Montpellier 2	Examinatrice
Bonnetier, Eric	PR	Université Grenoble-Alpes	Examinateur
Bretin, Elie	MCF, HDR.	INSA Lyon	Directeur de thèse
Renard, Yves	PR	INSA Lyon	Directeur de thèse
Homolle, Thomas	Ingénieur	MFP MICHELIN	Invité
Douanla-L., Charlie	Docteur	MFP MICHELIN	Invité

Département FEDORA – INSA Lyon - Ecoles Doctorales

SIGLE	ECOLE DOCTORALE	NOM ET COORDONNEES DU RESPONSABLE
CHIMIE	**CHIMIE DE LYON** https://www.edchimie-lyon.fr Sec. : Renée EL MELHEM Bât. Blaise PASCAL, 3e étage secretariat@edchimie-lyon.fr	**M. Stéphane DANIELE** C2P2-CPE LYON-UMR 5265 Bâtiment F308, BP 2077 43 Boulevard du 11 novembre 1918 69616 Villeurbanne directeur@edchimie-lyon.fr
E.E.A.	**ÉLECTRONIQUE, ÉLECTROTECHNIQUE, AUTOMATIQUE** https://edeea.universite-lyon.fr Sec. : Stéphanie CAUVIN Bâtiment Direction INSA Lyon Tél : 04.72.43.71.70 secretariat.edeea@insa-lyon.fr	**M. Philippe DELACHARTRE** INSA LYON Laboratoire CREATIS Bâtiment Blaise Pascal, 7 avenue Jean Capelle 69621 Villeurbanne CEDEX Tél : 04.72.43.88.63 philippe.delachartre@insa-lyon.fr
E2M2	**ÉVOLUTION, ÉCOSYSTÈME, MICROBIOLOGIE, MODÉLISATION** http://e2m2.universite-lyon.fr Sec. : Bénédicte LANZA Bât. Atrium, UCB Lyon 1 Tél : 04.72.44.83.62 secretariat.e2m2@univ-lyon1.fr	**Mme Sandrine CHARLES** Université Claude Bernard Lyon 1 UFR Biosciences Bâtiment Mendel 43, boulevard du 11 Novembre 1918 69622 Villeurbanne CEDEX sandrine.charles@univ-lyon1.fr
EDISS	**INTERDISCIPLINAIRE SCIENCES-SANTÉ** http://ediss.universite-lyon.fr Sec. : Bénédicte LANZA Bât. Atrium, UCB Lyon 1 Tél : 04.72.44.83.62 secretariat.ediss@univ-lyon1.fr	**Mme Sylvie RICARD-BLUM** Institut de Chimie et Biochimie Moléculaires et Supramoléculaires (ICBMS) - UMR 5246 CNRS - Université Lyon 1 Bâtiment Raulin - 2ème étage Nord 43 Boulevard du 11 novembre 1918 69622 Villeurbanne Cedex Tél : +33(0)4 72 44 82 32 sylvie.ricard-blum@univ-lyon1.fr
INFOMATHS	**INFORMATIQUE ET MATHÉMATIQUES** http://edinfomaths.universite-lyon.fr Sec. : Renée EL MELHEM Bât. Blaise PASCAL, 3e étage Tél : 04.72.43.80.46 infomaths@univ-lyon1.fr	**M. Hamamache KHEDDOUCI** Université Claude Bernard Lyon 1 Bât. Nautibus 43, Boulevard du 11 novembre 1918 69 622 Villeurbanne Cedex France Tél : 04.72.44.83.69 hamamache.kheddouci@univ-lyon1.fr
Matériaux	**MATÉRIAUX DE LYON** http://ed34.universite-lyon.fr Sec. : Yann DE ORDENANA Tél : 04.72.18.62.44 yann.de-ordenana@ec-lyon.fr	**M. Stéphane BENAYOUN** Ecole Centrale de Lyon Laboratoire LTDS 36 avenue Guy de Collongue 69134 Ecully CEDEX Tél : 04.72.18.64.37 stephane.benayoun@ec-lyon.fr
MEGA	**MÉCANIQUE, ÉNERGÉTIQUE, GÉNIE CIVIL, ACOUSTIQUE** http://edmega.universite-lyon.fr Sec. : Stéphanie CAUVIN Tél : 04.72.43.71.70 Bâtiment Direction INSA Lyon mega@insa-lyon.fr	**M. Jocelyn BONJOUR** INSA Lyon Laboratoire CETHIL Bâtiment Sadi-Carnot 9, rue de la Physique 69621 Villeurbanne CEDEX jocelyn.bonjour@insa-lyon.fr
ScSo	**ScSo*** https://edsciencessociales.universite-lyon.fr Sec. : Mélina FAVETON INSA : J.Y. TOUSSAINT Tél : 04.78.69.77.79 melina.faveton@univ-lyon2.fr	**M. Christian MONTES** Université Lumière Lyon 2 86 Rue Pasteur 69365 Lyon CEDEX 07 christian.montes@univ-lyon2.fr

*ScSo : Histoire, Géographie, Aménagement, Urbanisme, Archéologie, Science politique, Sociologie, Anthropologie

Abstract

Airless tyres are complex structures working in multi-physic contexts. The geometry and the combination of materials must be wisely chosen to manufacture competitive designs. Multiple innovations were proposed at different scales, from the micro-scale concerning the grip of the tread and the thermal response in the contact zone with the ground to the meter-scale concerning the global architecture of the airless tyre, with structural, vibratory challenges. At the latter macro-scale, designers particularly focus on the elastic response of the structure to correctly guide a vehicle towards its trajectory. Different tools based on several optimization methods exist to assist manufacturers reaching the optimal geometry responding to the best comprise of performances.

In our special case, we develop the geometric shape optimization in an elastic mechanical context. We propose a gradient method to minimize optimization criteria. Yet multiple aspects lead the optimization complex, such as non linearities. We develop the complexity linked to the contact condition between the airless tyre and the ground. The contact condition involves non linearities in the mechanical problem. The contact is treated by Nitsche's method, which is a consistent method and does not need the use of Lagrangian multipliers. Therefore we study geometric shape optimization with contact through a Nitsche-based formulation in elasticity. The contact condition also introduces a non differentiability in the usual sense through the optimization problem. A weaker notion of differentiability is introduced to ensure the formulation of shape derivatives of the optimization criteria. In addition, the airless tyre is largely solicited and high deformations might occur, involving other non linearities in the mechanical problem. Thereby the shape optimization procedure is first presented in linear elasticity where the mathematical framework offers the possibility to analyze the shape sensitivity and ensure shape derivatives for the criteria for the gradient descent method. Then the shape optimization is extended to large deformations for more realistic applications.

Résumé

Les pneumatiques sans air sont des structures complexes dont le comportement fait intervenir différentes physiques. Afin de proposer une conception performante, la géométrie d'un pneumatique sans air et les matériaux qui composent une telle structure font l'objet de choix de recherche rigoureux. Différentes innovations ont marqué l'histoire du pneumatique, et ce à différentes échelles : de l'échelle microscopique concernant l'adhérence et la réponse thermique de la bande de roulement à une échelle macroscopique concernant la réponse vibratoire et mécanique de la structure. A cette dernière macro-échelle, les concepteurs ont particulièrement étudié la réponse élastique du pneumatique sans air pour guider au mieux le véhicule le long de sa trajectoire. Différents outils de conception existent afin d'obtenir le meilleur compromis de performances, et en particulier, des stratégies d'optimisation de forme.

Dans notre cas particulier, nous développons l'optimisation de forme dite géométrique dans le contexte de l'élasticité. Nous proposons une méthode de gradient afin de minimiser des critères de performance. Cependant, différents aspects peuvent faire rendre l'optimisation difficile comme par exemple des non linéarités. Nous développons la complexité liée à la condition de contact entre le pneumatique sans air et le sol. En effet, cette condition introduit une non linéarité dans le problème mécanique. Le contact est approximé par la méthode de Nitsche, méthode consistante et qui ne nécessite pas l'ajout de multiplicateurs de Lagrange. Ainsi, nous étudions l'optimisation de forme géométrique à travers une formulation du problème élastique utilisant la méthode de Nitsche. La condition de contact introduit également une non différentiabilité au sens classique dans le problème d'optimisation. Une notion plus faible de la différentiabilité permet d'assurer la formulation de dérivées de forme des critères d'optimisation, et ainsi d'assurer le bon fonctionnement de la méthode de gradient. Par ailleurs, le pneumatique sans air est largement sollicité en grandes déformations, ce qui introduit de nouvelles non linéarités. Ainsi la stratégie d'optimisation de forme est présentée d'abord dans le cadre de l'élasticité linéaire afin de présenter les outils mis en place et d'analyser la sensibilité de forme permettant d'assurer l'existence de dérivées de forme. Ensuite l'étude de forme est étendue aux grandes déformations pour traiter des applications plus réalistes.

Acknowledments

Contents

List of Figures

List of Tables

Résumé étendu

Motivations et applications

Introduction

La conception d'une structure pneumatique nécessite un savoir-faire multidisciplinaire pour répondre aux différentes performances attendues, tout en assurant le meilleur compromis en terme de masse et d'énergie dépensée. La structure pneumatique fait l'objet d'une somme d'exigences capitales afin d'assurer ces fonctions principales que sont :

- Porter la charge du véhicule (effort normal au sol).

- Transmettre les efforts longitudinaux, dans la direction instantanée d'avancement du pneumatique prise dans le plan du sol, tout en assurant l'adhérence avec ce même sol et donc permettre l'accélération et le freinage du véhicule.

- Guider le véhicule afin de permettre de suivre une trajectoire assurant la transmission des efforts transversaux (toujours dans le plan du sol) par adhérence au sol.

- Rouler afin de permettre l'avancement du véhicule en limitant la résistance au roulement.

- Absorber les différentes perturbations d'efforts et ainsi assurer un confort aux passagers du véhicule par une fonction d'amortissement et également limiter le bruit aérien.

- Durer un temps d'utilisation le plus long possible tout en garantissant les autres fonctions à un niveau acceptable, en exigeant le meilleur niveau en terme d'usure et d'endurance.

Ces différentes propriétés se traduisent par des critères de "performances" et peuvent être antagonistes. Parmi ces performances, on peut notamment citer : longévité et endurance, faible contribution à la consommation du véhicule, adhérence en toutes conditions d'utilisation, agrément de conduite, bruit aérien, moindre consommation de matières premières et d'énergie pour sa fabrication, etc. La conception respectant un tel cahier des charges suppose donc des compromis rendant la recherche de solutions technologiques particulièrement subtile.

1

La structure pneumatique est ainsi régie par une physique complexe. De par sa structure composite et la nature des matériaux qui la constituent, elle relève d'une mécanique fortement non-linéaire, hétérogène et anisotrope. Ainsi de nombreux ingrédients mécaniques et mathématiques sont envisagés conjointement afin d'assurer une modélisation pertinente, parmi lesquels on peut citer :

- La mécanique du contact entre la structure et le sol.

- Le déplacement du chargement de la structure au cours du temps et donc de la zone de contact au cours de l'avancement.

- La mécanique en grandes déformations qui opère pour développer une aire de contact assurant les différentes fonctions de la structure.

Pour toutes ces contraintes, les outils de simulation peuvent apporter une aide précieuse dans la conception du produit d'abord, mais également dans la compréhension des mécanismes qui sous-entendent ces performances. En particulier, les méthodes d'optimisation permettent de fournir à l'utilisateur (les concepteurs) des outils d'aide à la recherche du compromis.

Le pneumatique sans air

Depuis quelques années, les fabricants de pneumatiques s'intéressent à une innovation qui pourrait révolutionner le marché. Il s'agit des pneumatiques sans air ou roues porteuses, comme présentés en Figure 1.

Figure 1: Pneumatiques "sans air" ou roues porteuses conçus par l'entreprise MFP MICHE-LIN : le TWEEL (2012) à gauche et le prototype UPTIS (2019) à droite.

La structure pneumatique sans air est de plus en plus étudiée (appelée en anglais "airless tyre") et sa mise sur le marché est proche, prévue d'ici la fin de la décennie 2020. Il diffère du pneumatique classique principalement dans le fait qu'il ne permet de porter le véhicule par la pression de l'air. Le pneumatique sans air garantit un risque de crevaison nul et donc potentiellement une durée de vie plus importante et surtout un risque d'accident réduit. Par ailleurs, un rechapage permettra de remplacer la bande de roulement lorsque celle-ci sera

usée. Ceci permettra de réutiliser la structure porteuse et d'économiser de la matière. Bien sûr, les concepteurs souhaitent garantir le même niveau de performances sur ces nouvelles structures induisant un challenge industriel immense. Notre étude se concentrera sur cette structure creuse en particulier que nous appellerons pneumatique sans air ou "airless tyre".

Contexte scientifique

Problème élastique avec contact

On cherche à optimiser une structure élastique roulante $\Omega \subset \mathbb{R}^d, d = 2$ (en deux dimensions) ou 3 (en trois dimensions), un exemple étant décrit en Figure 2. Le bord $\partial \Omega$ du domaine Ω est divisé en trois parties distinctes : Γ_N, Γ_C et Γ_D. Une condition de Neumann est considérée sur Γ_N où une densité de force g_N est imposée. Un contact avec frottement peut avoir lieu entre le bord Γ_C du pneumatique (correspondant à la bande de roulement) et un obstacle rigide et plat. Enfin une condition de déplacement imposé α_D est considérée sur le bord rigide Γ_D et correspond au poids du véhicule sur la jante du pneumatique (α_D est une inconnue supplémentaire qui est déterminée en imposant le poids sur la jante). A noter que seule la frontière Γ_N pourra être optimisée, la jante Γ_D et la bande de roulement Γ_C étant supposées non optimisables dans toute cette étude.
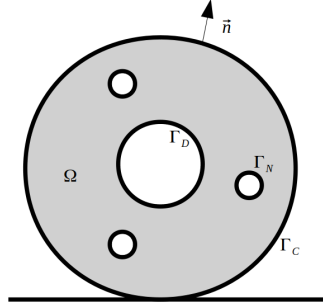
Figure 2: Représentation schématique du pneumatique et de l'obstacle rigide.

On suppose ici que le champ de déplacement $u_\Omega : \Omega \to \mathbb{R}^d$ est solution du problème élastique suivant :

$$\begin{cases} - \operatorname{div} \sigma(u_\Omega) = f & \text{dans } \Omega, \\ \sigma(u_\Omega)\, n = g_N & \text{sur } \Gamma_N, \\ u_\Omega = \alpha_D & \text{sur } \Gamma_D. \end{cases} \tag{1}$$

où, dans le cadre de l'élasticité linéaire,

$$\sigma(u) = A\, \varepsilon(u) = 2\mu\varepsilon(u) + \lambda tr(\varepsilon(u))I_d,$$

avec μ et λ les coefficients de Lamé, $\varepsilon(u) = \frac{1}{2}(\nabla u + \nabla u^T)$ la déformation linéarisée. La condition de contact sera explicitée ultérieurement. Comme le pneumatique est supposé

rouler sur l'ensemble de la bande de roulement en rotation, on considère N_d cas de chargement à différentes rotations régulièrement espacées. On obtient ainsi N_d rotations du pneumatique correspondant aux domaines Ω_i (voir la Figure 3), pour i allant de 1 à N_d. La solution du déplacement associée au domaine Ω_i est de plus notée u_Ω^i.
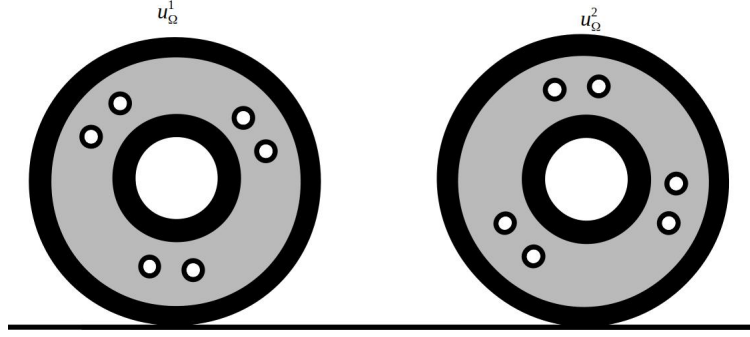
Figure 3: Représentation du pneumatique à différents angles de rotation. Deux configurations de Ω à differentes rotations pour $i = 1, 2$.

Contact unilatéral avec frottement

Le sol (ou obstacle) est supposé rigide et plat. On considère la normale entrante n_y au sol et g le gap initial entre l'obstacle et la bande de roulement (voir Figure 4). Le déplacement $u : \Omega \to \mathbb{R}^d$ est décomposé sur Γ_C par sa composante normale $u_n = u \cdot n_y$ et tangentielle $u_t = (I_d - n_y \otimes n_y)u$ de sorte que

$$u = u_n n_y + u_t.$$
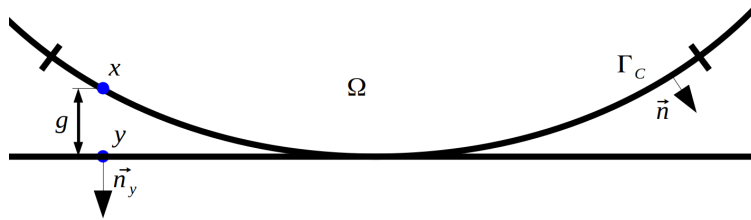
Figure 4: Représentation des surfaces de contact pour une configuration de la rotation du pneumatique.

Le gap initial est défini sur $x \in \Gamma_C$ par

$$g = n_y \cdot (y - x),$$

où y est la projection orthogonale de x sur l'obstacle. On note également la décomposition de la contrainte de contact sur Γ_C en composantes normales et tangentielles :

$$\sigma_n(u) = (\sigma(u)n) \cdot n_y \text{ et } \sigma_t(u) = \sigma(u)n - (\sigma(u)n) \cdot n_y.$$

La condition de contact unilatéral sur Γ_C est décrite par la condition de complémentarité suivante :

$$(u_n - g) \leq 0, \ \sigma_n(u) \leq 0, \ (u_n - g)\,\sigma_n(u) = 0. \tag{2}$$

Nous considérons le frottement de Coulomb statique :

$$\begin{cases} |\sigma_t(u)| \leq -\mathcal{F}\sigma_n(u) & \text{si } u_t = 0, \\ \sigma_t(u) = \mathcal{F}\sigma_n(u)\frac{u_t}{|u_t|} & \text{sinon.} \end{cases} \tag{3}$$

On introduit $a : V \times V \to \mathbb{R}$ et $\ell : V \to \mathbb{R}$, définis pour tout $(u,v) \in V \times V$ par

$$a(u,v) = \int_\Omega A\varepsilon(u) : \varepsilon(v) \,\mathrm{d}x,$$

$$\ell(v) = \int_\Omega f(x) \cdot v \,\mathrm{d}x + \int_{\Gamma_N} g_N \cdot v \,\mathrm{d}s(x),$$

où $V = \{v \in H^1(\Omega;\mathbb{R}^d) : v = \alpha_D \text{ on } \Gamma_D\}$.

La formulation faible du problème d'élasticité en élasticité linéaire avec une condition de contact mène à ce que $u_\Omega \in V$ satisfasse

$$\begin{cases} \text{Find } u \in K \text{ such that} \\ a(u, v - u) + j(v) - j(u) \geq \ell(v - u), \quad \forall v \in K, \end{cases}$$

avec $j(v) = -\displaystyle\int_{\Gamma_C} \mathcal{F}\sigma_n(v)|v_t|\mathrm{d}s(x)$ et

$$K := \{v \in V : v_n - g \in K_0\}, \quad K_0 := \{v \in L^2(\Gamma_C) : v \leq 0\}.$$

Formulation faible avec la méthode de Nitsche

La méthode de Nitsche, présentée initialement par J. Nitsche pour une condition de Dirichlet, a ensuite été introduite pour le contact unilatéral sans puis avec frottement. Elle introduit un terme qui impose faiblement les conditions de contact frottant (2) et (3) d'une manière consistante. La méthode de Nitsche est basée sur une formulation équivalente des conditions (2) - (3) et vient originellement de la formulation d'une approche Lagrangien augmenté, ce qui donne

$$\sigma_n(u) = -[\sigma_n(u) - \gamma(u_n - g)]_-,$$
$$\sigma_t(u) = P_{\mathcal{B}(0,\rho(u))}(\sigma(u)n - \gamma u),$$

où $\rho(u) = \mathcal{F}[\sigma_n(u) - \gamma(u_n - g)]_-$ est le seuil de frottement, $\mathcal{F}$ le coefficient de frottement, la partie négative étant définie par $[x]_- = \frac{1}{2}(|x| - x), \forall x \in \mathbb{R}$ et la projection d'un élément $x \in \mathbb{R}^d$ sur la boule $\mathcal{B}(n_y, \rho(u))$ de rayon $\rho(u)$ sur le plan tangent de normale n_y est définie par

$$P_{\mathcal{B}(N_y, \rho)}(q) = \begin{cases} (I_d - n_y \otimes n_y)q & \text{si } |(I_d - n_y \otimes n_y)q| \leq \rho, \\ \rho \frac{(I_d - n_y \otimes n_y)q}{|(I_d - n_y \otimes n_y)q|} & \text{sinon.} \end{cases}$$

Dans le cas du contact unilatéral, la formulation de Nitsche en élasticité linéaire s'écrit

$$a(u, v) + \mathcal{I}_N(u, v, n) = \ell(v), \; \forall v \in V, \tag{4}$$

avec le terme de contact $\mathcal{I}_N(u, v, n)$ tel que

$$\begin{aligned} \mathcal{I}_N(u, v, n) = &-\int_{\Gamma_C} \frac{\theta}{\gamma} \sigma_n(u)\sigma_n(v)\mathrm{d}s(x) - \int_{\Gamma_C} \frac{\theta}{\gamma} \sigma_t(u) \cdot \sigma_t(v)\mathrm{d}s(x) \\ &-\int_{\Gamma_C} \frac{1}{\gamma} \left[\sigma_n(u) - \gamma(u_n - g)\right]_- (\theta\,\sigma_n(v) - \gamma v_n)\mathrm{d}s(x) \\ &+\int_{\Gamma_C} \frac{1}{\gamma} P_{\mathcal{B}(n_y, \rho(u))}(\sigma(u)n - \gamma u) \cdot (\theta\,\sigma_t(v) - \gamma v_t)\mathrm{d}s(x), \end{aligned}$$

où $\theta \in \mathbb{R}$ est un paramètre et $\gamma > 0$ le paramètre de contact. Nous mettrons en évidence les avantages de la méthode de Nitsche, notamment par rapport à la pénalisation.

Optimisation de forme géométrique

L'objectif de cette thèse est de développer une méthodologie permettant d'optimiser la forme d'une structure et donc d'optimiser différents critères. Les algorithmes d'optimisation utilisés sont généralement des algorithmes itératifs de type gradient où l'idée est d'estimer les dérivées des énergies par rapport à la forme. Dans notre approche, nous n'optimiserons pas les paramètres des modèles de loi d'élasticité et seule la structure de l'ensemble est optimisée. La conception mécanique d'une structure pneumatique "sans air" peut être abordée par de tels outils dont l'objectif est d'obtenir un optimum multi-critère. Le choix des critères peut se faire à partir de la littérature (minimiser la masse, l'énergie de déformation, etc.) ou encore en choisissant directement les critères de performances précédemment exposés ou des critères de substitution pour les performances. On prendra le soin de formules mathématiques rigoureuses pour l'expression des critères afin de mener une optimisation au plus juste. On cherche à minimiser un critère $J(\Omega)$ afin d'obtenir la forme optimale de la structure en forçant l'évolution des frontières de la structure. On introduit la forme générique d'un critère d'optimisation (ou critère objectif) :

$$J(\Omega) = \int_\Omega \mathcal{M}(u_\Omega) \, \mathrm{d}x + \int_{\partial\Omega} \mathcal{N}(u_\Omega) \, \mathrm{d}s(x),$$

où u_Ω est la solution de l'équation (1). Ici, $\mathcal{M}$ et $\mathcal{N}$ sont deux fonctions que l'on suppose suffisamment régulières pour que la dérivée directionnelle de J soit bien définie. Soit $D \subset \mathbb{R}^d$ un domaine régulier aux bornes fixes. Soit Ω_{ad} l'ensemble des solutions admissible Ω. La fonction objective $J(\Omega)$ doit être minimisée

$$\inf_{\Omega \in \Omega_{ad}} J(\Omega). \tag{5}$$

On cherche à minimiser le critère $J(\Omega)$ dans (5) sous la contrainte suivante : la formulation faible avec contact (4) doit être respectée.

Nous nous concentrerons donc sur l'optimisation de forme de la géométrie, cette méthode étant relativement facile à implémenter et proposant un potentiel suffisant pour l'aide à la conception d'une telle structure. Ainsi nous ne nous somme pas intéressés dans cette thèse à des techniques de dérivées topologiques. Une boucle d'optimisation de forme se décompose en trois étapes successives :

- Résolution du problème mécanique par une approximation en éléments finis :

$$\begin{cases} \text{Trouver } u^h \in V^h \text{ tel que} \\ a(u^h, v^h) + \mathcal{I}(u^h, v^h, n) = \ell(v^h), \quad \forall v^h \in V^h, \end{cases}$$

où la discrétisation V^h de V utilise une méthode de Galerkin continue et sera précisée.

- Évaluation d'une direction de descente dans l'espace des paramètres pour permettre la minimisation de la fonctionnelle de travail. On formule donc un gradient de forme :

$$\begin{aligned} \mathcal{D}\, J(\Omega)[\Theta] = & \int_{\Gamma_m} (\Theta \cdot n) \left(\mathcal{M}(u_\Omega, x) + A\varepsilon(u_\Omega) : \varepsilon(p_\Omega) - f(x) \cdot p_\Omega \right) \mathrm{d}s(x) \\ & + \int_{\Gamma_m} (\Theta \cdot n) \left(\kappa_m\, \mathcal{N}(u_\Omega, x) + \nabla\mathcal{N}(u_\Omega, x) \cdot n \right) \mathrm{d}s(x) \\ & - \int_{\Gamma_m \cap \Gamma_N} (\Theta \cdot n) \left(\kappa_m\, p_\Omega \cdot g_N + (\nabla(p_\Omega \cdot g_N)) \cdot n \right) \mathrm{d}s(x), \end{aligned}$$

où $\mathcal{D}\, J(\Omega)[\Theta]$ est la dérivée de forme de $J(\Omega)$ dans la direction Θ, Γ_m est le bord mobile ou optimisable de Ω, κ_m est la courbure moyenne de $\partial\Omega$. Ici, p_Ω est la variable de l'état adjoint que l'on approxime également avec la méthode des éléments finis :

$$\begin{cases} \text{Trouver } p^h \in V^h \text{ tel que} \\ a(q^h, p^h) + \mathcal{D}_u\, \mathcal{I}(u^h_\Omega, p^h, n)[q^h] = \ell_{u^h_\Omega}(q^h), \quad \forall q^h \in V^h, \end{cases} \tag{6}$$

avec

$$\ell_{u_\Omega}(q) = - \int_\Omega \mathcal{D}_u\, \mathcal{M}(u_\Omega)[q]\mathrm{d}x - \int_{\partial\Omega} \mathcal{D}_u\, \mathcal{N}(u_\Omega)[q]\mathrm{d}s(x),$$

$\mathcal{D}_u\, \mathcal{M}(u_\Omega)[q]$ et $\mathcal{D}_u\, \mathcal{N}(u_\Omega)[q]$ étant respectivement les dérivées de forme de $\mathcal{M}(u_\Omega)$ et $\mathcal{N}(u_\Omega)$ par rapport à la variable u dans la direction q.

- Utilisation de cette direction de descente pour formuler une géométrie plus optimale.

Nous utilisons différents outils de modélisation, des méthodes numériques et du calcul scientifique pour rendre cet algorithme d'optimisation le plus précis et le plus rapide possible. Nous cherchons à développer l'optimisation de forme avec prise en compte du contact. Nous investiguons notamment l'apport de la méthode de Nitsche dans les modélisations récentes de la condition de contact afin de fournir plus de robustesse dans le résolution du problème mécanique tout en gardant la simplicité d'une formulation sans ajout de multiplicateur de Lagrange. Un calcul de sensibilité est ensuite proposé à travers une méthode de descente de gradient du critère d'optimisation par rapport à l'espace des paramètres utilisé, la complexité étant le contexte non-linéaire dans lequel le calcul mécanique est réalisé (grandes déformations et contact). Ainsi la sensibilité du gradient de forme sera étudiée au moins dans le cadre linéaire. La méthode de l'état adjoint permet de rendre explicite le calcul de sensibilité dans l'algorithme d'optimisation de forme. Nous cherchons également à exprimer différents critères d'optimisation et à obtenir un compromis. La structure étant roulante, nous réalisons cette étude dans un cadre multi-chargement. La méthode des courbes de niveau (dite "level set" en anglais) est une technique numérique d'analyse de surfaces ou de forme qui permet de représenter une géométrie et de mettre en évidence le lieu de la frontière de l'objet d'étude comme le lieu d'iso-valeur zéro d'une fonction distance ou indicatrice. Cette fonction peut alors être advectée pour modifier l'objet sans manipulation du maillage et à l'aide d'une équation d'Hamilton-Jacobi. Une étape de redistanciation est nécessaire pour régulariser le gradient de la fonction sur le domaine d'étude et limiter les erreurs d'advection.

Contribution de la thèse

Afin de réaliser cette étude d'optimisation de forme de la structure d'un pneumatique sans air, nous proposons différentes étapes.

Optimisation de forme en élasticité linéaire

Le premier chapitre se concentre sur l'optimisation de forme géométrique et la construction de l'algorithme. Nous prenons pour exemple la roue porteuse traitée par l'élasticité linéaire. Ceci permet d'introduire les notions physiques et mécaniques nécessaires à la formulation du contact. On introduit également la formulation d'un gradient de forme et de l'état adjoint par la méthode de Céa dite de dérivation rapide. On présente ensuite la méthode globale de l'optimisation menée sur la structure cylindrique en exposant les ingrédients utilisés dans l'algorithme pour rendre efficient la résolution du problème. L'objectif de ce premier chapitre est d'exposer les propriétés avantageuses de la méthode de Nitsche pour approximer la condition de contact, notamment en comparaison avec la pénalisation. On expose

également deux critères d'optimisation permettant déjà de mener une optimisation multi-critère et multi-chargement sur une géométrie simpliste. On introduit notamment un critère d'uniformité de la contrainte de contact que l'on formule rigoureusement comme suit

$$J_{p,2}(\Omega, u_\Omega, p_{mean}) = \frac{1}{2}\|\sigma(u_\Omega)n - p_{mean}\|^2_{H^{-1/2}(\Gamma_C, \mathbb{R}^d)},$$

que l'on compare avec d'autres formulations. On montre donc l'intérêt de la méthode de Nitsche pour traiter le contact dans le cadre de l'optimisation de forme et l'importance d'écrire des critères cohérents mathématiquement, menant à une optimisation pertinente.
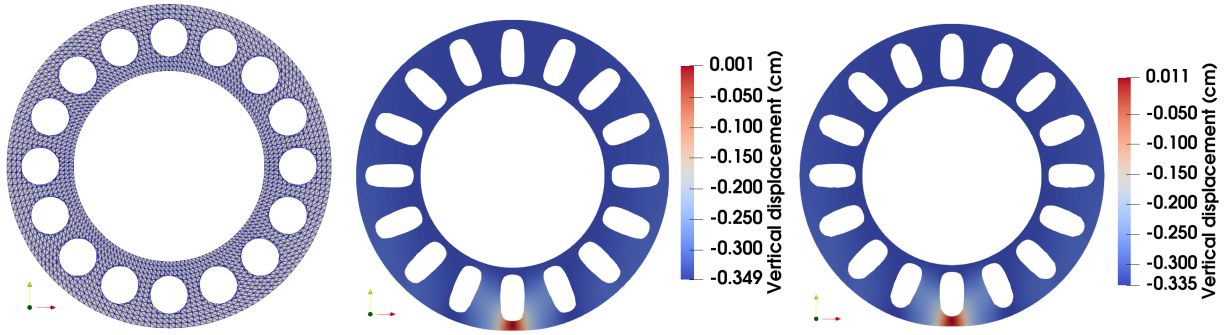
Figure 5: Optimisation d'une structure simple. A gauche : situation initiale, au centre : contact traité par la pénalisation et à droite : contact traité par la méthode de Nitsche.
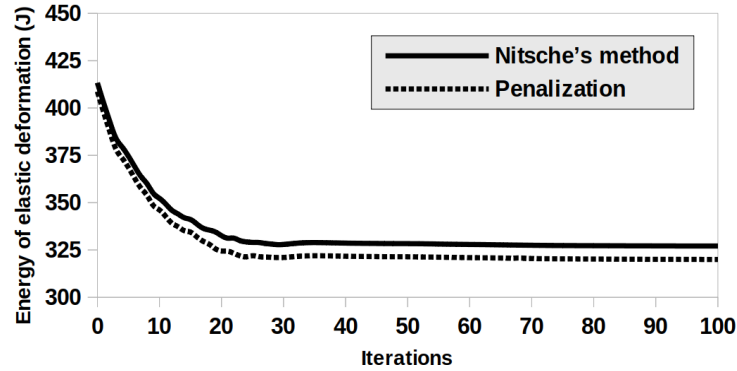
Figure 6: Décroissance du critère d'énergie de déformation élastique en fonction de la méthode d'approximation du contact utilisée.

On expose par exemple en Figures 5 et 6 le fait que la pénalisation n'est pas consistante et qu'elle autorise de l'interpénétration dans le sol, l'énergie de déformation élastique est alors sous-estimée.

Analyse de convergence de l'état adjoint

L'approximation de la condition de contact introduit un opérateur de projection qui n'est pas différentiable au sens classique, notamment en présence de zones de contact affleurantes (qu'on note $\Gamma_{C,b}$). Elle nécessite donc des notions plus faibles de dérivée comme par exemple la dérivée conique. L'objectif de ce nouveau chapitre est donc d'analyser plus précisément la convergence de la méthode précédente. On étudie notamment la convergence de l'état adjoint discret vers une version continue p, qui s'obtient par la résolution d'une équation d'élasticité couplée avec des conditions de Dirichlet sur la zone de contact $\Gamma_{C,a}$ et des conditions de Neumann sur la zone hors contact $\Gamma_{C,i}$ (voir Figure 7) de sorte que

$$
\begin{cases}
-\mathrm{div}\,(\sigma(p)) = -\mathcal{M}'(u_\Omega) & \text{in } \Omega, \\
\sigma(p)n = -\mathcal{N}'(u_\Omega) & \text{on } \Gamma_{C,b} \cup \Gamma_{C,i} \cup \Gamma_N, \\
p = 0 & \text{on } \Gamma_D, \\
(p)_n = 0 & \text{on } \Gamma_{C,a}, \\
\sigma_t(p) = -(\mathcal{N}'(u_\Omega))_t & \text{on } \Gamma_{C,a}.
\end{cases}
$$
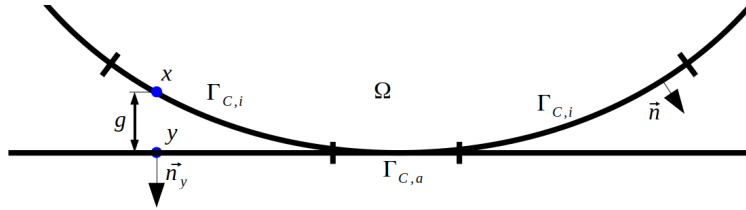
Figure 7: Découpage du bord de contact.

Nous nous sommes alors rendu compte que la méthode précédente où $\tilde{p}^h$ était défini en utilisant la méthode de l'état adjoint sur la formulation discrète du problème de contact (6) n'était pas consistance. En revanche, il est tout à fait possible de définir une nouvelle version discrète p^h, très proche de la précédente, obtenue en appliquant directement la méthode de Nitsche pour traiter les conditions de Dirichlet de p. Cela mène à trouver $p^h \in V_{\Gamma_{C,a}}^h$

$$
a(v^h, p^h) = -\int_\Omega \mathcal{M}'(u_\Omega^h) \cdot v^h \,\mathrm{d}x - \int_{\partial\Omega} \mathcal{N}'(u_\Omega^h) \cdot v^h \,\mathrm{d}s(x), \ \forall v^h \in V_{\Gamma_{C,a}}^h,
$$

avec $V_{\Gamma_{C,a}}^h := \{\phi \in V^h | \phi_n = 0 \text{ presque partout sur } \Gamma_{C,a}\}$.

Ainsi, sous des hypothèses de vitesse de convergence des zones de contact, nous avons réussi à démontrer un résultat de convergence. La difficulté vient essentiellement du contrôle d'erreur dont nous avons besoin sur les zones de contact lorsque le pas de discrétisation h tend vers 0. Nous expliquons aussi comment relâcher les hypothèses de vitesse de convergence en modifiant légèrement cette nouvelle formulation de l'état adjoint. Des expériences numériques illustrent ce résultat et montrent également qu'en pratique, ces deux approches conduisent à

des résultats très similaires, et cela même si la première discrétisation n'est pas consistante (voir Figure 8).
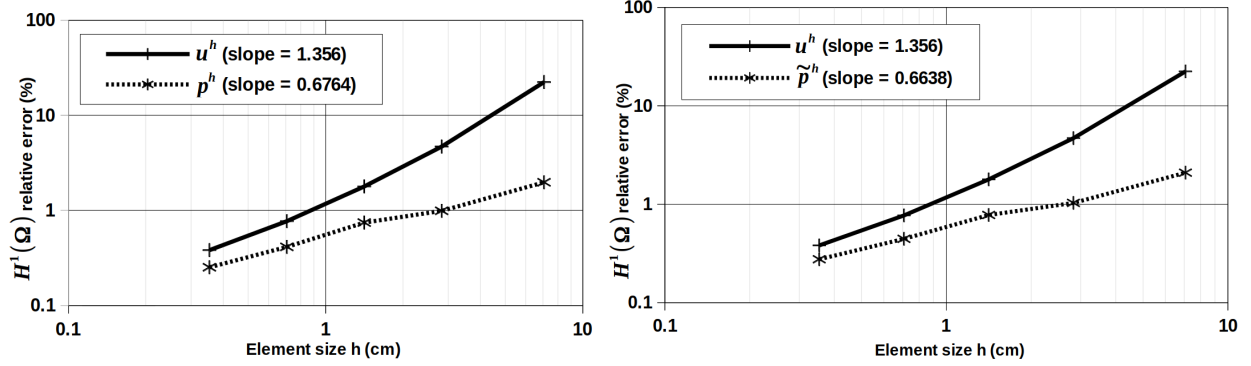
Figure 8: Courbes d'erreur relative avec la norme $H^1(\Omega)$ sur les variables directe et adjointe. A gauche : état adjoint avec la méthode de Nitsche pour traiter la condition de Dirichlet et à droite : état adjoint de la formulation discrète du problème de contact traité par la méthode de Nitsche.

Optimisation en grandes déformations

On souhaite enfin exposer les limites du cadre de l'élasticité linéaire. En effet, l'hypothèse des petites perturbations est embarrassante si on souhaite simuler l'écrasement d'un pneumatique. Les sollicitations du véhicule font intervenir des déformations importantes dans le pneumatique. Le bande de roulement en contact avec le sol développe une aire de contact qui n'a pas de sens physique si on utilise l'élasticité linéaire. Les non-linéarités géométriques doivent donc être prises en compte. Qu'en est-il du comportement matériau ? Les pneumatiques sont en majoritairement composés d'élastomères au comportement non linéaire. Cela a-t-il un effet sur l'optimisation de forme et sur les géométries optimales attendues ? Le troisième chapitre enfin présente l'optimisation de forme d'une structure pneumatique sans air en introduisant la théorie des grandes déformations. On introduit notamment la loi de Saint-Venant Kirchhoff

$$W(E(u)) = \frac{1}{2}\lambda(i_1(E(u)))^2 + \mu\, i_1(E(u)^2),$$

avec W le potentiel énergétique, E le tenseur de Green-Lagrange et i_1 le premier invariant principal. On introduit également la loi de Mooney-Rivlin

$$W(C(u)) = c_1(j_1(C(u)) - 3) + c_2(j_2(C(u)) - 3) + d_1(i_3(C(u))^{1/2} - 1)^2,$$

avec C le tenseur de Cauchy-Green, c_1, c_2 des constantes empiriques et d_1 le paramètre de pénalisation pour l'incompressibilité. $j_1(C)$, $j_2(C)$, i_3 sont des invariants que l'on explicitera. On présente donc les difficultés liées aux non-linéarités introduites par ces lois,

notamment géométriques et matériaux. Un gradient de forme est alors formulé en grandes déformations, un nouveau critère est introduit et on discute de la pertinence de l'optimisation multi-critère sur des géométries à la topologie plus complexe. On montre également la pertinence de différentes lois de comportement matériau. On montre en Figure 9 des exemples d'optimisation de forme où l'on compare l'influence des lois élastiques et hyperélastiques.
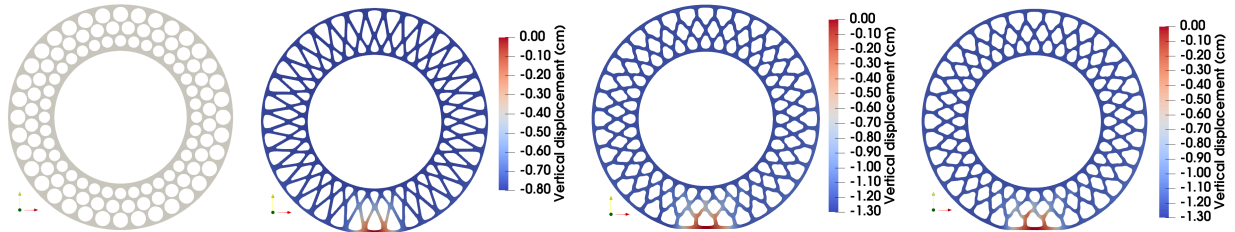
Figure 9: Optimisation d'une structure complexe. De gauche à droite : situation initiale, forme optimale en élasticité linéaire, forme optimale avec le modèle Saint-Venant Kirchhoff, forme optimale avec le modèle Mooney-Rivlin.

Introduction

0.1 Industrial context

Tyres are industrial products designed with complex technologies. Multiple physics must be taken into account in such a structure. Manufacturers must respect performances more and more exacting forcing the designers to intricate challenges. Many application fields must be studied from mathematics and physics to thermo-mechanics and chemistry. The behavior of each part of the tyre depends on many parameters, such as for instance the combination of materials used or the geometry. Many tests and experiments are led in R&T (Research and Technology) teams to understand as best as possible the mechanisms that occur within the tyres.

In the last recent years, manufacturers focus on the design of airless tyres which are not supported by air pressure. They can then reduce the risk of puncture as they can not go flat, resulting in a global much longer life time and the reduction of traffic accident risks.

That product must show the same performances as a "classical" pneumatic tyre. Actually, the airless tyre but more generally a tyre must fulfill several criteria of performances, announced for instance in [53]:

- carry the vehicle load,

- support the longitudinal efforts, in the instantaneous direction of driving - tangentially to the ground, in a dynamic framework in which the vehicle can accelerate or brake,

- guide the vehicle in the ground plan, supporting the transverse efforts through the grip, on a dry or wet ground,

- behave appropriately about rolling resistance with accurate visco-elastic properties,

- absorb the perturbations from the relief and the airborne noise thanks to its damping properties,

- last and prove its durability for a high distance of usage without disturbing the other properties announced above.

Various criteria, called performances, are then required to assure these properties:

- durability and endurance,

- low rolling resistance,

- optimal grip,

- driving comfort,

- low consumption of energy and materials.

These performances can not be all optimally granted in the same product. Among all the tools available, numerical modeling permits to consider different physics and test multiple configurations to understand the airless tyre behavior with less resources than physical experiments, as a first approach. In order to reach the best product, several mathematical tools exist and more especially in the field of structural optimization.

0.2   Structural optimization

The structural optimization is a set of tools used to estimate the best design of a product respecting various criteria of performances. Designers often have intuitive solutions to optimize a structure, yet mathematical tools can have a much higher potential to explore new concepts. Structural optimization is a large field of mathematics, so we focus especially on the optimization of the shape of the structure. The shape optimization aims at finding the best shape of a structure. There are three main ways to lead a shape optimization.

1. The easiest one is the parametric optimization where a narrow set of parameter evolves and modifies the structural geometry (lengths, weights, angles, etc.). It is somehow the most trivial shape optimization to implement but has a very limited potential. The topology of the geometry is fixed which constrains the shape possibilities. We intend to optimize some parameters such as geometric elements: membrane thickness, circle radius, etc. to obtain all the admissible shapes. We refer to [11, 46, 83] for more details about that method.

2. More and more studies have been led on the so called geometric shape optimization. It aims at forcing the frontiers of the structure to evolve in different directions until the best shape is reached. It can lead to complex geometries and is rather easy to be implemented provided that the criteria to be minimized is mathematically easily expressed and differentiable. Yet it is still limited as, despite the topology is optimized, the optimal shape largely depends on the initial situation and the optimization often leads to local minima. We can for instance lead a descent gradient method so that we formulate a shape gradient to reach optimal frontiers. We refer to [41] for the first idea of the frontiers variation method and then [4, 11, 18, 46, 83, 97] for further developments, although many other recent works introduce that method.

3. The third optimization to be implemented is the topological optimization by homogeneous methods. The optimization is not led by the frontiers variation, but by the distribution of matter in a domain containing the geometry. Homogeneous leads to define a density as 1 where there is matter and 0 in the holes. That density is to be optimized during the optimization process and varies between 0 and 1. This leads to optimal structures at macro scales but also at micro scales. Composite materials can appear as an optimal solution which might lead to a complex manufacturing process. It is the most complex method to implement. We refer to [75, 105] for the first works on this method.

The geometric shape optimization is developed in the next sections, since it represents a good compromise between the easy implementation provided by this method and the wide range of possibilities assured for the geometry evolution.

0.3   Geometric shape optimization

Geometric shape optimization is built on successive steps. First, one has to ensure the existence of an optimal shape, which is not easy without constraints or regularity. Second, one has to describe the mathematical overview that leads to the derivative with respect to the studied domain. Then, one has to develop the optimality notion, before using successive numerical schemes to solve an optimization algorithm. The geometric shape optimization aims at minimizing a criterion $J(\Omega)$ in order to find the optimal shape of a structure by forcing the domain frontiers to evolve. The choice of criteria can come from literature (minimization of the mass, the elastic energy of deformation, etc.) or directly from the performances linked to the tyre. It requires the formulation of a shape gradient so that a descent gradient method is performed.

An geometric shape optimization loop can be decomposed into three successive steps.

- We solve the mechanical problem using for instance a finite element approximation (see for instance [39, 42, 65, 108, 107, 37]) with the limit conditions considered.

- We evaluate the cost functional of the structure and its derivative to compute the shape gradient.

- We force the evolution of the geometry in a descent direction to consider a new geometry.

Different tools are exploited to lead an efficient geometric shape optimization through the implementation of an algorithm. We present first two simple applications to expose the potentials of that optimization method. Thereby, for the sake of simplicity, we do not develop the different equations of elasticity or optimization in this part but in the successive following chapters.

0.4 Cantilever optimization

Let the domain presented in Figure 10 be a simple study case to introduce the first results of shape optimization. The example introduced is a cantilever, it must carry a load on one of its sides being clamped on the other side. The aim of the optimization is to decrease the structural deformations.
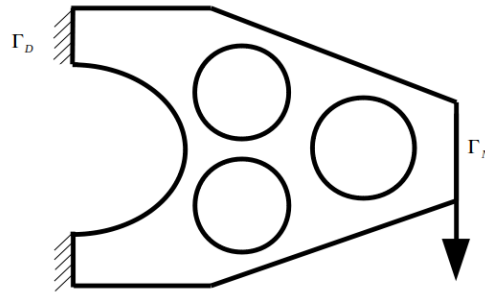
Figure 10: Scheme of the mechanical problem associated to the cantilever.

The domain is clamped on its left boundary called Γ_D and a load is imposed as a Neumann condition on its right boundary called Γ_N. A load of 1 kN is imposed along that same right boundary. Several inner holes are initially set. One considers a material whose Young modulus is 20MPa and Poisson ratio of 0.3. A first computation with a finite element method approximation leads to the mechanical behavior of the structure illustrated in Figure 11.
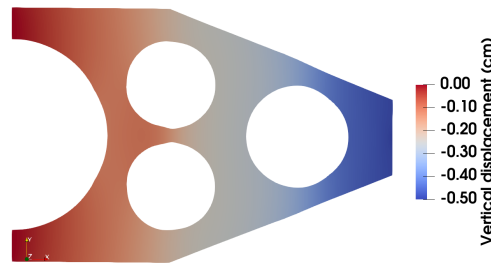
Figure 11: Vertical displacement approximated with a finite element method.

Then we compute the shape gradient associated to the structure as presented in Figure 12 and we force the evolution of the geometry according to that same shape gradient.
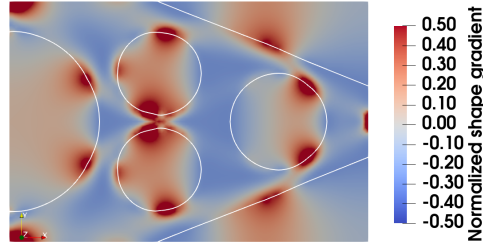
Figure 12: Shape gradient computed on the initial geometry.

The geometry evolves through the optimization process in order to decrease the deformation of the geometry. Figure 13 shows that the load is thereby better and better carried by the geometry.
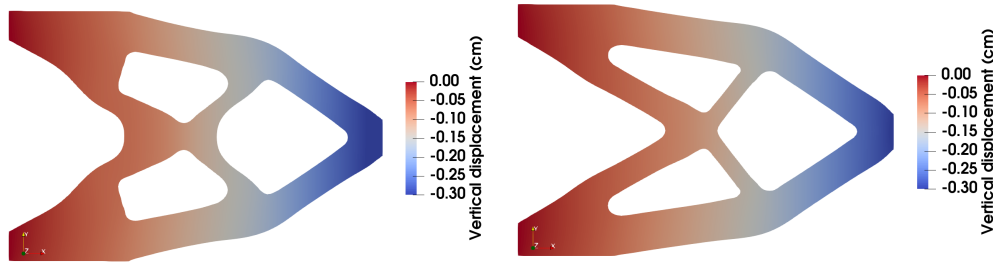
Figure 13: Optimal shape after 20 iterations on the left and after 50 iterations on the right.

The optimization led to a better structure with stronger mechanical properties. We give another example to illustrate the method.

0.5 Bridge optimization

Let the domain presented in Figure 14 be a structure representing a bridge that must carry a load from a side to another. Again, the optimization aims at minimizing the structural deformations. The domain is clamped on its side boundaries called Γ_D and a load is imposed as a Neumann condition on its bottom boundary called Γ_N. A load of 10 MN is imposed along that same bottom boundary. Several inner holes are also initially set. One considers a material whose Young modulus is 20GPa and Poisson ratio of 0.3.
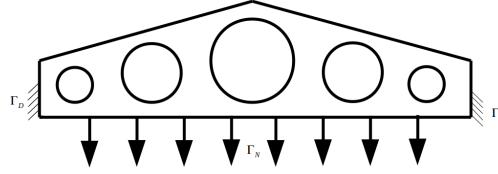
Figure 14: Mechanical scheme of the bridge.

Again, a first computation with a finite element method approximation leads to the computation of the mechanical behavior of the structure in Figure 15.
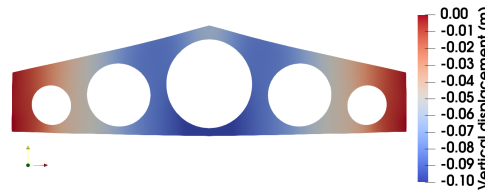
Figure 15: Initial geometry. Vertical displacement after a finite element computation.

Then again we compute the shape gradient associated to the structure and we force the evolution of the geometry according to the shape gradient.
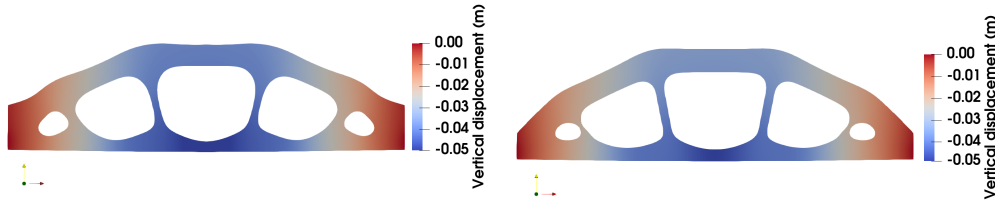
Figure 16: Optimal shape after 20 iterations on the left and after 50 iterations on the right.

The deflection of the bridge is minimized so as the deformation in the whole structure. Once again, the optimization was efficient and led to a stronger geometry.

0.6 Airless tyre optimization

We would like now to optimize the structure of the airless tyre structure presented previously. The optimization process is much more complex than for the tow previous examples. Indeed, the contact between the tyre and the ground introduces a complex condition in the mechanical and optimization problems. Contact conditions (or Signorini conditions) involve non

linearities in the mechanical problem and non differentiabilities which harden the formulation of criterion derivatives to consider the shape gradient. What's more, large deformations occur in the airless tyre which implies the need to use complex elastic laws. Indeed, the simple linearized elasticity model is not sufficient. The consideration of hyperelastic laws to model high deformations involves other non linearities in the mechanical problem. The geometric shape optimization of such a structure is hence much more intricate. We have to develop different models and methods to lead the optimization process as precise as possible.

0.6.1 Numerical modeling and methods

We want to develop the geometric shape optimization taking into account a contact condition. To do so, we follow the Nitsche's method to deal with the contact conditions to bring robustness in the finite element approximation but still with a simple formulation without the use of Lagrange multipliers. A sensitivity calculus is then proposed through the descent gradient method of the optimization criterion. The adjoint state method will lead to the formulation of an explicit shape gradient. The complexity relies in the differentiability of such formulations that must be studied. The other complexity is due to the non linearity while hyperelastic laws are considered for large deformations. Different criteria will be expressed and numerical experiments will be performed to reach the best compromise. The airless tyre being a rolling structure, multiple loads will be performed and so multiple finite element computations.

In order to describe the geometry, we use the level set method. The latter aims at describing curves, surfaces and volumes since it highlights the frontier of the structure as the iso-value zero of, for instance, a distance function. That function has the advantages to be easily manipulated so that, during the optimization process, the geometry can easily be transported thanks to a Hamilton-Jacobi equation. By this way, no manipulation of the mesh is required.

The finite element method permits a good approximation of the structure mechanical behavior. We especially exploit the fictitious domains method - based on the XFEM - manipulating cut finite elements that especially adapt to the geometry at each optimization iteration. While the fictitious domains method and the level set function are performed in the same algorithm, only one structured and regular mesh can be used without modification steps. The mesh is then fixed during all the optimization process which largely accelerate the algorithm execution.

0.7 Outline

This thesis manuscript is organized in three chapters as follows.

1. The first chapter provides the geometric shape optimization description of a rolling structure considering the linear elasticity as a first approximation. We present the

mechanical framework with Nitsche's method to treat the unilateral contact condition and the optimization process without any considerations of differentiability of the different formulations and especially of the shape gradient. We expose the relevance of Nitsche's method to treat the contact condition. Two criteria are introduced: the classical elastic energy of deformation and the uniformity of the contact stress, for which a particular mathematical attention is performed. A very simple geometry of a rolling structure is proposed and numerical tests are proposed.

2. The second chapter is focused on the sensitivity of the shape gradient in a Nitsche-based formulation of the optimization problem. Actually, the contact condition involves non differentiabilities owing to the introduction of projection operators. The criterion is not differentiable in the classical sense. Yet we introduce a weaker notion of differentiability so that the shape gradient makes sense. More particularly, we introduce Nitsche's method in the adjoint state and we analyze its formulation. An a priori error estimate is calculated to prove the convergence of discrete variables towards continuous ones.

3. The third chapter introduces the geometric shape optimization with contact through the finite strain theory. The consideration of large deformations permits to correctly model the physical behavior of the airless tyre. We expose the mechanical formulation based on Nitsche's method again to deal with the unilateral contact condition in the large strain configuration. More complex geometries are initialized to progressively reach the airless tyre structure. Hyperelastic laws are proposed to model large deformations and a comparison is done between elastic laws to show in particular the limits of the linear elasticity. A third criterion is introduced to force the uniformity of the tyre deflection along its rotation.

This thesis manuscript is then closed by a chapter of conclusions on the achieved work and the outlook for further potential studies.
In appendix A, we introduce the different mechanisms to force the evolution of the level set function. The schemes used to transport the level set function are exposed. Along the optimization process, that same function progressively looses regularity so we propose two treatments to gain back that regularity: redistancing and smoothing steps. The schemes associated to these treatments are exposed so as the choice of parameters used in the optimization algorithm.

Chapter 1

Shape optimization in linearized elasticity

Contents

1.1   Introduction

The motivation of this first chapter is the optimization of an elastic load-bearing rolling structure under criteria of compliance and uniformity of the contact stress in a multi-loading context. This first part follows the same effort as in [14].

In this work, the elastic rolling structure is in contact with a flat ground. This generates some non-linearity and non-differentiability issues according to the contact approximation. The latter can be consistent or not, and lead to numerical imprecisions. The elastic rolling structure is optimized under mechanical criteria such as deformation and stability criteria while the structure rolls. Thereby, a multi-loading strategy simulates the rotation of the structure and leads to uniformity criteria on all the loading computations. We derive the corresponding shape gradient and a descent method classically based on the early ideas of J. Hadamard [41] and on later developments, such as the formulation in terms of a Lagrangian due to J. Céa [18] and the adjoint method [66] introduced by J.-L. Lions.

Our purpose is to compare two methods for the approximation of the contact condition in the shape optimization framework: the penalty approach and Nitsche's method. We also introduce two strategies to deal with the uniformity criteria while the structure is rolling. We propose numerical experiments, representing the geometry thanks to the level set method to ease its evolution as exposed by G. Allaire, F. Jouve and A.-M. Toader in [9]. We also use the finite element method to compute the mechanical problem and especially we develop the fictitious domains method [52, 17] based on cut finite elements to deal with complex geometries.

We consider a rolling linearly elastic structure occupying in its reference configuration a domain $\Omega \subset \mathbb{R}^d, d = 2$ or 3 whose shape is to be optimized, an example being depicted in Figure 1.1. The boundary $\partial\Omega$ of the domain is split into three non-overlapping parts, Γ_N, Γ_C and Γ_D. A Neumann condition is considered on Γ_N where a force density g_N is prescribed. A contact with friction might occur with a flat and horizontal rigid obstacle on Γ_C and a homogeneous Dirichlet condition is prescribed on Γ_D.
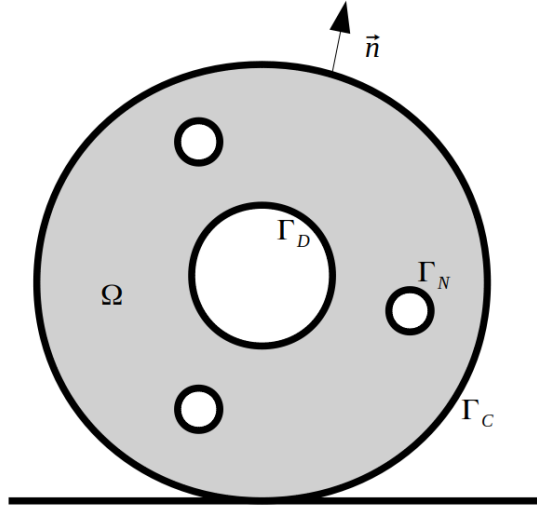
Figure 1.1: Schematic representation of Ω and the rigid obstacle.

The displacement $u_\Omega : \Omega \to \mathbb{R}^d$ of the body according to its reference configuration is solution to the following linearized elasticity problem:

$$\begin{cases} -\operatorname{div}\sigma(u_\Omega) = f & \text{in } \Omega \text{ where } \sigma(u_\Omega) = A\,\varepsilon(u_\Omega), \\ \sigma(u_\Omega)\,n = g_N & \text{on } \Gamma_N, \\ u_\Omega = 0 & \text{on } \Gamma_D, \end{cases} \tag{1.1}$$

where A is the fourth order symmetric tensor of elasticity, $\varepsilon(u)$ is the small deformations tensor, and n is the outward unit vector to Ω. The contact condition on Γ_C will be developed in the next section. Assuming the isotropy of the material, the tensor A finally reads

$$\sigma(u) = A\,\varepsilon(u) = 2\mu\varepsilon(u) + \lambda tr(\varepsilon(u))I_d, \tag{1.2}$$

where μ and λ are the Lamé material parameters.

For the purpose of our study, we consider that the contact and Dirichlet boundaries Γ_C and Γ_D are not some optimizable parts. However, the generalization to optimizable contact and Dirichlet boundaries is rather straightforward. Indeed, in case of optimizable contact boundaries, the work proposed in [69] should be adapted to Nitsche's method.

The structure is supposed to roll upon a ground (the obstacle) along its outer radius. We take this into account by considering N_l load positions, obtained as N_l rotations Ω_i of the domain Ω (see Figure 1.2), for i from 1 to N_l, with regularly spaced rotations of angles $i2\pi/N_l$. The displacement for the rotated domain Ω_i will be denoted u_Ω^i.

Ω_1 Ω_2
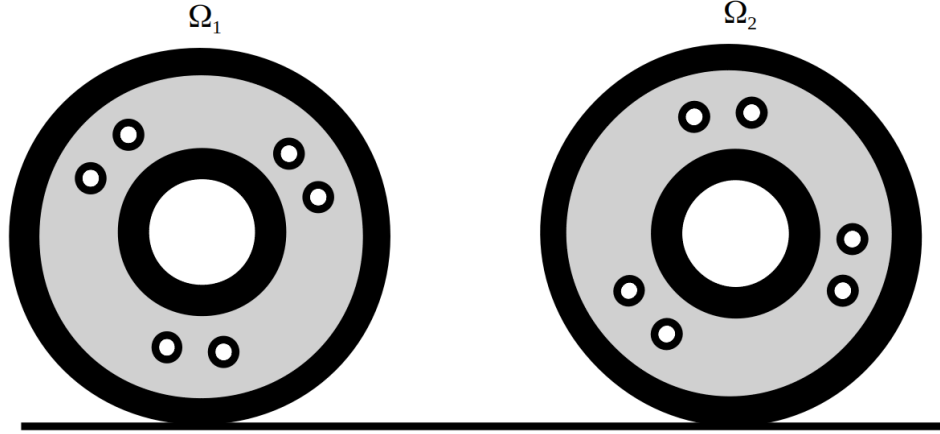
Figure 1.2: Rolling structure representation. Two configurations of Ω at different rotations for $i = 1, 2$.

Classically, the basic optimization criterion we consider corresponds to the strain energy, which we sum here on each load position:

$$\sum_{i=1}^{N_l} J_e(\Omega_i, u_\Omega^i) \quad \text{where} \quad J_e(\Omega_i, u_\Omega^i) = \int_{\Omega_i} \frac{1}{2} A\varepsilon(u_\Omega^i) : \varepsilon(u_\Omega^i) \, dx. \tag{1.3}$$

It aims at minimizing the energy associated to the elastic deformation corresponding to each domain Ω_i.

In order to obtain a structure that rolls as uniformly as possible, we introduce a second criterion. To this purpose, we introduce the mean contact stress on the contact boundary Γ_C, where the average is obtained over the different load positions:

$$p_{mean} = \frac{1}{N_l} \sum_{i=1}^{N_l} \sigma(u_\Omega^i) n.$$

A first idea leads to minimize on each load position

$$J_p(\Omega, u_\Omega, p_{mean}) = \int_{\Gamma_C} \frac{L}{2E} (\sigma(u_\Omega)n - p_{mean})^2 ds(x), \tag{1.4}$$

where L is a characteristic length and E is Young's modulus.

However, expression (1.4) is not completely satisfactory since the contact stress $\sigma(u)n$ may not be square integrable in some context and even if it is, continuity of (1.4) with respect to the problem data cannot be ensured. We develop in section 1.3.3 two more consistent variants of this criterion.

Finally, we consider the following global objective function

$$J(\Omega) = \sum_{i=1}^{N_l} J_g(\Omega_i, u_\Omega^i, p_{\text{mean}}), \tag{1.5}$$

where

$$J_g(\Omega_i, u_\Omega^i, p_{\text{mean}}) = J_e(\Omega_i, u_\Omega^i) + \alpha J_p(\Omega_i, u_\Omega^i, p_{mean}), \tag{1.6}$$

and we study the influence of the parameter α on the optimal shape Ω.

The main contribution of this work is twofold: first of all, we propose a comparison of the penalty and Nitsche's method in the framework of shape optimization. The second contribution of this work is to propose and test an efficient criterion for the uniformization of the contact stress according to the different load positions.

In section 1.2, we introduce the problem with a frictional contact condition, its approximation with a penalty approach and a consistent formulation based on Nitsche's method. In section 1.3, the geometric shape optimization framework is presented. In section 1.4, we introduce the discretization used and the optimization method. Finally, in section 1.5, we present some numerical results which highlight the interest of Nitsche's method and the efficiency of the geometric shape optimization to obtain optimal domains Ω that minimize the criteria previously introduced.

1.2 Weak formulation of the contact problem

In this section, we describe the unilateral contact condition with friction on the boundary Γ_C and provide the weak formulation of the elastic problem for both a penalized contact condition and Nitsche's method.

1.2.1 Classical weak inequality formulations

The displacement $u_\Omega : \Omega \to \mathbb{R}^d$ of the body according to its reference configuration satisfies the equations of system (1.1). To derive a weak formulation, let us also introduce the Hilbert space $V = \{v \in H^1(\Omega; \mathbb{R}^d) : v = 0 \text{ on } \Gamma_D\}$ and the two applications $a : V \times V \to \mathbb{R}$ and $\ell : V \to \mathbb{R}$, defined for all $(u, v) \in V \times V$ by

$$a(u, v) = \int_\Omega A\varepsilon(u) : \varepsilon(v) \, \mathrm{d}x,$$

$$\ell(v) = \int_\Omega f(x) \cdot v \, \mathrm{d}x + \int_{\Gamma_N} g_N \cdot v \, \mathrm{d}s(x).$$

Then, using Green's formula and under regularity assumptions, one shows that the displacement field $u_\Omega \in V$ satisfies

$$a(u, v) - \int_{\Gamma_C} \sigma(u)n \cdot v \, \mathrm{d}s(x) = \ell(v), \quad \forall v \in V. \tag{1.7}$$

The obstacle is supposed to be rigid and flat. We consider n_y, the inward unit vector to the rigid obstacle and g the initial gap between the elastic body and the obstacle (see Figure 1.3). On the contact boundary Γ_C, the displacement $u : \Omega \to \mathbb{R}^d$, is decomposed into its normal component $u_n = u \cdot n_y$ and its tangent one $u_t = (I - n_y \otimes n_y)u$ such that

$$u = u_n n_y + u_t.$$
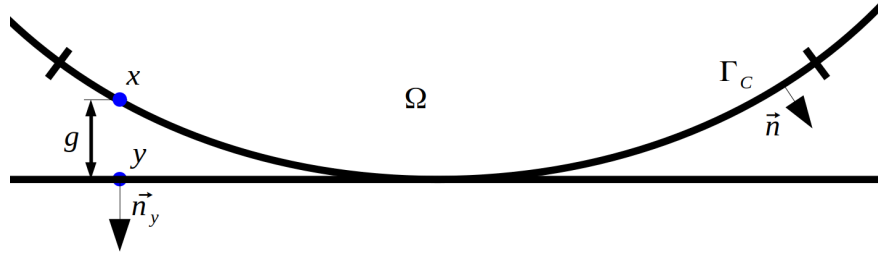
Figure 1.3: Contact surface representation for the vertical load configuration.

The initial gap between the body and the obstacle is defined on $x \in \Gamma_C$ by

$$g = n_y \cdot (y - x),$$

where y is the orthogonal projection of x upon the rigid obstacle. We note also the decomposition of the contact stress on Γ_C into normal and tangent parts:

$$\sigma_n(u) = (\sigma(u)\, n) \cdot n_y, \quad \sigma_t(u) = (I_d - n_y \otimes n_y)(\sigma(u)\, n).$$

The unilateral contact condition on Γ_C can be expressed by the following complementary condition:

$$(u_n - g) \leq 0,$$
$$\sigma_n(u) \leq 0,$$
$$(u_n - g)\, \sigma_n(u) = 0.$$

In case of frictionless contact, the displacement u_Ω is the minimizer of the energy $\frac{1}{2}a(u, u) - \ell(u)$ on the convex K of admissible displacements satisfying the non-interpenetration condition on the boundary Γ_C defined as

$$K := \{v \in V : v_n - g \in K_0\}, \quad K_0 := \{v \in L^2(\Gamma_C) : v \leq 0\}.$$

The corresponding optimality system reads (see [32])

$$\begin{cases} \text{Find } u \in K \text{ such that} \\ a(u, v - u) \geq \ell(v - u), \quad \forall v \in K. \end{cases} \tag{1.9}$$

Under standard assumptions, the existence and uniqueness of the solution to problem (1.9) is a direct consequence of Stampacchia's theorem (see [34]).

The classical Coulomb law of friction can be written on Γ_C as

$$
\begin{cases}
|\sigma_t(u)| \leq -\mathcal{F}\sigma_n(u) & \text{if } \dot{u}_t = 0, \\
\sigma_t(u) = \mathcal{F}\sigma_n(u)\frac{\dot{u}_t}{|\dot{u}_t|} & \text{otherwise,}
\end{cases}
$$

where $\mathcal{F} \geq 0$ is the friction coefficient, depending on the couple of materials in contact and $\dot{u}_t$ is the sliding velocity. The Coulomb law of friction is usually approximated by replacing the sliding velocity by the finite difference

$$
\frac{u_t - u_t^0}{\Delta t},
$$

where u_t^0 stands for the tangent displacement at an initial time step and Δt the time step. For the sake of simplicity, taking $u_t^0 = 0$ leads to the so called static Coulomb's law of friction:

$$
\begin{cases}
|\sigma_t(u)| \leq -\mathcal{F}\sigma_n(u) & \text{if } u_t = 0, \\
\sigma_t(u) = \mathcal{F}\sigma_n(u)\frac{u_t}{|u_t|} & \text{otherwise.}
\end{cases}
\tag{1.10}
$$

In case of contact with friction, the displacement u_Ω is solution to the following weak inequality formulation (see [32]):

$$
\begin{cases}
\text{Find } u \in K \text{ such that} \\
a(u, v - u) + j(v) - j(u) \geq \ell(v - u), \quad \forall v \in K,
\end{cases}
\tag{1.11}
$$

where $j(v) = -\displaystyle\int_{\Gamma_C} \mathcal{F}\sigma_n(v)|v_t|\mathrm{d}s(x)$. The existence of solutions to Problem (1.11) is addressed for instance in [60, 33] and is not generally ensured for arbitrary large friction coefficients. Condition of uniqueness of the solution to this problem still remains an open question, partially addressed in [85, 56, 57].

1.2.2 Weak formulation with a penalty method

The penalty method (see [61] for instance) is a simple way to treat contact problems. It involves an additional weak term in the weak formulation standing for a stiffness at the boundaries limiting inter-penetration between the body and the obstacle. It is non-consistent in the sense that it represents a supplementary approximation of the contact condition. For $\gamma > 0$ the penalty parameter, the frictional contact conditions (1.8) - (1.10) are approximated by

$$
\begin{aligned}
\sigma_n(u) &= -\gamma[g - u_n]_-, \\
\sigma_t(u) &= P_{\mathcal{B}(n_y, \rho(u))}(\gamma u),
\end{aligned}
\tag{1.12}
$$

where $\rho(u) = \mathcal{F}\gamma[g - u_n]_-$ is the friction threshold, the negative part being defined by $[x]_- = \frac{1}{2}(|x| - x), \forall x \in \mathbb{R}$ and the projection of an element $x \in \mathbb{R}^d$ on the ball $\mathcal{B}(n_y, \rho(u))$ of radius $\rho(u)$ on the tangent plane with respect to n_y (see also [84]) is defined by

$$P_{\mathcal{B}(n_y,\rho)}(q) = \begin{cases} (I_d - n_y \otimes n_y)q & \text{if } |(I_d - n_y \otimes n_y)q| \leq \rho, \\ \rho\frac{(I_d - n_y \otimes n_y)q}{|(I_d - n_y \otimes n_y)q|} & \text{otherwise.} \end{cases}$$

Recall that using (1.7) the displacement field $u_\Omega \in V$ satisfies

$$a(u, v) - \int_{\Gamma_C} (\sigma_n(u)v_n + \sigma_t(u) \cdot v_t)\mathrm{d}s(x) = \ell(v), \quad \forall v \in V. \tag{1.13}$$

Finally, a weak formation for the penalty method can be easily deduced by incorporating equalities (1.12) in (1.13) which conduces to introduce the solution $u_\Omega^P \in V$ of

$$a(u, v) + \mathcal{I}_P(u, v, n_y) = \ell(v), \ \forall v \in V, \tag{1.14}$$

where the penalty contact term $\mathcal{I}_P(u, v, n_y)$ is

$$\mathcal{I}_P(u, v, n_y) = \int_{\Gamma_C} (\gamma[g - u_n]_- \ v_n \ - P_{\mathcal{B}(n_y,\rho(u))}(\gamma u) \ \cdot \ v_t)\mathrm{d}s(x). \tag{1.15}$$

We refer to [32, 28] for the existence of a solution to problem (1.14).

1.2.3   Weak formulation using Nitsche's method

Nitsche's method, presented by J. Nitsche in [77], aimed first at treating Dirichlet conditions. The Nitsche method we used to account for the contact condition with friction was originally introduced in [23, 25] for frictionless contact, then generalized to Tresca's friction in [21] and Coulomb's friction in [24] (see also the overview [22]). The Nitsche method introduces a contact term which weakly prescribed the frictional contact conditions (1.8)-(1.10) in a consistent manner (see for instance [86] for the numerical efficiency of Nitsche's method compared to other classical methods). It is based on the equivalent reformulation of the contact conditions which has been originally derived from the augmented Lagrangian approach [3] and reads as

$$\begin{aligned} \sigma_n(u) &= -[\sigma_n(u) - \gamma(u_n - g)]_-, \\ \sigma_t(u) &= P_{\mathcal{B}(n_y,\rho(u))}(\sigma(u)n - \gamma u), \end{aligned} \tag{1.16}$$

where ρ is now defined by $\rho(u) = \mathcal{F}[\sigma_n(u) - \gamma(u_n - g)]_-$. More precisely, incorporating

$$v_n = -\frac{1}{\gamma}(\theta\sigma_n(v) - \gamma v_n) + \frac{\theta}{\gamma}\sigma_n(v), \quad v_t = -\frac{1}{\gamma}(\theta\sigma_t(v) - \gamma v_t) + \frac{\theta}{\gamma}\sigma_t(v),$$

for a fixed $\theta \in \mathbb{R}$ in the weak formulation (1.7), we see that $\forall v \in V$,

$$a(u,v) - \int_{\Gamma_C} \frac{\theta}{\gamma} \sigma_n(u)\sigma_n(v) \, \mathrm{d}s(x) + \int_{\Gamma_C} \frac{1}{\gamma} \sigma_n(u)(\theta\sigma_n(v) - \gamma v_n)\mathrm{d}s(x)$$
$$- \int_{\Gamma_C} \frac{\theta}{\gamma}\sigma_t(u) \cdot \sigma_t(v)\mathrm{d}s(x) + \int_{\Gamma_C} \frac{1}{\gamma} \; \sigma_t(u) \cdot (\theta\sigma_t(v) - \gamma v_t)\mathrm{d}s(x) = \ell(v), \tag{1.17}$$

which becomes

$$a(u,v) - \int_{\Gamma_C} \frac{\theta}{\gamma}\sigma_n(u)\sigma_n(v)\mathrm{d}s(x) - \int_{\Gamma_C} \frac{\theta}{\gamma}\sigma_t(u) \cdot \sigma_t(v)\mathrm{d}s(x)$$
$$- \int_{\Gamma_C} \frac{1}{\gamma} \; [\sigma_n(u) - \gamma(u_n - g)]_- \; (\theta \, \sigma_n(v) - \gamma v_n)\mathrm{d}s(x)$$
$$+ \int_{\Gamma_C} \frac{1}{\gamma} P_{\mathcal{B}(n_y,\rho(u))}(\sigma(u)n - \gamma u) \cdot (\theta \, \sigma_t(v) - \gamma v_t)\mathrm{d}s(x) = \ell(v), \; \forall \, v \in V,$$

by using additionally (1.16). Finally, the Nitsche approach conduces to define the solution u_Ω^N to

$$a(u,v) + \mathcal{I}_N(u,v,n) = \ell(v), \; \forall v \in V, \tag{1.18}$$

where the contact term $\mathcal{I}_N(u,v,n)$ reads

$$\mathcal{I}_N(u,v,n) = - \int_{\Gamma_C} \frac{\theta}{\gamma}\sigma_n(u)\sigma_n(v)\mathrm{d}s(x) - \int_{\Gamma_C} \frac{\theta}{\gamma}\sigma_t(u) \cdot \sigma_t(v)\mathrm{d}s(x)$$
$$- \int_{\Gamma_C} \frac{1}{\gamma} \; [\sigma_n(u) - \gamma(u_n - g)]_- \; (\theta \, \sigma_n(v) - \gamma v_n)\mathrm{d}s(x)$$
$$+ \int_{\Gamma_C} \frac{1}{\gamma} P_{\mathcal{B}(n_y,\rho(u))}(\sigma(u)n - \gamma u) \cdot (\theta \, \sigma_t(v) - \gamma v_t)\mathrm{d}s(x). \tag{1.19}$$

Remark 1. *The introduction of the parameter θ leads to different variants acting on the symmetry, skew-symmetry or non-symmetry of the contact term (see [25]). In particular, in the frictionless case, when $\theta = 1$, the formulation is symmetric and admits a potential energy. When $\theta = 0$, a non-symmetric method is set whose formulation is closer to the penalty approach described in 1.2.2. Finally, when $\theta = -1$, the contact term is skew-symmetric and leads to interesting properties independent of the Nitsche parameter γ.*

1.2.4 Analysis of a Nitsche-based finite element method

Let $V^h \subset V$ be a family of finite dimensional vector spaces indexed by h coming from a family $\mathcal{T}^h$ of triangulations of the domain Ω supposed to be polygonal for the sake of simplicity

($h = \max_{T \in \mathcal{T}^h} h_T$ where h_T is the diameter of T). The family of triangulations is supposed regular (i.e., there exists $\sigma > 0$ such that $\forall T \in \mathcal{T}^h, h_T/\rho_T \leq \sigma$ where ρ_T denotes the radius of the inscribed ball in T) and conformal to the subdivision of the boundary into Γ_D, Γ_N and Γ_C (i.e. a face of an element $T \in \mathcal{T}^h$ is not allowed to have simultaneous non-empty intersection with more than one part of the subdivision). For instance, a standard Lagrange finite element method of degree k reads

$$V^h := \{v^h \in \mathscr{C}^0(\bar{\Omega})^d : v^h|_T \in (P_k(T))^d, \forall T \in \mathcal{T}^h, v^h = 0 \text{ on } \Gamma_D\}. \tag{1.20}$$

Let γ be a piecewise constant function on the contact interface Γ_C defined for any $x \in \Gamma_C$ lying on the relative interior of $\Gamma_C \cap T$ for a (closed) element T having a non-empty intersection of dimension $d - 1$ with Γ_C by

$$\gamma(x) = \frac{\gamma_0}{h_T},$$

where γ_0 is a positive given constant. The generalized Nitsche-based approximation then reads:

$$\begin{cases} \text{Find } u^h \in V^h \text{ such that} \\ a(u^h, v^h) + \mathcal{I}_N(u^h, v^h, n) = \ell(v^h), \quad \forall v^h \in V^h. \end{cases}$$

The advantage of Nitsche's method over the penalty approach is its consistency which can be established in the following sense.

Lemma 2. *Suppose that the solution u of (1.1), (1.8) and (1.10) is in $(H^{\frac{3}{2}+\nu}(\Omega))^d$ where $d = 2, 3$ and $\nu > 0$. Then u is also solution, $\forall v^h \in V^h$, of*

$$a(u, v^h) + \mathcal{I}_N(u, v^h, n) = \ell(v^h).$$

Proof. Let u be the solution to (1.1), (1.8) and (1.10). Let v^h be in V^h. Since $u \in (H^{\frac{3}{2}+\nu}(\Omega))^d$ and $\nu > 0$, $\sigma_n(u)$ and $\sigma_t(u) \in H^\nu(\Gamma_C) \subset L^2(\Gamma_C)$. As a result,

$$a(u, v^h) - \int_{\Gamma_C} \frac{\theta}{\gamma} \sigma_n(u) \, \sigma_n(v^h) \, \mathrm{d}s(x) - \int_{\Gamma_C} \frac{\theta}{\gamma} \sigma_t(u) \cdot \sigma_t(v^h) \, \mathrm{d}s(x),$$

makes sense, and $\sigma_n(u) - \gamma(u_n - g)$ and $\sigma_t(u) - \gamma u_t \in L^2(\Gamma_C)$. Using the reformulation of $\sigma_n(u)$ and $\sigma_t(u)$ in (1.16) and formulation (1.17), it holds:

$$a(u, v^h) - \int_{\Gamma_C} \frac{\theta}{\gamma} \sigma_n(u) \sigma_n(v^h) \, \mathrm{d}s(x) - \int_{\Gamma_C} \frac{\theta}{\gamma} \sigma_t(u) \cdot \sigma_t(v^h) \, \mathrm{d}s(x)$$

$$- \int_{\Gamma_C} \frac{1}{\gamma} [\sigma_n(u) - \gamma(u_n - g)]_- \ (\theta \sigma_n(v^h) - \gamma v_n^h) \, \mathrm{d}s(x)$$

$$+ \int_{\Gamma_C} \frac{1}{\gamma} P_{\mathcal{B}(n_y, \rho(u))}(\sigma(u)n - \gamma u) \ \cdot \ (\theta \sigma_t(v^h) - \gamma v_t^h) \, \mathrm{d}s(x)$$

$$= a(u, v^h) - \int_{\Gamma_C} \frac{\theta}{\gamma} \sigma_n(u) \sigma_n(v^h) \, \mathrm{d}s(x) - \int_{\Gamma_C} \frac{\theta}{\gamma} \sigma_t(u) \cdot \sigma_t(v^h) \, \mathrm{d}s(x)$$

$$- \int_{\Gamma_C} \frac{1}{\gamma} \sigma_n(u) \ (\theta \sigma_n(v^h) - \gamma v_n^h) \, \mathrm{d}s(x)$$

$$+ \int_{\Gamma_C} \frac{1}{\gamma} \sigma_t(u) \ \cdot \ (\theta \sigma_t(v^h) - \gamma v_t^h) \, \mathrm{d}s(x)$$

$$= a(u, v^h) - \int_{\Gamma_C} \sigma_n(u) v_n^h \, \mathrm{d}s(x) - \int_{\Gamma_C} \sigma_t(u) \cdot v_t^h \, \mathrm{d}s(x).$$

In the same time, using an integration by parts, it holds:

$$a(u, v^h) - \int_{\Gamma_C} \sigma_n(u) v_n^h \, \mathrm{d}s(x) - \int_{\Gamma_C} \sigma_t(u) \cdot v_t^h \, \mathrm{d}s(x) = \ell(v^h),$$

which ends the proof, as the equality is strictly respected, whatever θ is.   □

The well-posedness and the consistency are analyzed in [23] and [25] for the frictionless formulation. When $\theta = -1$, the well-posedness does not depend on γ_0 anymore, which implies that the value of $\theta = -1$ is a convenient choice for the rest of the computation if robustness is required. Concerning the Nitsche-based formulation with the Coulomb law of friction, the existence of solution is studied in [24].

1.3   Geometric shape optimization

The geometric shape optimization aims at minimizing a criterion $J(\Omega)$ to find the optimal shape of a structure by forcing the domain frontiers to evolve. The energy of the structure can be expressed as a target criterion. If several criteria must be minimized, that energy can be a combination of these criteria and lead to a multi-criterion optimization. The generic formulation for the energy or the target criterion might be expressed as

$$J(\Omega) = \int_\Omega \mathcal{M}(u_\Omega, x) \, \mathrm{d}x + \int_{\partial\Omega} \mathcal{N}(u_\Omega, x) \, \mathrm{d}s(x), \tag{1.21}$$

where u_Ω is defined as the solution of

$$a(u_\Omega, v) + \mathcal{I}(u_\Omega, v, n) = \ell(v), \ \forall v \in V.$$

Here the contact term $\mathcal{I}$ is written as $\mathcal{I}(u, v, n) = \mathcal{I}_P(u, v, n)$ or $\mathcal{I}(u, v, n) = \mathcal{I}_N(u, v, n)$ according to the contact approximation used. Here again, $\mathcal{M}$ and $\mathcal{N}$ are two functions assumed to be sufficiently smooth so that the shape derivative of J is well defined.

Remark 3. *As specified for instance in [69], it is often assumed, in order to ensure that the criteria and the adjoint state are well defined, that*

$$\begin{aligned}
|\mathcal{M}(u, x)| &\leq C(1 + |u|^2), & |\mathcal{N}(u, x)| &\leq C(1 + |u|^2), \\
|\mathcal{M}'(u, x)[v]| &\leq C|u||v|, & |\mathcal{N}'(u, x)[v]| &\leq C|u||v|,
\end{aligned} \tag{1.22}$$

for some constants $C > 0$ which includes the case of the compliance energy when it is expressed as

$$J(\Omega) = \int_\Omega f u_\Omega \, \mathrm{d}x + \int_{\Gamma_N} g_N \cdot u_\Omega \, \mathrm{d}s(x).$$

Yet using additional frictional contact terms, it is not clear whether this expression takes properly into account the elastic strain energy or not and we prefer to use the following formulation

$$J(\Omega) = \int_\Omega \frac{1}{2} A\varepsilon(u_\Omega) : \varepsilon(u_\Omega)\mathrm{d}x,$$

which unfortunately does not meet the above conditions. However, as we will see later, these conditions are not necessary to obtain the existence of the shape derivatives of the criteria we use.

Let $\mathcal{D} \subset \mathbb{R}^d$ be a fixed bounded and smooth domain whose boundary is split into Γ_C and Γ_D supposed in our case to be some fixed non-optimizable boundaries. Let Ω_{ad} be the admissible set composed of all smooth open domains Ω having Γ_C and Γ_D as parts of its boundary and having an additional optimizable boundary Γ_N (see Figure 1.1)

$$\Omega_{ad} := \{\Omega \subset \mathcal{D} | \Omega \text{ open and of class } \mathscr{C}^1, \Gamma_C \subset \overline{\Omega}, \Gamma_D \subset \overline{\Omega}\}.$$

Then, the shape optimization consists in finding some domains $\Omega \in \Omega_{ad}$ minimizing the target criterion $J(\Omega)$ with a volume constraint.

Note that we use the following notation of the directional derivative of an element A with respect to x in the direction y:

$$\mathcal{D}_x A(x)[y] = \lim_{\epsilon \to 0} \frac{A(x + \epsilon y) - A(x)}{\epsilon}.$$

1.3.1   Shape derivative

The differentiation with respect to the domain aims at modifying the reference state of the domain $\Omega \in \Omega_{ad}$ using the boundary method first described by J. Hadamard in [41] and then developed for instance in [54], [74], [83], [93] and [97]. Let $\Theta \in W^{1,\infty}(\mathbb{R}^d; \mathbb{R}^d) \cap \mathscr{C}^1(\mathbb{R}^d)$ be a vector field displacing the reference domain Ω towards different admissible shapes $\Omega_t \in \Omega_{ad}$. The domain variation in the direction $t\Theta$ reads for t small:

$$\Omega_t = (Id + t\Theta)(\Omega).$$

The shape derivative $\mathcal{D}\, J(\Omega)[\Theta]$ of $J(\Omega)$ with respect to the reference domain Ω in the direction Θ is defined as the derivative on $t = 0$ of the application $t \mapsto J(\Omega_t)$ when it exists and gives

$$J(\Omega_t) = J(\Omega) + t \; \mathcal{D}\, J(\Omega)[\Theta] + o(t).$$

Recall that the shape gradient for general functional in a context of linear elasticity with penalized contact is derived in [69]. We develop the case where Nitsche's method is used to deal with the contact although the contact boundary Γ_C is not optimized.

Theorem 4. *Let $\Omega \in \mathscr{C}^2$ and assume that $f \in H^1(\Omega; \mathbb{R}^d)$, $g_N \in H^2(\Omega; \mathbb{R}^d)$ and that (1.14) or (1.18) admits a unique solution $u_{\Omega_t} \in H^1(\Omega_t; \mathbb{R}^d)$ for t small enough and $\Theta \in W^{1,\infty}(\mathbb{R}^d; \mathbb{R}^d)$. If we denote $\mathcal{D}\, J(\Omega)[\Theta]$ the Gâteaux derivative of $J(\Omega)$ with respect to Ω in the direction $\Theta \in W^{1,\infty}(\mathbb{R}^d; \mathbb{R}^d)$ and $p_\Omega \in V$ defined as the solution of*

$$a(q, p) + \mathcal{D}_u \mathcal{I}(u_\Omega, p, n)[q] = \ell_{u_\Omega}(q), \qquad \forall q \in V, \tag{1.23}$$

where

$$\ell_{u_\Omega}(q) = -\int_\Omega \mathcal{D}_u \mathcal{M}(u_\Omega, x)[q]\mathrm{d}x - \int_{\partial\Omega} \mathcal{D}_u \mathcal{N}(u_\Omega, x)[q]\mathrm{d}s(x),$$

we have when this derivative exists and for $u_\Omega, p_\Omega \in H^2(\Omega, \mathbb{R}^d)$:

$$
\begin{aligned}
\mathcal{D}\, J(\Omega)[\Theta] \;=\; & \int_{\Gamma_m} (\Theta \cdot n)\, (\mathcal{M}(u_\Omega, x) + A\varepsilon(u_\Omega) : \varepsilon(p_\Omega) - f(x) \cdot p_\Omega)\, \mathrm{d}s(x) \\
& + \int_{\Gamma_m} (\Theta \cdot n)\, (\kappa_m\, \mathcal{N}(u_\Omega, x) + \nabla\mathcal{N}(u_\Omega, x) \cdot n)\, \mathrm{d}s(x) \\
& - \int_{\Gamma_m \cap \Gamma_N} (\Theta \cdot n)\, (\kappa_m\, p_\Omega \cdot g_N + (\nabla(p_\Omega \cdot g_N)) \cdot n)\, \mathrm{d}s(x).
\end{aligned}
$$

where Γ_m is a moving boundary of Ω, assuming $\Gamma_m \cap \Gamma_C = \Gamma_m \cap \Gamma_D = \emptyset$, κ_m is the mean curvature of $\partial\Omega$.

Remark 5. *As explained previously, the existence of adjoint state problem requires that the applications $q \mapsto \mathcal{D}_u \mathcal{M}(u_\Omega, x)[q]$ and $q \mapsto \mathcal{D}_u \mathcal{N}(u_\Omega, x)[q]$ must be continuous in V, which is clearly the case under assumptions (1.22). However, these conditions are sufficient but not necessary to verify these continuity properties.*

We develop now the Lagrangian method introduced by J. Céa [18] which aims at describing a constrained optimization problem. To this end, we first present two useful results: let Ω be a bounded open and regular set from $\mathbb{R}^d$.

- Let $f \in H^1(\Omega)$ and let the application $J : \Omega_{\mathrm{ad}} \mapsto \mathbb{R}$ defined by

$$J(\Omega) = \int_{\Omega} f(x)\, \mathrm{d}x.$$

  Then J is differentiable with respect to Ω in the direction $\Theta \in \mathscr{C}^1(\mathbb{R}^d, \mathbb{R}^d)$ and

$$\mathcal{D}\,J(\Omega)[\Theta] = \int_{\partial\Omega} \Theta \cdot n\, f(x)\, \mathrm{d}s(x).$$

- Let $g \in H^1(\Omega)$ and let the application $J : \Omega_{\mathrm{ad}} \mapsto \mathbb{R}$ defined by

$$J(\Omega) = \int_{\partial\Omega} g(x)\, \mathrm{d}s(x).$$

  Then J is differentiable in Ω and for all $\Theta \in \mathscr{C}^1(\mathbb{R}^d\, \mathbb{R}^d)$ and

$$\mathcal{D}\,J(\Omega)[\Theta] = \int_{\partial\Omega} \Theta \cdot n\, (\nabla g(x) \cdot n + \kappa_m g(x))\, \mathrm{d}s(x).$$

Proof of theorem (4):
We intend to minimize the criterion $J(\Omega)$ given by (1.21) under the constraint that the weak formulation (1.14) or (1.18) is satisfied. Let $\mathcal{L}$ the Lagrangian application defined by

$$\mathcal{L}(u, v, n, \Omega) = J(\Omega, u) + (a(u,v) + \mathcal{I}(u,v,n) - \ell(v)).$$

where $J(\Omega, u) = \displaystyle\int_{\Omega} \mathcal{M}(u,x)\, \mathrm{d}x + \int_{\partial\Omega} \mathcal{N}(u,x)\, \mathrm{d}s(x)$. The key is to remark that $J(\Omega) = J(\Omega, u_\Omega)$ and then to identify $J(\Omega)$ as

$$J(\Omega) = \mathcal{L}(u_\Omega, v, n, \Omega).$$

If $\mathcal{L}$ is differentiated with respect to the domain Ω in the direction Θ, it gives

$$\begin{aligned}
\mathcal{D}\,J(\Omega)[\Theta] &= \mathcal{D}\left[\mathcal{L}(u_\Omega, v, n, \Omega)\right][\Theta] \\
&= \mathcal{D}_\Omega\,\mathcal{L}(u_\Omega, v, n, \Omega)[\Theta \cdot n] + \mathcal{D}_n\,\mathcal{L}(u_\Omega, v, n, \Omega)[\mathcal{D}_\Omega\, n[\Theta]] \quad\quad (1.24)\\
&\quad + \mathcal{D}_u\,\mathcal{L}(u_\Omega, v, n, \Omega), [\mathcal{D}_\Omega\, u_\Omega[\Theta]].
\end{aligned}$$

Yet $\mathcal{D}_\Omega\, u_\Omega[\Theta]$ can not be explicitly calculated. In order to vanish the last term of equation (1.24) and obtain an explicit formulation of the shape derivative of J, the idea is to follow

the method of the adjoint state introduced by J.-L. Lions in [66]. More precisely, let $p_\Omega \in V$ be defined as the solution of

$$\mathcal{D}_u \, \mathcal{L}(u_\Omega, p_\Omega, n, \Omega)[q] \; = 0, \; \forall q \in V. \tag{1.25}$$

Then, evaluating the equation (1.24) at $v = p_\Omega$ shows that

$$\mathcal{D} \, \mathcal{L}(u_\Omega, p_\Omega, n, \Omega)[\Theta] \; = \; \mathcal{D}_\Omega \, \mathcal{L}(u_\Omega, p_\Omega, n, \Omega)[\Theta \cdot n]$$
$$+ \mathcal{D}_n \, \mathcal{L}(u_\Omega, p_\Omega, n, \Omega)[\mathcal{D}_\Omega \, n[\Theta]],$$

as $\mathcal{D}_\Omega \, u_\Omega[\Theta] \in V$. Moreover, the term $\mathcal{D}_u \, \mathcal{L}(u, p, n, \Omega)[q]$ can be identified as

$$\mathcal{D}_u \, \mathcal{L}(u, p, n, \Omega)[q] = a(q, p) + \mathcal{D}_u \, \mathcal{I}(u, p, n)[q]$$
$$+ \int_\Omega \mathcal{D}_u \, \mathcal{M}(u, x)[q] \, \mathrm{d}x + \int_{\partial\Omega} \mathcal{D}_u \, \mathcal{N}(u, x)[q] \, \mathrm{d}s(x).$$

This leads to the following explicit expression of the shape gradient in linear elasticity:

$$\mathcal{D} \, J(\Omega)[\Theta] \; = \; \int_{\Gamma_m} (\Theta \cdot n) \, (\mathcal{M}(u_\Omega, x) + A\varepsilon(u_\Omega) : \varepsilon(p_\Omega) - f(x) \cdot p_\Omega) \, \mathrm{d}s(x)$$
$$+ \int_{\Gamma_m} (\Theta \cdot n) \, (\kappa_m \, \mathcal{N}(u_\Omega, x) + \nabla \mathcal{N}(u_\Omega, x) \cdot n) \, \mathrm{d}s(x)$$
$$- \int_{\Gamma_m \cap \Gamma_N} (\Theta \cdot n) \, (\kappa_m \, p_\Omega \cdot g_N + (\nabla(p_\Omega \cdot g_N)) \cdot n) \, \mathrm{d}s(x),$$

as $\Gamma_m \cap \Gamma_C = \emptyset$ and $\mathcal{I}(u, p, n)$ is an integral term defined on Γ_C.

$\square$

Remark 6. *In case where the Neumann condition g_N corresponds to a pressure term, the latter depends on n since $g_N = -p^{hl} n$ where p^{hl} is the constant pressure. The shape gradient reads then*

$$\mathcal{D} \, J(\Omega)[\Theta] \; = \; \int_{\Gamma_m} (\Theta \cdot n) \, (\mathcal{M}(u_\Omega, x) + A\varepsilon(u_\Omega) : \varepsilon(p_\Omega) - f(x) \cdot p_\Omega) \, \mathrm{d}s(x)$$
$$+ \int_{\Gamma_m} (\Theta \cdot n) \, (\kappa_m \, \mathcal{N}(u_\Omega, x) + \nabla \mathcal{N}(u_\Omega, x) \cdot n) \, \mathrm{d}s(x)$$
$$+ \int_{\Gamma_m \cap \Gamma_N} (\Theta \cdot n) \, p^{hl}(\kappa_m \, p_\Omega \cdot n + (\nabla(n \cdot p_\Omega)) \cdot n) \, \mathrm{d}s(x)$$
$$+ \int_{\Gamma_m \cap \Gamma_N} \frac{\partial p^{hl} n \cdot p_\Omega}{\partial n} \cdot n'(\Theta) \, \mathrm{d}s(x),$$

where $n'(\Theta) = -\nabla_t(\Theta \cdot n) = -\nabla(\Theta \cdot n) + (\Theta \cdot n)n$. Recalling the following integration by parts, if Ω is a closed and regular set of $\mathbb{R}^d$, $f \in W^{2,1}(\mathbb{R}^d, \mathbb{R}^d)$ and for all $\Theta \in W^{1,\infty}(\mathbb{R}^d, \mathbb{R}^d)$:

$$\int_\Gamma f \mathrm{div}_\Gamma \Theta \, \mathrm{d}s(x) = \int_\Gamma ((\Theta \cdot n)(f\kappa_m) - \nabla_t f \cdot \Theta) \, \mathrm{d}s(x),$$

where $\mathrm{div}_\Gamma \Theta = \mathrm{div}\,\Theta - \nabla(\Theta \cdot n) \cdot n$, *which gives*

$$
\begin{aligned}
\mathcal{D}\,J(\Omega)[\Theta] = & \int_{\Gamma_m} (\Theta \cdot n)\,(\mathcal{M}(u_\Omega, x) + A\varepsilon(u_\Omega) : \varepsilon(p_\Omega) - f(x) \cdot p_\Omega)\,\mathrm{d}s(x) \\
& + \int_{\Gamma_m} (\Theta \cdot n)\,(\kappa_m\,\mathcal{N}(u_\Omega, x) + \nabla\mathcal{N}(u_\Omega, x) \cdot n)\,\mathrm{d}s(x) \\
& + \int_{\Gamma_m \cap \Gamma_N} (\Theta \cdot n)\,p^{hl}(\kappa_m\,p_\Omega \cdot n + (\nabla(n \cdot p_\Omega)) \cdot n)\,\mathrm{d}s(x) \\
& - \int_{\Gamma_m \cap \Gamma_N} (\Theta \cdot n)\,p^{hl}(\kappa_m p_\Omega \cdot n - \mathrm{div}_\Gamma p_\Omega)\,\mathrm{d}s(x),
\end{aligned}
$$

and it finally holds, in case of pressure term for the Neumann condition:

$$
\begin{aligned}
\mathcal{D}\,J(\Omega)[\Theta] = & \int_{\Gamma_m} (\Theta \cdot n)\,(\mathcal{M}(u_\Omega, x) + A\varepsilon(u_\Omega) : \varepsilon(p_\Omega) - f(x) \cdot p_\Omega)\,\mathrm{d}s(x) \\
& + \int_{\Gamma_m} (\Theta \cdot n)\,(\kappa_m\,\mathcal{N}(u_\Omega, x) + \nabla\mathcal{N}(u_\Omega, x) \cdot n)\,\mathrm{d}s(x) \\
& + \int_{\Gamma_m \cap \Gamma_N} (\Theta \cdot n)\,p^{hl}\mathrm{div}\,(p_\Omega)\,\mathrm{d}s(x).
\end{aligned}
$$

1.3.2   Contact term

In this section, we give an explicit formulation of the contact term and its directional derivative in the adjoint equation.

Case of the penalty method

In this case, we have $\mathcal{I}(u, v, n) = \mathcal{I}_P(u, v, n)$ defined by (1.15). The derivative term $\mathcal{D}_u\,\mathcal{I}_\mathcal{P}(u, p, n)[q]$ from (1.23) can then be developed as

$$
\mathcal{D}_u\,\mathcal{I}_P(u, p, n)[q] = -\int_{\Gamma_C} \left(\gamma\,H(-(g - u_n))q_n\,p_n + \mathcal{D}_u\,P_{\mathcal{B}(n_y, \rho(u))}(\gamma u)\,\gamma q_t \cdot p_t\right)\,\mathrm{d}s(x),
$$

where H is the Heaviside function defined by $H(x) = 1$ for $x \geq 0$ and $H(x) = 0$ otherwise. Moreover, the computation of $\mathcal{D}_u\,P_{\mathcal{B}(n, \rho(u))}((\gamma u))$ is obtained thanks to the the partial derivatives of the projection ball $P_{\mathcal{B}(n, \tau)}(q)$ according to q and τ. Indeed, it reads (see [84])

$$
\partial_q P_{\mathcal{B}(n, \tau)}(q) = \begin{cases} 0 & \text{for } \tau \leq 0, \\ T_n & \text{if } |q_t| \leq \tau, \\ \frac{\tau}{|q_t|}\left(T_n - \frac{q_t}{|q_t|} \otimes \frac{q_t}{|q_t|}\right) & \text{otherwise,} \end{cases}
$$

and

$$\partial_\tau P_{\mathcal{B}(n,\tau)}(q) = \begin{cases} 0 & \text{for } \tau \le 0 \text{ or } |q_t| \le \tau, \\ \frac{q_t}{|q_t|} & \text{otherwise,} \end{cases}$$

Where T_n is defined by $T_n = I_d - n \otimes n$, $q_t = T_n q$. We refer to [19] for the differentiability of the penalty approach.

Case of Nitsche's approach

Concerning Nitsche's method, we now have $\mathcal{I}(u, v, n) = \mathcal{I}_N(u, v, n)$ defined by (1.19). The directional derivative $\mathcal{D}_u \mathcal{I}_N(u, p, n)[q]$ from (1.23) has the following form

$$\begin{aligned}
\mathcal{D}_u \mathcal{I}_N(u, p, n)[q] &= \int_{\Gamma_C} \left(-\frac{\theta}{\gamma}\sigma_n(q)\sigma_n(p) \ - \frac{\theta}{\gamma}\sigma_t(q) \cdot \sigma_t(p)\right. \\
&+ \frac{1}{\gamma} H(-(\sigma_n(u) - \gamma(u_n - g)))(\sigma_n(q) - \gamma q_n)(\theta\,\sigma_n(p) - \gamma p_n) \\
&+ \left.\frac{1}{\gamma} \mathcal{D}_u P_{\mathcal{B}(n_y, \rho(u))}(\sigma(u)n - \gamma u)(\sigma_t(q) - \gamma q_t) \cdot (\theta\,\sigma_t(p) - \gamma p_t)\right) \mathrm{d}s(x).
\end{aligned} \tag{1.26}$$

Remark 7. *Note that the term $\mathcal{D}_u \mathcal{I}_N(u, p, n)[q]$ is not clearly defined in the continuous framework because of the possible lack of regularity of u_Ω and p_Ω. In this chapter, we focus only on the discrete case which does not pose any existence problem. The analysis of the convergence of the solutions of the discrete problem will be addressed in the next chapter where we discover by the way that the above term (1.26) does not lead to a consistent adjoint state formulation.*

1.3.3   Criterion minimization

The main energy that is to be minimized, namely the elastic strain energy and defined by (1.3) can then be expressed in the general form (1.21) by considering

$$\mathcal{M}(u_\Omega^i, x) = \frac{1}{2} A\varepsilon(u_\Omega^i) : \varepsilon(u_\Omega^i) \text{ and } \mathcal{N}(u_\Omega^i, x) = 0.$$

Consequently, the associated term in the adjoint equation of the strain energy criterion (1.3) reads

$$\mathcal{D}_u J_e(\Omega, u_\Omega)[q] = \int_\Omega A\varepsilon(q) : \varepsilon(u_\Omega) \, \mathrm{d}x.$$

Note that a sufficient condition for the adjoint equation to make sense is that $q \mapsto \mathcal{D}_u J_e(\Omega, u_\Omega)[q]$ is continuous in V which is satisfied here even though the term do not meet the conditions (1.22).

An additional criterion developed in this work consists of uniformizing the contact stress on the contact boundary of the rolling structure according to the load positions. As mentioned

in the introduction, a first natural idea would be to minimize the objective function (1.4). However, this expression is possibly difficult to define according to the regularity of u_Ω^i whose basic guaranteed regularity is to be in $H^1(\Omega, \mathbb{R}^d)$. Assuming additionally a square integrable right hand side, the trace $\sigma(u_\Omega)n$ on Γ_C belongs only to $H^{-1/2}(\Gamma_C, \mathbb{R}^d)$ (see [61]) and not necessarily to $L^2(\Gamma_C, \mathbb{R})$ meaning in particular that there is no continuous dependence of the objective function (1.4) with respect to the data of the problem.

Two variants of the criterion will be developed to recover this continuity. A first idea is to thicken the contact boundary of a size ϵ , which leads to the first criterion

$$J_{p,1}(\Omega, u_\Omega, p_{mean}) = \int_{\Gamma_C^\epsilon} \frac{L}{2E\epsilon}(\sigma(u_\Omega)n - p_{mean})^2 \mathrm{d}x, \tag{1.27}$$

where $\epsilon > 0$ is a fixed small length, Γ_C^ϵ is an annulus delimited by Γ_C on the exterior and of thickness ϵ and n is an extension in the domain Γ_C^ϵ of the unit outward normal vector on Γ_C. A second idea is to consider a criterion depending on the $H^{-1/2}(\Gamma_C, \mathbb{R}^d)-$norm by considering the energy

$$J_{p,2}(\Omega, u_\Omega, p_{mean}) = \frac{1}{2}\|\sigma(u_\Omega)n - p_{mean}\|_{-1/2,\Gamma_C}^2, \tag{1.28}$$

where here and in the rest of this work, $\| \cdot \|_{s,\omega}$ stands for the $H^s(\omega)-$norm.

In order to simplify the minimization of $J_{p,1}$ and $J_{p,2}$, we treat the computation of p_{mean} by freezing it to the value at the previous optimization step. It has the advantage to uncouple the computation of the adjoint problem on each load position.

Uniformity of the contact stress on the thickened boundary

As explained previously, a first strategy consists in thickening the contact boundary with a size ϵ which leads to the criterion (1.27). It can be expressed in the general form (1.21) with

$$\mathcal{M}(u_\Omega, x) = \frac{L}{2E\epsilon}(\sigma(u_\Omega)n - p_{mean})^2 \, \chi_{\Gamma_C^\epsilon}(x) \ \text{ and } \ \mathcal{N}(u_\Omega, x) = 0,$$

where $\chi_{\Gamma_C^\epsilon}(x) = \begin{cases} 1 & \text{if } x \in \Gamma_C^\epsilon, \\ 0 & \text{otherwise} \end{cases}$. In that case, the associated term in the adjoint equation of the contact stress criterion from equation (1.27), assuming p_{mean} known in advance, reads as

$$\mathcal{D}_u \, J_{p,1}(\Omega, u_\Omega, p_{mean})[q] = \int_{\Gamma_C^\epsilon} \frac{L}{E\epsilon}(\sigma(u_\Omega)n - p_{mean}) \cdot \sigma(q)n \, \mathrm{d}x.$$

Note that in this case, $q \mapsto \mathcal{D}_u \, J_{p,1}(\Omega, u_\Omega, p_{mean})[q]$ is continuous on V.

Uniformity of contact stress using a $H^{-1/2}(\Gamma_C, \mathbb{R}^d)-$norm

The second strategy consists in minimizing the functional (1.28). It can be expressed constructively using a Neumann to Dirichlet operator (see for instance [85] and [2]). Indeed, let $\mathcal{B}$ be a fixed domain whose boundary is decomposed as the union of Γ_C and Γ_D. We first introduce the norm $\|\cdot\|_{H_{00}^{1/2}(\Gamma_C, \mathbb{R}^d)}$ defined by

$$\|w\|_{H_{00}^{1/2}(\Gamma_C, \mathbb{R}^d)} = \inf_{z \in V_0, z=w \text{ on } \Gamma_C} \|z\|_{V_0},$$

where $V_0 = \{v \in H^1(\mathcal{B}; \mathbb{R}^d), v = 0 \text{ on } \Gamma_D\}$ and

$$\|z\|_{V_0}^2 = \int_{\mathcal{B}} A\, \varepsilon(z) : \varepsilon(z) \, \mathrm{d}x.$$

The norm $\|\cdot\|_{-1/2,\Gamma_C}$ is then defined as the dual of $\|\cdot\|_{H_{00}^{1/2}(\Gamma_C, \mathbb{R})}$ by

$$\|g\|_{-1/2,\Gamma_C} = \sup_{z \in H_{00}^{1/2}(\Gamma_C, \mathbb{R}), z \neq 0} \frac{\langle g, z \rangle}{\|z\|_{H_{00}^{1/2}(\Gamma_C, \mathbb{R})}} = \sup_{z \in V_0} \frac{\langle g, z \rangle}{\|z\|_{V_0}}.$$

In particular, we can show that

$$\|g\|_{-1/2,\Gamma_C} = \|w[g]\|_{V_0},$$

where $w[g] \in V_0$ is defined as the solution of

$$\begin{cases} -\operatorname{div} \sigma(w) = 0 & \text{in } \mathcal{B} \text{ where } \sigma(w) = A\, \varepsilon(w), \\ \sigma(w)n = g & \text{on } \Gamma_C, \\ w = 0 & \text{on } \Gamma_D. \end{cases} \tag{1.29}$$

The weak formulation of (1.29) reads as

$$\int_{\mathcal{B}} A\, \varepsilon(w[g]) : \varepsilon(z) \, \mathrm{d}x = \langle g, z \rangle, \forall z \in V_0,$$

which shows also by using $z = \omega[g]$ that $\omega[g]$ satisfies

$$\frac{1}{2} \int_{\mathcal{B}} A\varepsilon(\omega[g]) : \varepsilon(\omega[g]) \, \mathrm{d}x = \langle g, \omega[g] \rangle = \int_{\Gamma_C} g \cdot \omega[g] ds(x).$$

Using these equalities, the criterion for the uniformization of the contact stress finally reads

$$\begin{aligned} J_{p,2}(\Omega, u_\Omega, p_{mean}) &= \frac{1}{2} \|\sigma(u_\Omega)n - p_{mean}\|_{-1/2,\Gamma_C}^2 = \frac{1}{2} \|w_\Omega\|_{V_0}^2 \\ &= \frac{1}{2} \int_{\mathcal{B}} \sigma(w_\Omega) : \varepsilon(w_\Omega) \, \mathrm{d}x = \frac{1}{2} \int_{\Gamma_C} g \cdot w_\Omega \, ds(x) \\ &= \frac{1}{2} \int_{\Gamma_C} (\sigma(u_\Omega)n - p_{mean}) \cdot w_\Omega \, ds(x). \end{aligned}$$

where $w_\Omega = \omega[\sigma(u_\Omega)n - p_{mean}]$ is the solution to (1.29) for $g = \sigma(u_\Omega)n - p_{mean}$.

Still assuming p_{mean} known in advance, the associated term in the adjoint equation of the $H^{-1/2}(\Gamma_C, \mathbb{R}^d)-$norm criterion reads

$$
\begin{aligned}
\mathcal{D}_u\, J_{p,2}(\Omega, u_\Omega, p_{mean})[q] &= \frac{1}{2} \int_\Omega \mathcal{D}_u\, A\varepsilon(w_\Omega)^2[q]\ \mathrm{d}x \\
&= \int_\Omega A\varepsilon(w_\Omega) : \varepsilon(w[\sigma(q)n])) \ \mathrm{d}x \\
&= \int_{\Gamma_C} \sigma(q)n \cdot w_\Omega \ \mathrm{d}s(x),
\end{aligned}
$$

where $w[\sigma(q)n]$ is defined as the solution to (1.29) for $g = \sigma(q)n$. As previously, the existence of the adjoint would expect the continuity of $q \mapsto \mathcal{D}_u\, J_{p,2}(\Omega, u_\Omega, p_{mean})[q]$ in V which is not satisfied but is the case in a subspace $H_\sigma = \{v \in V : \mathrm{div}(\sigma(v)) \in L^2(\Omega)\}$ containing the solutions of the contact problem.

Remark 8. *The Dirichlet to Neumann operator can also be defined by an intermediary Poisson problem instead of the elasticity problem (1.29). The preference given here to the elasticity problem is guided by mechanical considerations.*

1.4   Numerical strategy

The aim of this section is to introduce the optimization method to minimize the objective function given by (1.5) and (1.6). Since the optimization is to be performed on the whole structure, it would be necessary to make computations for all the load positions. In order to save some computational time, we assume a certain periodicity of the structure, using its axisymmetry, and we perform computations only for the load positions corresponding to a single sector of the structure. The structure is divided into $N_s = 16$ sectors (see Figure 1.4) and we perform the computations on N_d load positions corresponding to only one sector, regularly spaced in rotations of angles $i2\pi/(N_d \times N_s)$ for i from 1 to N_d. Then the computations for the load positions corresponding to the other sectors are deduced by a simple rotation, so that we obtain at the end the computations for $N_l = N_d \times N_s$ load positions. In practice, the load is imposed using Dirichlet boundary conditions on the entire Γ_D boundary in the direction n_y, i.e. $u = \alpha_D n_y$, where the constant α_D is determined to obtain an overall load of 300 kg. A more precise description is the subject of section 1.4.2.
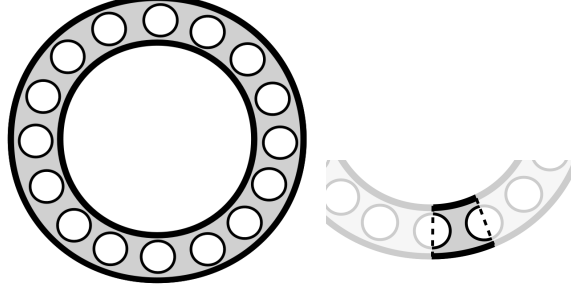
Figure 1.4: Periodicity of the domain Ω. On the left: the domain drilled by 16 circular holes and on the right: focus on the sector corresponding to the load positions for which computations are performed.

We consider a minimizing sequence Ω^k of J starting from an initial domain Ω^0 and taking volume and symmetry constraints into account. From a domain Ω^k, we intend to reach a domain Ω^{k+1} by performing the following steps:

- For each load position on the first sector, for i from 1 to N_d, we compute $u^i_{\Omega^k}$ the solution to the direct non-linear problem (1.14) or (1.18) approximated by a finite element method. The solutions $u^i_{\Omega^k}$ for i from $N_d + 1$ to $N_d \times N_s$ are deduced by rotations of solutions on the first sector.

- The mean contact stress p^k_{mean} is computed on Γ_C:

$$p^k_{mean} = \frac{1}{N_d} \sum_i^{N_d} (\sigma(u^i_{\Omega^k})n).$$

- For each load position on the first sector, for i from 1 to N_d, we compute $p^i_{\Omega^k}$ the solution to the adjoint problem (1.25) approximated by a finite element method. The solutions $p^i_{\Omega^k}$ for i from $N_d + 1$ to $N_d \times N_s$ are also deduced by rotations of solutions on the first sector.

- For each load position, we compute the shape gradient of $J_g(\Omega^k, u^i_{\Omega^k})$ which we harmonically extend into the holes by solving a Poisson equation.

- We sum each term to obtain the shape gradient $\overline{G^k} = \nabla J(\Omega^k)$ of $J(\Omega^k)$ on all the load positions.

- We prescribe the volume to remain constant thanks to a penalization on the gradient as $\tilde{G}^k = G^k - \lambda_k$ where $\lambda_k = 8 * (\max(G^k) - \min(G^k)) * (r_v^0 - r_v^k)$ is the Lagrange multiplier with r_v^k the volume ratio at iteration k.

- We compute the new shape Ω^{k+1} by approximating the equation $\Omega^{k+1} = (I_d - \delta_k \tilde{G}^k)(\Omega^k)$, δ_k being the descent step of the shape optimization.

As an illustration, Figure 1.5 successively depicts the treatments led on the shape gradients: The computation of the shape gradient on a load position, the harmonic extension of that shape gradient, and the summed gradients, periodically repeated on the different sectors and the additional correction for volume constraint. We describe more precisely the finite element method, using cut elements, used to compute the mechanical behavior of such a geometry in section 1.4.3.
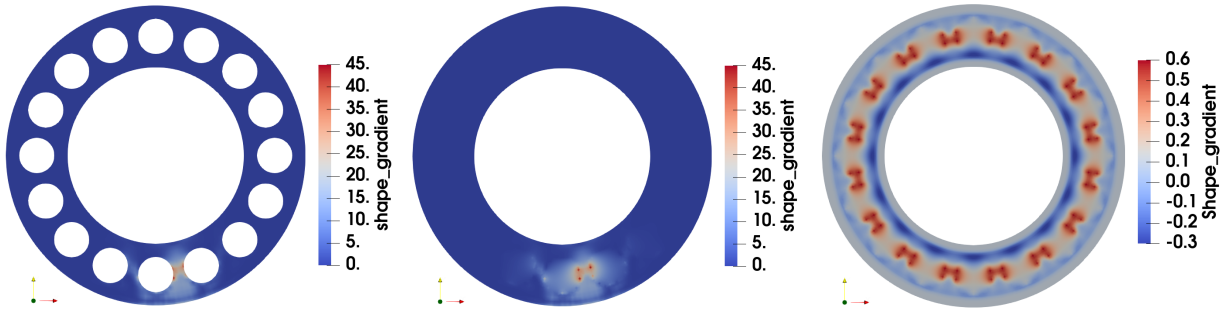
Figure 1.5: Successive shape gradient treatments. Left to right: the shape gradient computed on the cut elements from the solutions u_{Ω^k} and p_{Ω^k}, the harmonic extension of the shape gradient on the complete mesh and the symmetry and volume correction of the shape gradient.

1.4.1 Domain representation and level set function

The level set method has been introduced by S. J. Osher and J. A. Sethian in [79] to describe a geometry and its evolutions. The first applications of the level set method were about geodesics, lithography, generation of minimal surfaces, propagation of flame fronts and fluid interfaces. This method was first introduced for shape optimization applications by S. J. Osher and F. Santosa in [80] and then by G. Allaire et al. in [8] and [9]. Let $\mathcal{D} \subset \mathbb{R}^d$ still being a fixed bounded domain in which the domain Ω is included. The representation of the domain Ω in $\mathcal{D}$ is expressed by a function ψ defined in $\mathcal{D}$ as:

$$\begin{cases} \psi(x) = 0 \text{ if } x \in \partial\Omega, \\ \psi(x) < 0 \text{ if } x \in \Omega, \\ \psi(x) > 0 \text{ otherwise.} \end{cases}$$
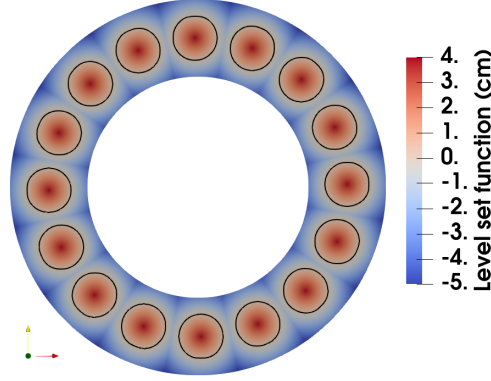
Figure 1.6: Level set representation of the domain.

The interface between holes and matter is represented by the zero value of the level set function. The level set representation and its evolution is more largely treated in appendix A.

1.4.2 Load condition on a rigid rim

Aiming at a model closer to a load-bearing rolling structure, the Dirichlet condition on Γ_D is replaced by a rigid boundary condition (rim) that is only allowed to have a vertical rigid motion and is subject to a global load. Denoting g_D the prescribed load and α_D the unknown vertical rigid displacement on Γ_D, the weak formulation reads now: Find $u \in V, \alpha_D \in \mathbb{R}, \lambda_D \in H^{-1/2}(\Gamma_D)^d$ such that $\forall v \in V, \forall \beta_D \in \mathbb{R}$ and $\forall \mu_D \in H^{-1/2}(\Gamma_D)^d$,

$$a(u,v) + \mathcal{I}(u,v,n) = \int_\Omega f(x) \cdot v \, \mathrm{d}x + \int_{\Gamma_D} (\lambda_D \cdot v + (u - \alpha_D n_y) \cdot \mu_D + (\lambda_D \cdot n_y - g_D)\beta_D) \, \mathrm{d}s(x),$$

where λ_D is a multiplier representing the force density on Γ_D introduced to enforce the condition.

Consequently, a new term is added to the adjoint problem on Γ_D and the two new variables α_D and λ_D are introduced in the Lagrangian. The adjoint problem now reads $\forall q \in V, \forall q_{\alpha_D} \in \mathbb{R}$ and $\forall q_{\lambda_D} \in H^{-1/2}(\Gamma_D)^d$,

$$\mathcal{D}_u \mathcal{L}(u,p,\alpha_D,\lambda_D,n,\Omega)[q] + \mathcal{D}_{\alpha_D} \mathcal{L}(u,p,\alpha_D,\lambda_D,n,\Omega)[q_{\alpha_D}]$$
$$+ \mathcal{D}_{\lambda_D} \mathcal{L}(u,p,\alpha_D,\lambda_D,n,\Omega)[q_{\lambda_D}] = 0,$$

which leads to find $p \in V, p_{\alpha_D} \in \mathbb{R}, p_{\lambda_D} \in H^{-1/2}(\Gamma_D)^d$ such that $\forall q \in V, \forall q_{\alpha_D} \in \mathbb{R}$ and $\forall q_{\lambda_D} \in H^{-1/2}(\Gamma_D)^d$

$$a(q,p) + \mathcal{D}_u \mathcal{I}(u,p,n)[q] = \ell_u(q) + \int_{\Gamma_D} (p_{\lambda_D} \cdot q + (p - p_{\alpha_D} n_y) \cdot q_{\lambda_D} - p_{\lambda_D} \cdot n_y q_{\alpha_D}) \, \mathrm{d}s(x).$$

1.4.3 Finite element discretization and fictitious domains method

To compute each direct and adjoint problem on the evolving domain Ω^k, we use a fictitious domain method with respect to the fixed domain $\mathcal{D}$ containing Ω^k. The fictitious domains method used in this work is close to the Xfem approach proposed first by N. Moës et al. in [72] for crack growths and then for contact stakes in [31, 38, 76]. The fictitious domains method is presented in [52, 16] and applied to the unilateral contact and to Nitsche's method in [35]. One of the main advantages of this method is its optimal convergence, including when a high-order base finite element method is used. It mainly consists in considering a classical finite element method, here a Lagrange P_2 finite element on the polar grid also used for the level set discretization, and taking its restriction on the real domain Ω^k. Consequently, only one fixed, regular and polar grid is manipulated for the level set and the finite element method. As an illustration, Figure 1.7 successively depicts an example of a polar structured mesh of the fictitious domain $\mathcal{D}$, the mesh cut by the level set representing Ω^k and the computed direct solution u_{Ω^k} using a Lagrange P_2 cut finite element method.

The discretized non-linear direct problems are solved with a non-smooth Newton-Raphson algorithm. The finite element software used for the analysis is GetFEM++ [87] with its python interface.
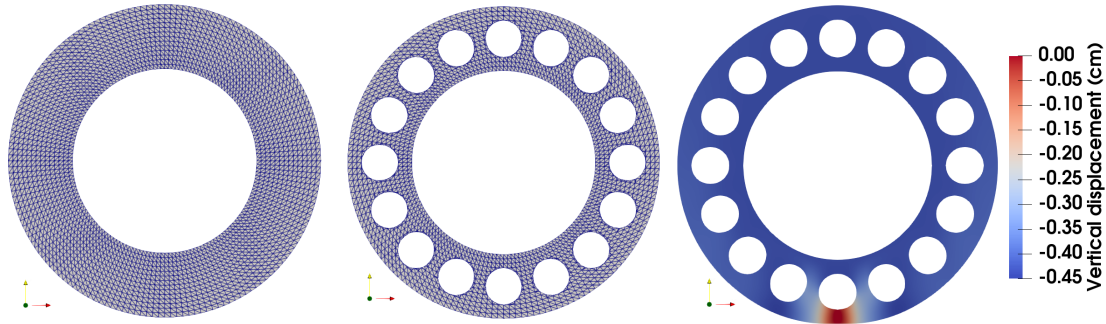
Figure 1.7: Left to right: the structured polar mesh, the mesh cut by the level set representing Ω^k and a direct solution u_{Ω^k} plot on the deformed mesh.

It has been noted in [52, 16] that an optimal approximation of the gradient of the solution is not achieved in the cut element method without the addition of a stabilization term, mainly on elements having a very small intersection with the real domain Ω^k, as illustrated in Figure 1.8. Since the calculation of the shape gradient requires the computation of the gradient of the displacement on the level set itself, we added a stabilization term to ensure a good quality of the approximation. We have chosen to use the so-called ghost penalty method proposed by E. Burman and P. Hansbo in [15]. It aims at penalizing some inter-element jumps, on the elements cut by the level set. It consists in adding a stabilization term to the

direct problem which then reads

$$
\begin{cases}
\text{Find } u^h \in V^h \text{ such that } \forall v^h \in V^h, \\
a(u^h, v^h, N) + \mathcal{I}(u^h, v^h, N) + G(u^h, v^h, N) = \ell(v^h),
\end{cases}
$$

where G is the ghost penalty term

$$
G(u, v, n) = \sum_{E \in \mathcal{E}^k} \frac{1}{2} \int_E \frac{\xi}{\gamma} [\![\sigma(u)n]\!] \cdot [\![\sigma(v)n]\!] \, \mathrm{d}s(x),
$$

where $\mathcal{E}^k$ denotes the set of edges (for $d = 2$) or faces (for $d = 3$) of the mesh having a non empty intersection with $\partial \Omega^k$, $[\![\sigma(u) \cdot n]\!]$ denotes the inter-element stress jump over E, n is a unit normal vector to E and ξ is the penalty parameter. The same term is imposed in the adjoint equation (1.23) and reads

$$
\mathcal{D}_u \, G(u, p, n)[q] = \sum_{E \in \mathcal{E}^k} \frac{1}{2} \int_{\partial T} \frac{\xi}{\gamma} [\![\sigma(q)n]\!] \cdot [\![\sigma(p)n]\!] \, \mathrm{d}s(x).
$$
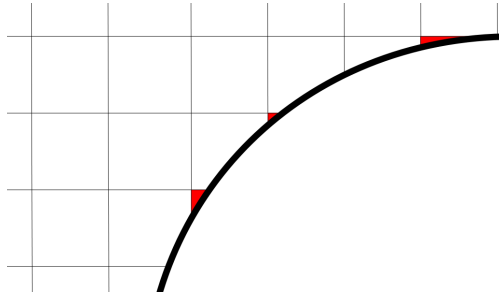
Figure 1.8: Example of a structured mesh at the interface with a hole. The red areas depict cut elements having a small intersection with the domain Ω^k where the gradient of the solution may be of poor quality.
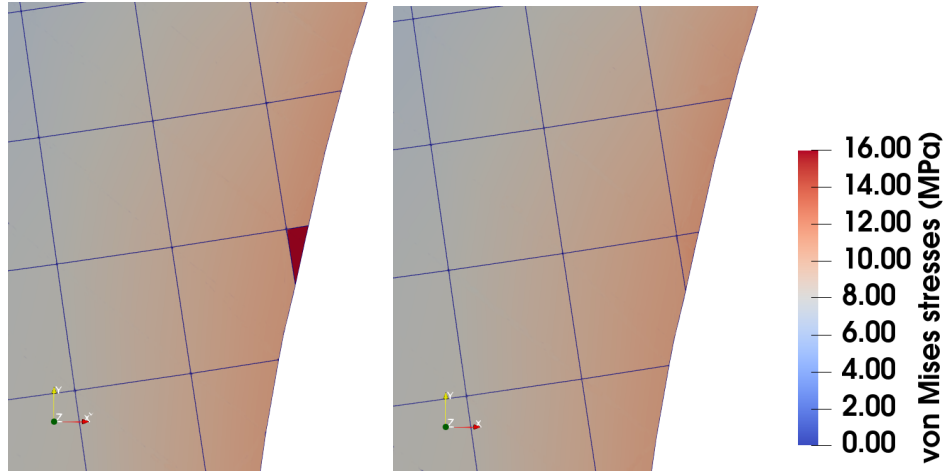
Figure 1.9: Focus on the von Mises stress of two solutions of the direct problem near a hole. On the left the stress jump is not penalized to compute the solution ($\xi = 0$) and on the right the stress jump is penalized ($\xi = 10^{-3}$).

To illustrate the influence of the stabilization parameter, Figure 1.9 shows that the stress (here the von Mises stress) can be badly estimated on the elements having a very small intersection with the real domain in the absence of a stabilization term ($\xi = 0$), whereas the application of a small stabilization term ($\xi = 10^{-3}$) allows to recover a good approximation. In the following, all the computations are performed with a penalization parameter $\xi = 10^{-3}$.

1.5   Numerical experiments

In this section, we present a set of numerical tests, beginning with a simple initial geometry. The objective is successively to evaluate the difference in behavior of the penalty and Nitsche methods for the approximation of the contact condition, and to evaluate the different criteria of uniformization of the contact force density. Finally, we illustrate the shape optimization on more complex initial geometries.

1.5.1   Geometry setting

We consider the domain as a ring with an inner radius $R_i = 20$ cm and an outer radius $R_e = 34$ cm containing sixteen regularly spaced holes of radius $r = 4$ cm (see Figure 1.10). The ring width is set to $w_r = 12$ cm. The domain is divided in $N_s = 16$ sectors for periodic simplification. We compute $N_d = 8$ mechanical load positions per sector.
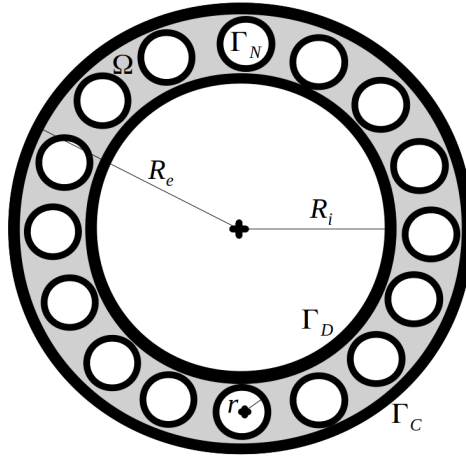
Figure 1.10: Schematic representation of the domain.

The Young modulus is set to $E = 200$ MPa and the Poisson ratio is $\nu = 0.48$. A contact might occur on the boundary Γ_C upon the outer radius R_e with a flat rigid body representing the ground. A load condition is set on the rigid boundary Γ_D upon the inner radius R_i and the load is supposed to be 300 kg.

1.5.2 Minimization of the sole elastic strain energy

A first optimization is performed on the simple initial geometry with only a minimization of the elastic strain energy J_e. The result is presented in Figure 1.11 for a contact condition approximated by Nitsche's method with parameters $\gamma = E/h_T$ and $\theta = -1$.
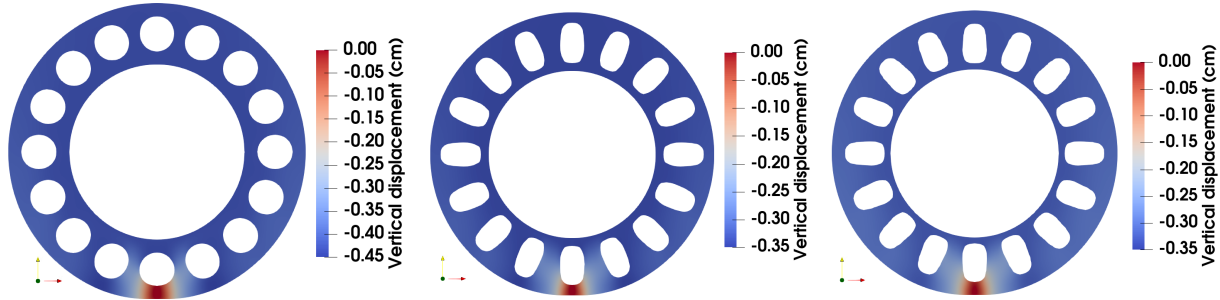
Figure 1.11: Shape optimization for the sole strain energy. The vertical displacement is displayed. Contact treated by Nitsche's method. From left to right: first iteration, 20th iteration and 100th iteration.

The circular holes progressively radially lengthen along the optimization process to bring stiffness and to reduce deformation whatever the load position is. The evolution of the objective function J_e is presented in Figure 1.12.
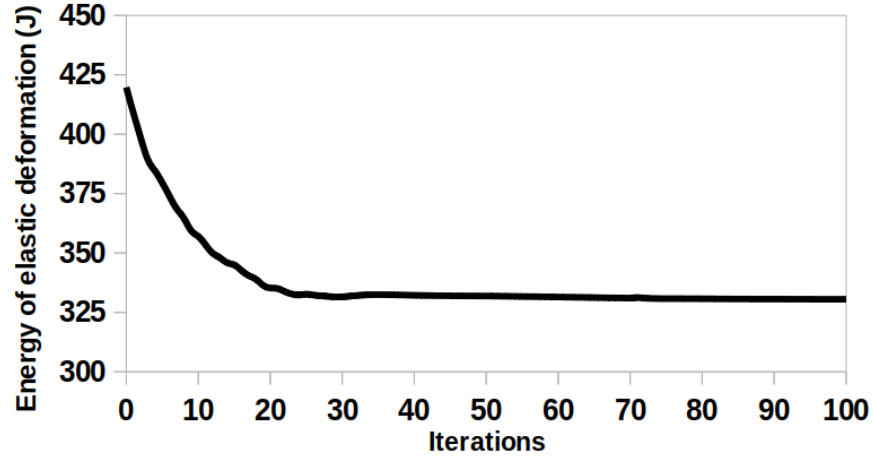
Figure 1.12: Evolution of the elastic strain energy J_e for the configuration presented in Figure 1.11 according to the successive iterations of the shape optimization algorithm.

1.5.3 Comparison of contact methods for the geometric shape optimization

In order to compare the two strategies to account for the contact condition, the test of the previous section is now performed using the penalty method to treat the contact. The penalty parameter is also taken equal to $\gamma = E/h_T$. The result of the shape optimization is shown in Figure 1.13.
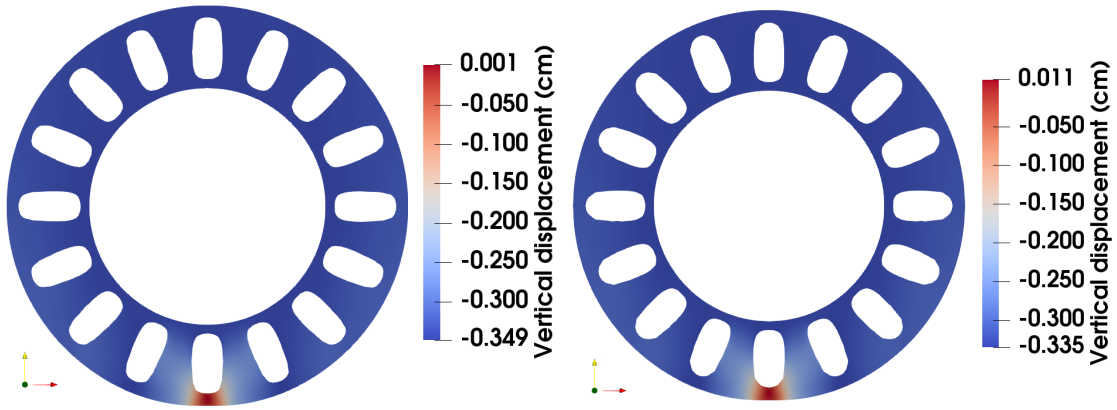
Figure 1.13: Optimal shapes for different contact methods. On the left: optimal shape with the contact treated by penalization and on the right: optimal shape with the contact treated by Nitsche's method.

It can be noted, comparing with Figure 1.11 that both methods almost lead to the same

final and optimal shape. A very careful comparison in Figure 1.13 shows that the solution with penalty corresponds to a slightly higher deflection of the structure.

The difference is more significant in Figure 1.14 where a comparison of the evolution of elastic strain energy is plotted for the two methods. With the penalty, the elastic strain energy is underestimated because of the interpenetration.
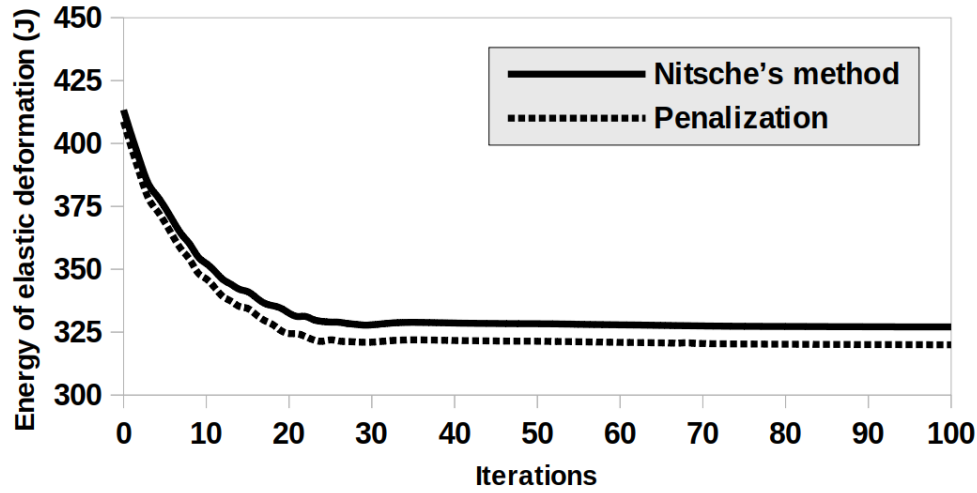
Figure 1.14: Evolution of the strain energy J_e during the shape optimization: comparison between Nitsche's method and penalization.

To overcome this drawback, the penalty parameter γ might be increased so that the contact would be better estimated. Two other tests are performed with $\gamma = 10E/h_T$ for both methods. The optimal shape and deformation obtained can be seen in Figure 1.15.
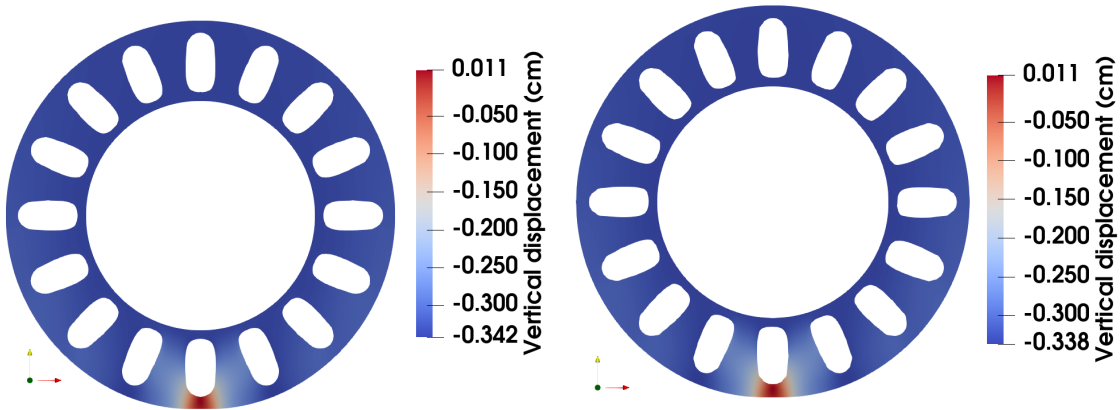
Figure 1.15: Optimal shapes for different contact methods. $\gamma = 10E/h_T$. On the left: optimal shape with the contact treated by penalization and on the right: optimal shape with the contact treated by Nitsche's method.

The two deformations are very close to each other in that case and the evolution of the strain energy, plotted in Figure 1.16 is also almost the same.
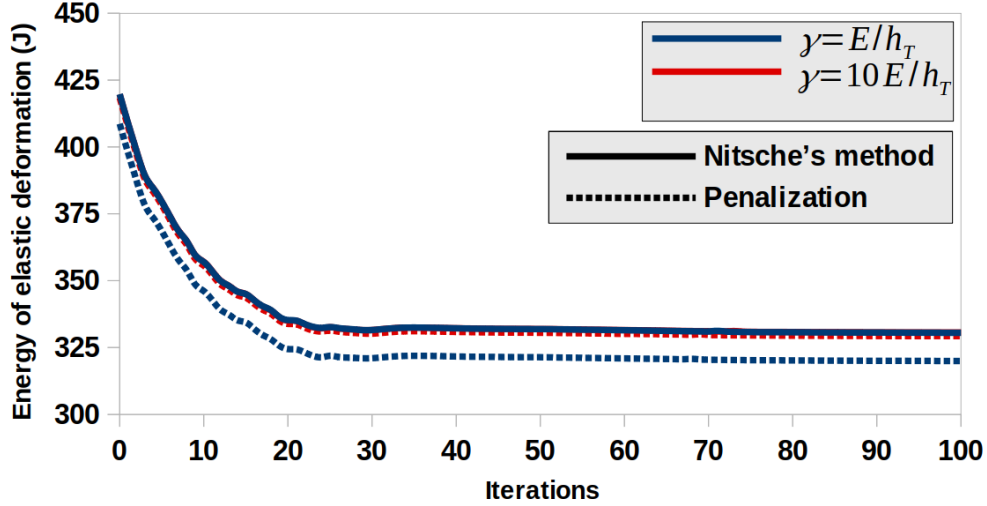
Figure 1.16: Evolution of the strain energy J_e during the shape optimization: comparison between Nitsche's method and penalization and different values of the parameter γ.

The main conclusion that can be drawn by considering the result presented in Figure 1.16 is that the use of the penalty method leads to a shape optimization more sensitive to the parameter γ than Nitsche's method whose results are quite independent on γ. The consideration of Nitsche's method thus allows the use of a parameter γ with a smaller value without deteriorating the quality of the solution. It also allows to avoid some potential difficulties which can be encountered when γ is large and which can result in a stiff problem difficult to solve numerically. As a consequence of this comparison, for the rest of our numerical study, we use Nitsche's method with a parameter $\gamma = E/h_T$.

1.5.4 Frictional contact and pressurized holes analysis

In this section, we perform two different shape optimizations with the Nitsche-based approach. We first set pressure into the holes with $g_N = -p^{hl}n$ where $p^{hl} = 3$ bar. In a second time, we perform a shape optimization taking into account a frictional contact (see section 1.2.1) with $\mathcal{F} = 1$.
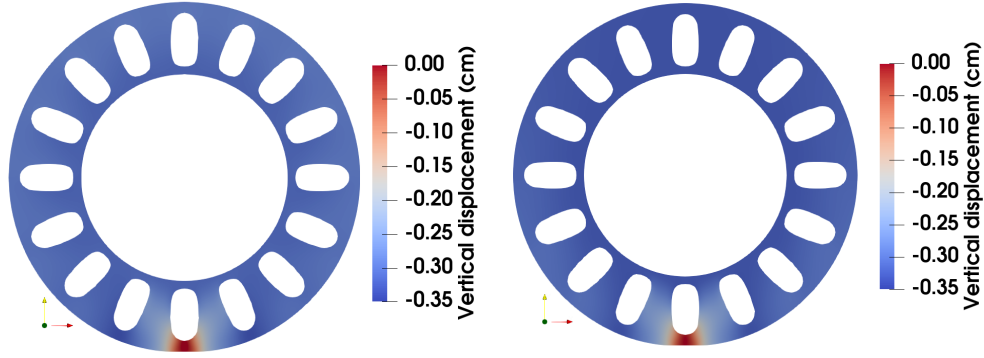
Figure 1.17: Optimal shapes. On the left: Shape optimization with pressure into the holes ($p^{hl} = 3$ bar) and on the right: Shape optimization with friction ($\mathcal{F} = 1$).

The two physical phenomena show very limited impacts on the optimal shapes in Figure 1.17 compared to Figure 1.11. Both pressure into the holes and frictional contact lead to a very similar optimal shape as the frictionless contact without pressure into the holes. That conclusion holds at least in the framework of linearized elasticity where small deformations occur and when only a vertical load is applied. Therefore we lead the next optimization tests without friction and without pressure into the holes.

1.5.5   Comparison of contact criterion strategies

A comparison is led between the contact stress criterion strategies described earlier. We recall that to uniformize the contact stress between the successive load positions, two strategies were presented in the previous parts: either the contact boundary is thickened with a size ϵ which leads to the criterion $J_{p,1}$ given by (1.27), or we consider the norm $H^{-1/2}(\Gamma_C, \mathbb{R}^d)$ of the criterion $J_{p,2}$ given by (1.28). We also recall that the general criterion set in the optimization algorithm reads as in (1.5). Here, the characteristic length L is chosen to be equal to ϵ. To perform a comparison between the two strategies $J_{p,1}$ and $J_{p,2}$, the parameter α is chosen to reach the same criterion amplitude at the first iteration of the optimization on both contact criterion strategies, i.e.

$$\sum_{i=1}^{N_d} \alpha_1 J_{p,1}(\Omega^0, u^i_{\Omega^0}, p_{mean}) = \sum_{i=1}^{N_d} \alpha_2 J_{p,2}(\Omega^0, u^i_{\Omega^0}, p_{mean}).$$

To this aim, we take in our case a weight $\alpha_1 = 6$ for the criterion $J_{p,1}(\Omega, u^i, p_{mean})$ and a weight $\alpha_2 = 100$ for $J_{p,2}(\Omega, u^i, p_{mean})$. In order to measure the effect of the uniformization criteria, Figure 1.18 first gives the optimal shape and the contact stress curves on the different positions without using these criteria (i.e. with $\alpha = 0$). One can see a significant disparity of contact stresses on the different loading positions which obviously corresponds to the presence or not of a hole near the effective contact area.
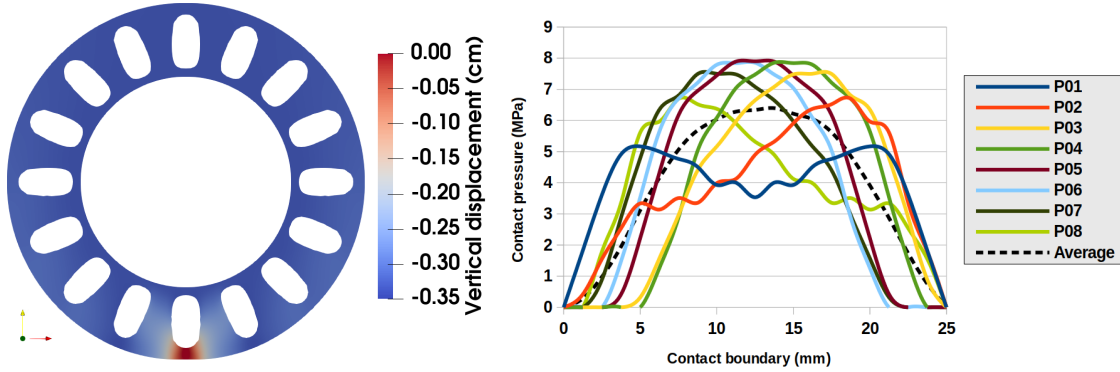
Figure 1.18: Optimization with J_e ($\alpha = 0$). Contact treated by Nitsche's method. On the left: optimal shape and on the right: contact stresses on the 8 load positions.
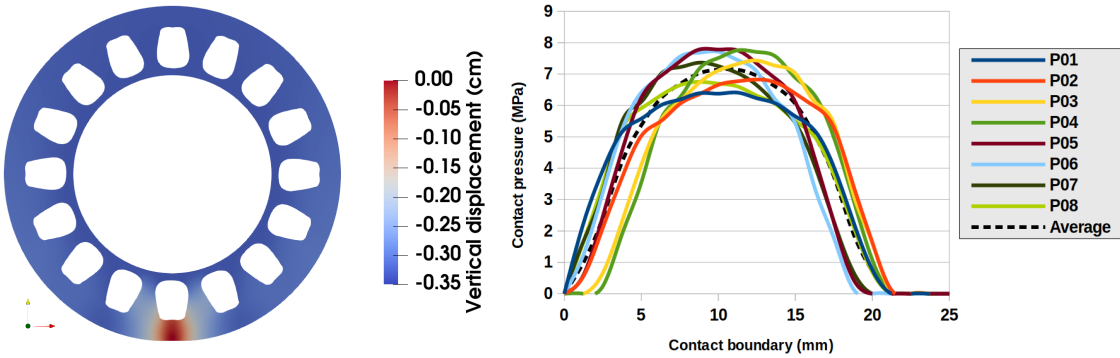
Figure 1.19: Optimization with J_e and $J_{p,1}$ ($\alpha_1 = 6$). Contact treated by Nitsche's method. On the left: optimal shape and on the right: contact stress on the 8 load positions.
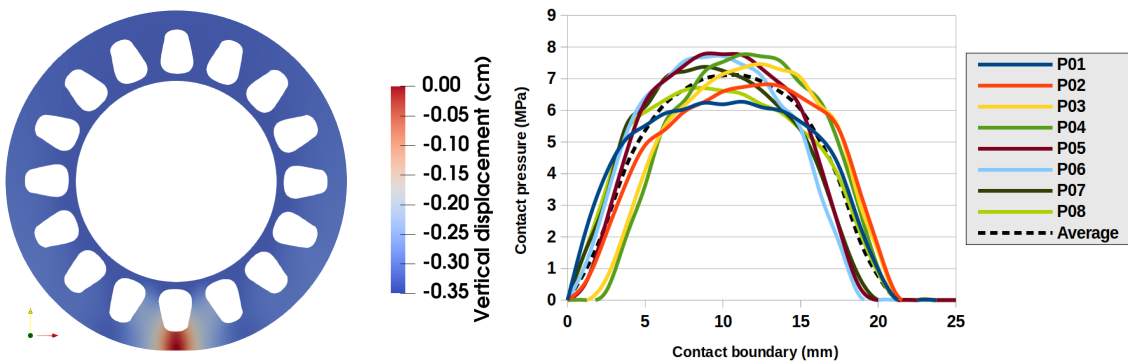
Figure 1.20: Optimization with J_e and $J_{p,2}$ ($\alpha_2 = 100$). Contact treated by Nitsche's method. On the left: optimal shape and on the right: contact stresses on the 8 load positions.

The effect of the addition of the uniformization criteria can be seen in Figures 1.19 and 1.20 for $J_{p,1}$ and $J_{p,2}$, respectively. Both criteria give some similar results, in particular the disparities on contact stresses have been significantly reduced compared to Figure 1.18 when only the strain energy is minimized. One of the effects of both criteria is a certain radial transfer of the holes away from the contact boundary resulting in some thickening of the ring of material located between the contact boundary Γ_C and the holes. It is quite obvious that this transfer contributes to the desired uniformization. One also notes a slight difference between the shapes obtained with $J_{p,1}$ and $J_{p,2}$, the thickening being a little more important for $J_{p,1}$ and ending with a smaller amount of material between the holes. There is also a difference in the decrease of the two criteria that is presented in Figure 1.21. $J_{p,2}$ leads to a proportionally larger decrease which shows that $J_{p,2}$ is actually a few more efficient than $J_{p,1}$. In addition, one advantage of the criterion $J_{p,2}$ over $J_{p,1}$ is that it does not depend on the parameter ϵ. And so, the calculation with $J_{p,2}$ does not require a non-optimizable zone of thickness ϵ which is more natural than the calculation with $J_{p,1}$.
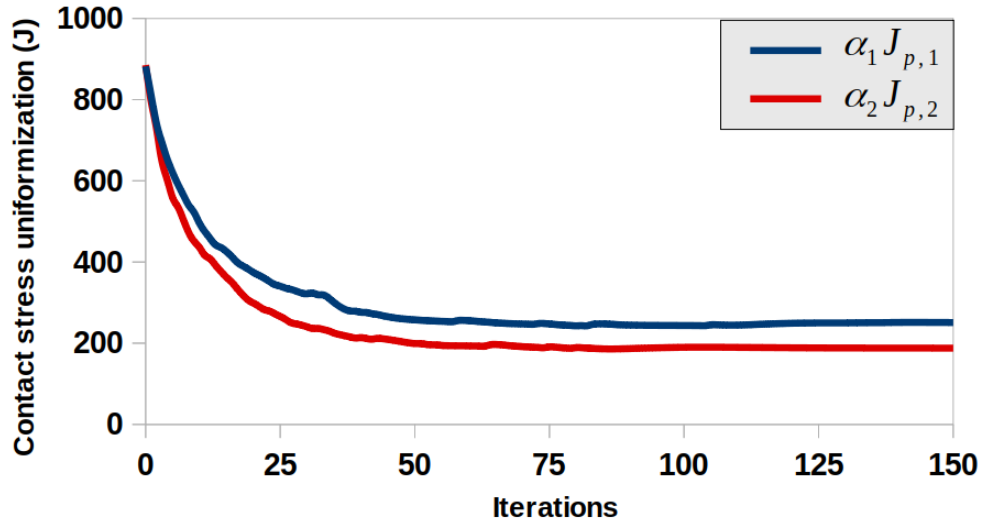
Figure 1.21: Comparison between the contact criterion strategies $J_{p,1}$ and $J_{p,2}$. Evolution of the contact stress uniformization criteria $J_{p,1}$ and $J_{p,2}$ for the configurations presented in Figures 1.19 and 1.20.

What's more, the magnitude of parameter α_2 influences the optimization and the minimization of J_e and $J_{p,2}$. One notes that $\alpha_2 = 10$ leads to a light optimization of $J_{p,2}$ as shown in Figure 1.22 whereas $\alpha_2 = 1000$ leads to a good uniformization of the contact stress even though the deflection of the structure increases (see Figure 1.23). And so J_e is less minimized. A wise choice of $\alpha_2 = 100$ is a good compromise to minimize both J_e and $J_{p,2}$ for this configuration (see Figure 1.20).
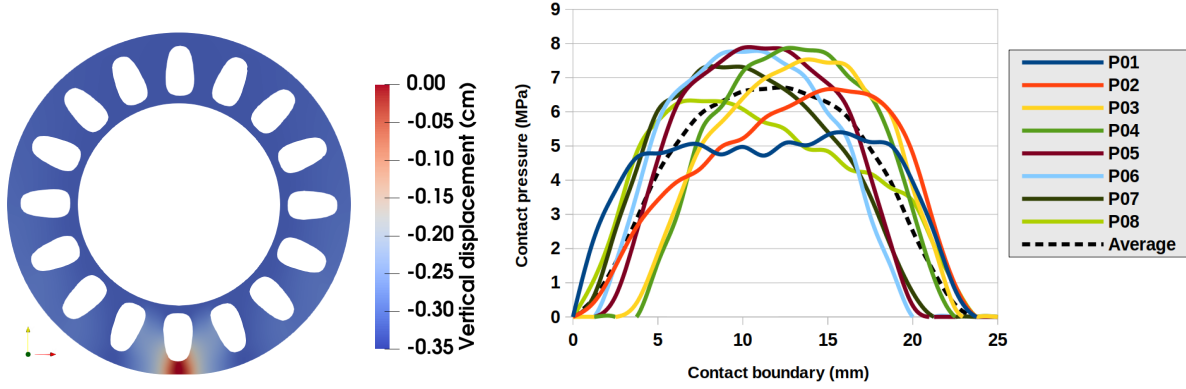
Figure 1.22: Optimization with J_e and $J_{p,2}$ ($\alpha_2 = 10$). Contact treated by Nitsche's method. On the left: optimal shape and on the right: contact stresses on the 8 load positions.
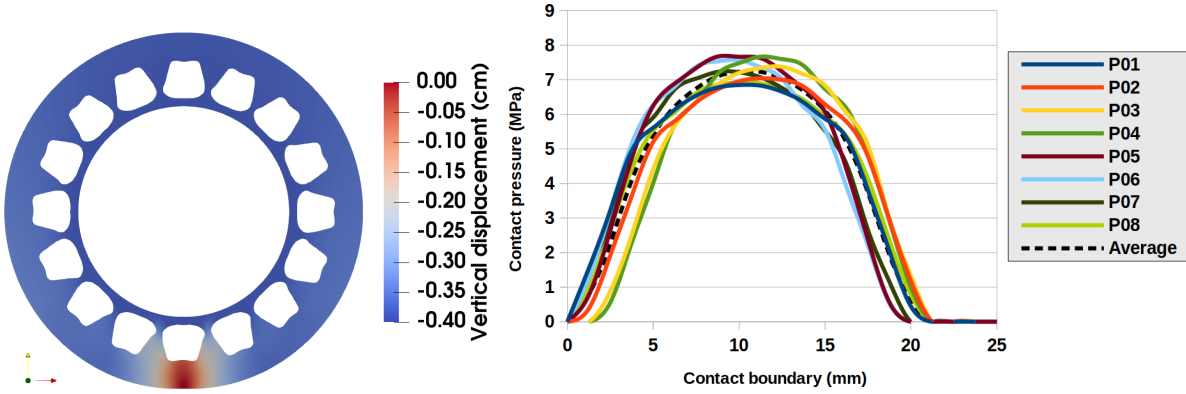
Figure 1.23: Optimization with J_e and $J_{p,2}$ ($\alpha_2 = 1000$). Contact treated by Nitsche's method. On the left: optimal shape and on the right: contact stresses on the 8 load positions.

1.5.6   Shape optimization of complex geometries

It is obvious that the final geometry obtained by shape optimization depends on the chosen initial geometry. This is especially the case since we have chosen to constrain the amount of material to remain constant. To illustrate the variety of shapes that can be obtained, optimization results are presented in Figure 1.24 with or without the use of an uniformization criterion of the contact stress and for an initial geometry with 48 holes. Finally, we present a case with an initial geometry with 108 holes optimized for the sole strain energy in two-dimensional in Figure 1.25 and three-dimensional in Figure 1.26.
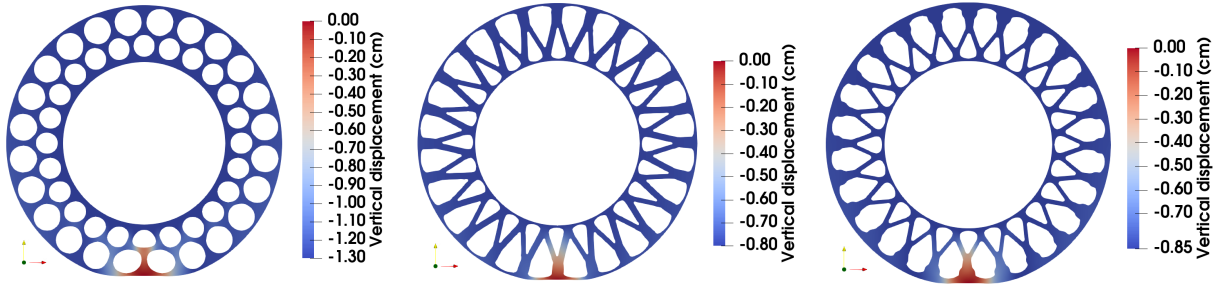
Figure 1.24: Optimal designs for 48 initial holes. From left to right: initial geometry with 48 circular holes, optimization with the J_e energy criterion and a multi-criterion optimization with J_e and $J_{p,2}$ with $\alpha = 50$.
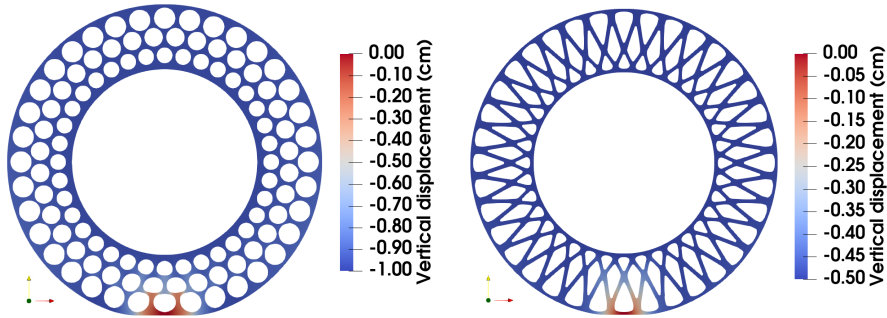
Figure 1.25: Optimal designs for 108 initial holes with the minimization of the J_e energy criterion in a two-dimensional framework. On the left: initial geometry and on the right an optimal shape.
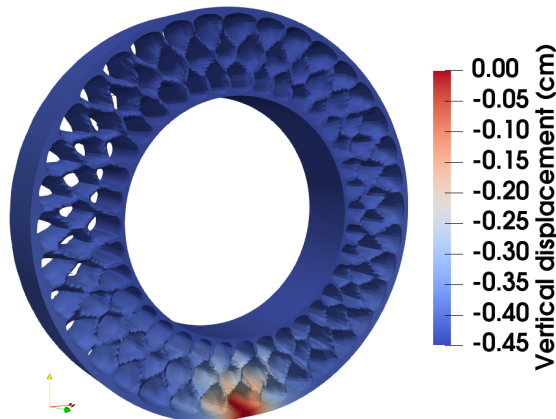
Figure 1.26: Optimal design for 108 initial holes with the minimization of the J_e energy criterion in a three-dimensional framework.

1.6   Conclusion

In this first chapter, we have presented a procedure for the shape optimization of a linearly elastic rolling structure in contact with a flat ground.

The main ingredients was Nitsche's method for the contact approximation, the use of cut finite elements, a level set representation of the geometry approximated on a regular polar grid. More precisely, the cut finite element method was used on the regular grid for the approximation of the displacement fields and the adjoint variables. Indeed, thanks to its optimal convergence, it allows the use of a coarser grid than for other fictitious domain methods. Finally, the ghost penalty stabilisation allows us to obtain a good quality gradient on the boundary of the evolving domain.

Beyond these choices, we have presented comparisons of the treatment of the contact condition by penalty and by Nitsche's method. In particular, these numerical experiments highlight the advantage of Nitsche's method which allows a consistent approximation of the contact condition without the use of Lagrange multipliers. We have also introduced two variants of a criterion for the uniformization of the contact stress for which the associated adjoint state is well defined and has a continuous dependence on the data. Eventually, the numerical experiments using each of these two criteria show very similar optimal elastic structures.

In this first part, we focused on the discrete case, assuming not to follow a mathematical care of the shape differentiability concerning the displacement and adjoint state variables, so that the shape gradient makes sense. In the next chapter, we pay a special attention on the mathematical formulation of the shape gradient, analysing the shape sensitivity.

Chapter 2

Shape sensitivity analysis

Contents

2.1 Introduction

In many industrial applications, shape optimization has become an essential tool to improve the quality of mechanical properties of workpieces. In some contexts, complexity arises

while the mathematical formulations involve non-linear or non-differentiable terms. In this study, the motivation is based on the shape optimization of an elastic structure in sliding contact via a gradient descent method. This requires in particular the shape derivative of the optimization criterion. Unfortunately, the introduction of a non-linear contact condition in the mechanical problem leads to a tricky formulation of the shape gradient. The elastic problem with sliding contact becomes an elliptic variational inequality whose differentiation is difficult to obtain especially since it is not well defined in the classical sense.

A first approach consists in defining a weak notion of the differentiability, the so-called conical differentiability initially introduced by F. Mignot in [70], leading to optimality conditions. We refer to the work of J. Sokolowski and J.-P. Zolesio [95, 97, 96, 99, 94, 98]. A way to get optimality conditions is to expose a sequence of penalized problems (see for instance [12, 10, 106] and for numerical applications see [81, 63, 30]). The case of an elastic structure with a contact condition has been considered by B. Chaudet and J. Deteix who proves differentiability of the solution to the contact problem using the penalization method in [19] and the augmented Lagrangian method in [20].

A second approach to deal with the non-differentiability in the classical sense consists in formulating the discrete variational inequality and then differentiating the discrete formulation thanks to subdifferential calculus. We refer to the work of J. Haslinger et al. [50, 43, 45, 51, 47, 46, 48] where the mechanical problem is approximated by the finite element method. In that work, Lipschitz regularity on the boundary is assumed to ensure the existence of an optimum. In particular, a convergence analysis is performed in [49] according to the discretization parameter.

Another way to reach optimal conditions is to regularize the unilateral contact conditions using smooth formulations as in [100, 101]. While friction is considered in the contact conditions, the derivation is even more tricky. The Tresca model for friction is studied in [97] and a conical derivative is reached for specific directions and only in a two-dimensional framework. Of course, penalized or regularized formulations ease the compute of shape derivatives as in [62, 64, 10, 102]. Results are given for Coulomb friction in [43]. In [58] a general overview of shape optimization results for problems with contact is proposed.

In the previous chapter, we were interested in the optimization of an elastic structure under contact conditions while trying to minimize criteria that couple compliance terms and additional terms allowing pressure uniformizations. We proposed the use of Nitsche-based methods [25] to efficiently discretize the contact terms. The optimization of the elastic structure is also performed using gradient descent method where the gradient is estimated via the adjoint state method applied directly on the discrete formulation of the problem. Although the proposed method allows us to obtain convincing structure optimization, no results of convergence analysis about the discretization of the adjoint state problem were given.The objective of this chapter is therefore to analyze and propose a development in this direction.

We recall that the weak formulation of Problem (1.1) in case of frictionless contact reads as

a variational inequality (see [36, 32, 61, 44]):

$$\begin{cases} \text{Find } u_\Omega \in K \text{ such that} \\ a(u_\Omega, v - u_\Omega) \geq \ell(v - u_\Omega), \quad \forall v \in K. \end{cases} \tag{2.1}$$

Moreover, the solution to (2.1) is the unique minimizer on K of the functional

$$\inf_{v \in K} \varphi(v) := \inf_{u \in K} \frac{1}{2} a(u, u) - \ell(u).$$

Contact conditions are often approximated in numerical application using the penalty method, which has the advantage of simplicity and robustness at the price of a supplementary approximation. Another classical strategy is the use of Lagrangian or augmented Lagrangian formulations which are fully consistent in contrary to the penalty approach but requires supplementary unknowns (the Lagrange multipliers) and the satisfaction of inf-sup conditions. In this work, we consider a third approach, namely Nitsche's method, which is also fully consistent and avoids the use of supplementary unknowns. In this chapter and for the sake of simplicity, we focus on a frictionless contact condition.

First of all, in section 2.2, we give some results about the conical directional differentiability of the solution to the contact problem and the link with the shape gradient mainly following [20, 68]. In a second step, as in the previous chapter, we present in section 2.3 the discretization of the adjoint state problem consisting in applying the adjoint state method on the discrete Nitsche version of the direct problem. Unfortunately, we note a lack of consistency of this approach. We then consider alternatively the discrete Nitsche-based approximation of the continuous adjoint state. We then show an a priori convergence result of this numerical discretization under assumptions of convergence rate of the discrete contact area. We will also see how to do without these assumptions by slightly modifying the Nitsche-based formulation of the adjoint state. Finally, numerical experiments will illustrate in section 2.4 these convergence results on the discretization of the adjoint state.

2.2   Shape optimization

The geometric shape optimization aims at minimizing a criterion $J(\Omega) = J(\Omega, u(\Omega))$. It explicitly depends on the domain Ω, but also implicitly on the solution u_Ω to Problem (2.1). For each part of the boundary Γ_C, Γ_D and Γ_N, it is supposed that a part is non-optimizable, denoted $\Gamma_C^{no}, \Gamma_D^{no}$ and Γ_N^{no}, the remaining parts Γ_C^o, Γ_D^o and Γ_N^o being optimizable. To preserve the coercivity of the problem, it is supposed that Γ_D^{no} is of non-zero Lebesgue measure. Let $\mathcal{D} \subset \mathbb{R}^d$ be a fixed bounded and smooth domain having $\Gamma_C^{no}, \Gamma_D^{no}$ and Γ_N^{no} as part of its boundary. The shape optimization consists in minimizing the criterion $J(\Omega)$ on the set of admissible domains composed of all smooth (of class $\mathscr{C}^1$) open domains $\Omega \subset \mathcal{D}$ accompagned with a partition Γ_C, Γ_D and Γ_N of its boundary with the constraint $\Gamma_C^{no} \subset \Gamma_C, \Gamma_D^{no} \subset \Gamma_D,$

and $\Gamma_N^{no} \subset \Gamma_N$ (see Figure 1.1). We recall the generic formulation for the target criterion (1.21) can be expressed as

$$J(\Omega) = \int_\Omega \mathcal{M}(u_\Omega) \, \mathrm{d}x + \int_{\partial\Omega} \mathcal{N}(u_\Omega) \, \mathrm{d}s(x), \qquad (2.2)$$

where $\mathcal{N}$ is defined on the boundary of Ω. In the following, we denote $\Gamma_m = \Gamma_C^o \cup \Gamma_D^o \cup \Gamma_N^o$ the optimizable (moving) boundary.

2.2.1   Notions of shape derivative

We recall here some results coming mainly from [20, 68]. In addition, we develop more precisely the previous section 1.3.1. The differentiation with respect to the domain aims at modifying the reference state of the domain Ω using the boundary method first described by J. Hadamard in [41] and then developed for instance in [74, 83, 93, 97, 55]. Let $\Theta \in W^{1,\infty}(\mathbb{R}^d; \mathbb{R}^d) \cap \mathscr{C}^1(\mathbb{R}^d)$ be a vector field displacing the reference domain Ω towards different admissible shapes Ω_t. The associated transported domain Ω_t in the direction Θ is defined as

$$\Omega_t = (Id + \Theta)(\Omega),$$

for Θ small enough so that $Id + \Theta$ is a diffeomorphism (see for instance [54]). Then the classical notion of differentiability in Banach spaces can define shape differentiability. We refer to [29] for the different notions of derivation. We recall the definition of a conical derivative as expressed in [70].

Definition 9. *Let V_1 and V_2 be two Banach spaces. A continuous function $u : V_1 \to V_2$ admits a conical derivative at x it there exists an operator $Q : V_1 \to V_2$ positively homogeneous such that:*

$$\forall h \in V_1, \forall t \geq 0, u(x + th) = u(x) + tQ(h) + o(t),$$

where o is to be understood as

$$\lim_{\Theta \to 0} \frac{\|o(\Theta)\|_V}{\|\Theta\|_{W^{1,\infty}(\mathbb{R}^d, \mathbb{R}^d)}} = 0.$$

For $u_\Omega \in V$ the solution of a variational formulation posed on Ω, there are two ways to define the derivative of u according to Ω as proposed for instance in [68]: a Lagrangian and an Eulerian one. First we define the Lagrangian derivative or material derivative following the point x during its transportation by the diffeomorphism $I_d + \Theta$.

Definition 10. *Let V be a reflexive Banach set and assume that $u_\Omega(x) \in V$, and $u_{(I_d+\Theta)\Omega}(x + \Theta(x)) \in V$. We call $d_\Omega u[\Theta]$, the directional Lagrangian derivative of $u_\Omega(x)$ in the direction Θ, the linear form in Θ from $W^{1,\infty}(\mathbb{R}^d, \mathbb{R}^d)$ to V satisfying:*

$$u_{(I_d+\Theta)\Omega}(x + \Theta) = u_\Omega(x) + d_\Omega u[\Theta] + o(\Theta).$$

where $o(\Theta)$ is to be understood as

$$\lim_{\Theta \to 0} \frac{\|o(\Theta)\|_V}{\|\Theta\|_{W^{1,\infty}(\mathbb{R}^d,\mathbb{R}^d)}} = 0.$$

The other definition refers to the Eulerian derivative or shape derivative which is more easy to use but causes additional difficulties to be properly defined. There is actually no difficulty if we define it for a point x belonging to both Ω and $(I_d + \Theta)(\Omega)$. Yet it is much more intricate for points located in the boundary $\partial\Omega$ which do not belong to $(I_d + \Theta)(\Omega)$ or its boundary. We only differentiate the point values of $u(x)$, without carrying the points on the boundary which does not lead to rigorous definitions of functional space for u and its derivative.

Definition 11. *We call $\mathcal{D}_\Omega u[\Theta]$, the directional Eulerian derivative of $u_\Omega(x)$, the linear form in Θ that satisfies:*

$$u_{(I_d+\Theta)\Omega}(x) = u_\Omega(x) + \mathcal{D}_\Omega u[\Theta] + o(\Theta).$$

Note that while the additional condition $\nabla u_\Omega \cdot \Theta \in V$ holds for $\Theta \in W^{1,\infty}(\mathbb{R}^d;\mathbb{R}^d) \cap \mathscr{C}^1(\mathbb{R}^d)$, we use the following notation of the directional Eulerian or shape derivative of an element u according to Ω in the direction Θ:

$$\mathcal{D}_\Omega u[\Theta] = d_\Omega u[\Theta] - \nabla u_\Omega \cdot \Theta. \tag{2.3}$$

The relation (2.3) correctly defines the Eulerian derivative, preventing from the difficulties previously mentioned. Finally, we note that the solution u_Ω is directionally shape differentiable if it admits a directional derivative for any admissible direction Θ. In case the map $\Theta \mapsto \mathcal{D}_\Omega u_\Omega[\Theta]$ is positively homogeneous from $\mathscr{C}^1(\mathbb{R}^d)$ to V, u_Ω is conically differentiable. Finally, this map is shape differentiable if it is linear continuous from $\mathscr{C}^1(\mathbb{R}^d)$ to V.

2.2.2 Shape differentiability

It is known that the projection operator used in the contact condition is not Fréchet-differentiable, the consequence being that u_Ω is not differentiable in a classical sense. However, it has been proved that the solution u_Ω of (2.1) admits conical material and shape derivatives in some directions Θ. We actually know from [70] that projection operators are conically differentiable. It has been proved in [96] that Signorini's problem admits a conical material and shape derivative.

We make the same usual choice as [20] to restrict the directions of Θ. In view of Zolésio-Hadamard structure theorem, we limit the geometric deformation fields $\Theta \in \mathscr{C}^1(\mathbb{R}^d)$ along the direction of the normal n. The vector n is extended to $\mathscr{C}^1(\mathbb{R}^d)$ as $\partial\Omega$ is assumed to have $\mathscr{C}^1$ regularity. To achieve the transport of the domain, the variables need to respect some regularity for usual differentiability conveniences.

Assumption 12. $(\lambda, \mu) \in \left(\mathscr{C}^1(\mathbb{R}^d)\right)^2$, $f \in H^1(\Omega; \mathbb{R}^d)$ and $g \in H^2(\Omega; \mathbb{R}^d)$.

We suppose also as in [20, 19] that for $u_\Omega \in H^{(\frac{3}{2}+\nu)}(\Omega)$ with $\nu \in]0, 1[$. This implies in particular $\sigma_n(u_\Omega) \in L^2(\Gamma_C)$. The contact boundary Γ_C is split into three parts as illustrated in Figure 2.1 (with $\sigma_n(u_\Omega)$ a particular representative of its class in $L^2(\Gamma_C)$):

- $\Gamma_{C,a} := \{x \in \Gamma_C | \sigma_n(u_\Omega) < 0, (u_\Omega)_n = g\}$, the active set, or effective contact area,

- $\Gamma_{C,i} := \{x \in \Gamma_C | \sigma_n(u_\Omega) = 0, (u_\Omega)_n < g\}$, the inactive set, or non-contact area,

- $\Gamma_{C,b} := \{x \in \Gamma_C | \sigma_n(u_\Omega) = 0, (u_\Omega)_n = g\}$, the bi-active set, or grazing contact area.
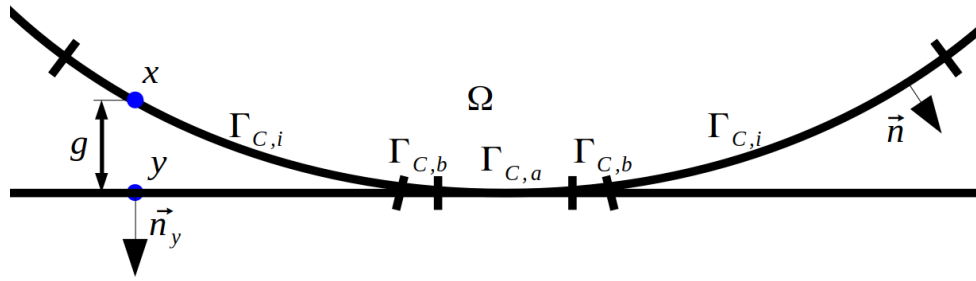
Figure 2.1: Contact area split into three parts.

Theorem 13. *Under Assumption 12, the solution u_Ω of (2.1) is conically shape differentiable with respect to the domain Ω and its conical shape derivative $\mathcal{D}_\Omega u[\Theta]$ in the direction Θ satisfies $\mathcal{D}_\Omega u[\Theta] \in S(K_0)$ and*

$$a(\mathcal{D}_\Omega u[\Theta], \phi - \mathcal{D}_\Omega u[\Theta]) \geq \ell'(\phi - \mathcal{D}_\Omega u[\Theta])[\Theta] - a'(u_\Omega, \phi - \mathcal{D}_\Omega u[\Theta])[\Theta], \quad \forall \phi \in S(K_0), \quad (2.4)$$

where $S(K_0) = \{\phi \in V | \phi_n \leq 0$ a.e. on $\Gamma_{C,a} \cup \Gamma_{C,b}$ and $(a(u_\Omega, \phi) = \ell(\phi))\}$ and where

$$a'(u, v)[\Theta] = \int_{\Gamma_m} (\Theta \cdot n) \, A\varepsilon(u) : \varepsilon(v) \, \mathrm{d}s(x),$$

$$\ell'(v)[\Theta] = \int_{\Gamma_m} (\Theta \cdot n) \, f \cdot v \, \mathrm{d}s(x) + \int_{\Gamma_m \cap \Gamma_N} (\Theta \cdot n) \, (\kappa_m g_N \cdot v + \nabla(g_N \cdot v) \cdot n) \, \mathrm{d}s(x).$$

Here Γ_m is still the optimizable boundary of Ω and κ_m is the mean curvature of $\partial\Omega$.

The proof can be found in [68], Section 5.2. Note that Formulation (2.4) relies on the set $S(K_0)$ that is not easy to handle. It is however possible to rewrite this formulation as a standard optimization problem under the assumption that there exists no isolated point (see [59]):

Assumption 14. $\Gamma_{C,a} \cup \Gamma_{C,b} = \overline{\mathrm{int}(\Gamma_{C,a} \cup \Gamma_{C,b})}$.

Theorem 15. *Under assumptions 12 and 14, $\mathcal{D}_\Omega u[\Theta]$ is solution of (2.4) if and only if it solves:*

$$\inf_{\phi \in K_{\Gamma_{C,a}}} \frac{1}{2} a(\phi, \phi) - \ell'(\phi)[\Theta] + a'(u_\Omega, \phi)[\Theta],$$

where $V_{\Gamma_{C,a}} := \{\phi \in V \,|\, \phi_n = 0 \ a.e. \ on \ \Gamma_{C,a}, \phi = 0 \ a.e. \ on \ \Gamma_D\}$ and $K_{\Gamma_{C,a}} := \{\phi \in V_{\Gamma_{C,a}} \,|\, \phi_n \leq 0 \ a.e. \ on \ \Gamma_{C,b}\}$.

The proof can be found in [20] and shows in particular that $S(K_0) = K_{\Gamma_{C,a}}$. Some additional results can then be obtained in the case $K_{\Gamma_{C,a}} = V_{\Gamma_{C,a}}$, which implies the use of the following assumption:

Assumption 16. *The subset $\Gamma_{C,b}$ is of zero Lebesgue measure in Γ_C.*

The non-differentiability coming from the points in $\Gamma_{C,b}$, the analysis can be simplified when the assumption 16 is considered.

Remark 17. *An element $x \in \Gamma_{C,b}$ is a point where $(u_\Omega)_n = g$ and $\sigma_n(u_\Omega) = 0$ at the same time which means that contact occurs with a vanishing contact pressure. The set $\Gamma_{C,b}$ is often referred as the set of grazing contact. Assumption 16 is verified while the set of grazing contact points is a zero measure set between contact and non contact areas. Interestingly, this corresponds, in fact, to most of the practical situations.*

Theorem 18. *Under assumptions 12 and 14 and if in addition Assumption 16 holds, then u_Ω solution of (2.1) is shape differentiable in $L^2(\Omega)$. Its shape derivative in the direction Θ denoted $\mathcal{D}_\Omega u[\Theta]$ is defined as the unique solution of*

$$a(\mathcal{D}_\Omega u[\Theta], \phi) = \ell'(\phi)[\Theta] - a'(u_\Omega, \phi)[\Theta], \ \forall \phi \in V_{\Gamma_{C,a}}. \tag{2.5}$$

The proof can be found in [69] Section 1.3.3.

2.2.3 Shape gradient formulation

Still considering the generic formulation for a criterion in (2.2) given by

$$J(\Omega) = \int_\Omega \mathcal{M}(u_\Omega) \, \mathrm{d}x + \int_{\partial\Omega} \mathcal{N}(u_\Omega) \, \mathrm{d}s(x),$$

we assume that the two functions $\mathcal{M}$ and $\mathcal{N}$ are in $\mathscr{C}^1(\mathbb{R}^d)$ and their derivatives $\mathcal{M}'$ and $\mathcal{N}'$ are Lipschitz-continuous. Suppose Ω is of class $\mathscr{C}^2$ and Assumption 12 holds, then $J(\Omega)$ is also conically shape differentiable at Ω and its derivative in the direction $\Theta \in W^{1,\infty}(\mathbb{R}^d; \mathbb{R}^d)$ reads (see [68]):

$$\begin{aligned}
\mathcal{D} J(\Omega)[\Theta] &= \int_\Omega \left(\mathcal{M}'(u_\Omega) \cdot \mathcal{D}_\Omega u[\Theta] + (\Theta \cdot n) \mathcal{M}(u_\Omega) \right) \mathrm{d}x \\
&+ \int_{\partial\Omega} \left(\mathcal{N}'(u_\Omega) \cdot \mathcal{D}_\Omega u[\Theta] + (\Theta \cdot n) \left(\kappa_m \, \mathcal{N}(u_\Omega) + \nabla\mathcal{N}(u_\Omega) \cdot n \right) \right) \mathrm{d}s(x).
\end{aligned} \tag{2.6}$$

From a numerical point of view, this expression of the shape derivative is difficult to use in the sense that it does not allow to define a gradient algorithm. Therefore, in order to isolate a quantity independent of Θ and get rid of the Eulerian derivative, we classically introduce the adjoint state variable $p_\Omega \in V_{\Gamma_{C,a}}$ solution to the following problem:

$$a(v, p_\Omega) = -\int_\Omega \mathcal{M}'(u_\Omega) \cdot v \, \mathrm{d}x - \int_{\partial\Omega} \mathcal{N}'(u_\Omega) \cdot v \, \mathrm{d}s(x), \ \forall v \in V_{\Gamma_{C,a}}. \tag{2.7}$$

The corresponding strong formulation is the following:

$$\begin{cases} -\mathrm{div}\,(\sigma(p_\Omega)) = -\mathcal{M}'(u_\Omega) & \text{in } \Omega, \\ \sigma(p_\Omega)n \ = -\mathcal{N}'(u_\Omega) & \text{on } \Gamma_{C,b} \cup \Gamma_{C,i} \cup \Gamma_N, \\ p_\Omega \ = 0 & \text{on } \Gamma_D, \\ (p_\Omega)_n \ = 0 & \text{on } \Gamma_{C,a}, \\ \sigma_t(p_\Omega) \ = -(\mathcal{N}'(u_\Omega))_t & \text{on } \Gamma_{C,a}. \end{cases} \tag{2.8}$$

This allows to rewrite the shape derivative of J in (2.6) for $v = \mathcal{D}_\Omega u$ as

$$\begin{aligned} \mathcal{D} J(\Omega)[\Theta] \ &= -a(\mathcal{D}_\Omega u[\Theta], p_\Omega) \\ &\quad + \int_\Omega (\Theta \cdot n)\mathcal{M}(u_\Omega) \, \mathrm{d}x + \int_{\partial\Omega} (\Theta \cdot n)\,(\kappa_m\,\mathcal{N}(u_\Omega) + \nabla\mathcal{N}(u_\Omega) \cdot n)\,\mathrm{d}s(x). \end{aligned}$$

Considering Assumption 16 and taking $\phi = p_\Omega$ in (2.5), it holds

$$\begin{aligned} \mathcal{D} J(\Omega)[\Theta] \ &= \int_{\Gamma_m} (\Theta \cdot n)\,(\mathcal{M}(u_\Omega) + A\varepsilon(u_\Omega) : \varepsilon(p_\Omega) - f(x) \cdot p_\Omega)\,\mathrm{d}s(x) \\ &\quad + \int_{\Gamma_m} (\Theta \cdot n)\,(\kappa_m\,\mathcal{N}(u_\Omega) + \nabla\mathcal{N}(u_\Omega) \cdot n)\,\mathrm{d}s(x) \\ &\quad - \int_{\Gamma_m \cap \Gamma_N} (\Theta \cdot n)\,(\kappa_m\,p_\Omega \cdot g_N + \nabla(p_\Omega \cdot g_N) \cdot n)\,\mathrm{d}s(x). \end{aligned} \tag{2.9}$$

In particular, this formula now allows us to easily obtain the gradient expression of J from

$$\mathcal{D} J(\Omega)[\Theta] = \langle \nabla J(\Omega), \Theta \rangle_{L^2(\Gamma_m)} = \int_{\Gamma_m} \nabla J(\Omega)(x) \cdot \Theta(x)\,\mathrm{d}s(x),$$

which is defined for all $x \in \Gamma_m$ by

$$\begin{aligned} \nabla J(\Omega)(x) &= (\mathcal{M}(u_\Omega(x)) + A\varepsilon(u_\Omega(x)) : \varepsilon(p_\Omega(x)) - f(x) \cdot p_\Omega(x))n(x) \\ &\quad + (\kappa_m(x)\,\mathcal{N}(u_\Omega(x)) + \nabla\mathcal{N}(u_\Omega(x)) \cdot n(x))n(x) \\ &\quad + (\kappa_m(x)\,p_\Omega \cdot g_N(x) + \nabla(p_\Omega(x) \cdot g_N(x)) \cdot n(x))\chi_{\Gamma_N}(x)n(x). \end{aligned} \tag{2.10}$$

Note that since $a(\cdot, \cdot)$ is a continuous and coercive bilinear form whereas $\mathcal{M}$ and $\mathcal{N}$ are supposed to be Lipschitz-continuous, Lax-Milgram theorem ensures the well-posedness of problem (2.7) which admits a unique solution $p_\Omega \in V_{\Gamma_{C,a}}$.

Remark 19. *If assumption 16 does not hold, is is not possible to obtain the formulation (2.9) since the shape derivative depends nonlinearly on the direction Θ. In this case, the functional J is not differentiable in the classical sense.*

2.3 Nitsche-based formulations

In this section, we conduct a convergence analysis of a finite element approximation of the adjoint state equation (2.7). We introduce Nitsche's method to deal with the boundary condition on Γ_C. We verify its the consistency and finally detail its convergence analysis.

2.3.1 Nitsche-based formulation for the direct problem

We recall that the generalized Nitsche-based approximation $u_\Omega^h \in V^h$ (where V^h is proposed in equation 1.20) is defined as the solution of

$$a(u_\Omega^h, v^h) + \mathcal{I}(u_\Omega^h, v^h, n) = \ell(v^h), \quad \forall v^h \in V^h, \tag{2.11}$$

where the frictionless contact term $\mathcal{I}(u, v, n)$ reads

$$\mathcal{I}(u,v,n) = -\int_{\Gamma_C} \frac{\theta}{\gamma} \sigma_n(u)\sigma_n(v)\, \mathrm{d}s(x) + \int_{\Gamma_C} \frac{1}{\gamma}\, [\sigma_n(u) - \gamma(u_n - g)]_-\, (\theta\, \sigma_n(v) - \gamma v_n)\, \mathrm{d}s(x).$$

We recall some results from the work of P. Hild, F. Chouly and Y. Renard in [25] in the following result.

Proposition 20. *Suppose that the solution u to Problem (2.1) belongs to $(H^{\frac{3}{2}+\nu}(\Omega))^d$ with $\nu \in\,]0, k - 1/2[$ ($k = 1, 2$ is the degree of the finite element method given in (1.20))and $d = 2, 3$. When $\theta \neq -1$, suppose in addition that the parameter γ_0 is sufficiently large. The solution u_Ω^h of Problem (2.11) satisfies the following error estimates for $C > 0$ a constant independent of h:*

$$\|u_\Omega^h - u_\Omega\|_{1,\Omega} \leq Ch^{\frac{1}{2}+\nu}\|u_\Omega\|_{\frac{3}{2}+\nu,\Omega}, \tag{2.12}$$

$$\|\sigma_n(u_\Omega^h) - \sigma_n(u_\Omega)\|_{0,\Gamma_C} \leq Ch^\nu \|u_\Omega\|_{\frac{3}{2}+\nu,\Omega},$$

$$\|[\sigma_n(u_\Omega^h) - \gamma((u_\Omega)_n^h - g)]_- + \sigma_n(u_\Omega)\|_{0,\Gamma_C} \leq Ch^\nu \|u_\Omega\|_{\frac{3}{2}+\nu,\Omega}. \tag{2.13}$$

Note that these convergence results make an important use of the following classical property whose proof can be found for instance in [25]:

Lemma 21. *There exists $C > 0$ independent of the parameter γ_0 and of the mesh size h, such that for all $v^h \in V^h$*

$$\|\gamma^{-\frac{1}{2}}\sigma_n(v^h)\|_{0,\Gamma_C}^2 \leq \frac{C}{\gamma_0}\|v^h\|_{1,\Omega}^2.$$

2.3.2   Adjoint state of the Nitsche-based formulation

For the minimization of the discrete criterion

$$J^h(\Omega) = \int_\Omega \mathcal{M}(u_\Omega^h) \, \mathrm{d}x + \int_{\partial\Omega} \mathcal{N}(u_\Omega^h) \, \mathrm{d}s(x),$$

where $u_\Omega^h \in V^h$ solution of (2.11), a first approach proposed in the first chapter is to derive the adjoint state of the discrete formulation, for instance using a Lagrangian approach. This leads to the following formulation:

$$
\begin{aligned}
\mathcal{D} \, J^h(\Omega)[\Theta] \; = \; & \int_{\Gamma_m} (\Theta \cdot n) \, (\mathcal{M}(u_\Omega^h) + A\varepsilon(u_\Omega^h) : \varepsilon(\tilde{p}_\Omega^h) - f(x) \cdot \tilde{p}_\Omega^h) \, \mathrm{d}s(x) \\
& + \int_{\Gamma_m} (\Theta \cdot n) \, (\kappa_m \, \mathcal{N}(u_\Omega^h) + \nabla\mathcal{N}(u_\Omega^h) \cdot n) \, \mathrm{d}s(x) \\
& - \int_{\Gamma_m \cap \Gamma_N} (\Theta \cdot n) \, (\kappa_m \, \tilde{p}_\Omega^h \cdot g_N + \nabla(\tilde{p}_\Omega^h \cdot g_N) \cdot n) \, \mathrm{d}s(x),
\end{aligned}
\tag{2.14}
$$

where the discrete adjoint state $\tilde{p}_\Omega^h \in V^h$ is defined by

$$
\begin{cases}
\text{Find } \tilde{p}_\Omega^h \in V^h \text{ such that } \forall q^h \in V^h \\[4pt]
a(\tilde{p}_\Omega^h, q^h) - \displaystyle\int_{\Gamma_C} \frac{\theta}{\gamma} \sigma_n(\tilde{p}_\Omega^h)\sigma_n(q^h) \mathrm{d}s(x) \\[10pt]
+ \displaystyle\int_{\Gamma_C} \frac{1}{\gamma} H(-(\sigma_n(u_\Omega^h) - \gamma((u_\Omega^h)_n - g))))(\sigma_n(q^h) - \gamma q_n^h)(\theta\sigma_n(\tilde{p}_\Omega^h) - \gamma(\tilde{p}_\Omega^h)_n)\mathrm{d}s(x) \\[10pt]
= - \displaystyle\int_\Omega \mathcal{M}'(u_\Omega^h) \cdot q^h \, \mathrm{d}x - \int_{\partial\Omega} \mathcal{N}'(u_\Omega^h) \cdot q^h \, \mathrm{d}s(x),
\end{cases}
\tag{2.15}
$$

with $H(x) = \begin{cases} 1 \text{ for } x > 0 \\ 0 \text{ for } x \leq 0 \end{cases}$ being the Heaviside function.

Since expressions (2.14) and (2.9) are more than similar and that there are some convergence results about the convergence of u_Ω^h to u_Ω, a question that naturally arises is to know if a similar convergence result of $\tilde{p}_\Omega^h$ towards p_Ω can be expected. Unfortunately the answer is no in the general case, due to a consistency issue in the definition of $\tilde{p}^h$ which does not allow to ensure the right boundary conditions on $\Gamma_{C,a}$, at least in the case $\theta \neq 1$. To be convinced of this, it is enough to notice that assuming for simplicity $H(-(\sigma_n(u_\Omega^h) - \gamma((u_\Omega^h)_n - g)))) = \chi_{\Gamma_{C,a}}$, then $\tilde{p}_\Omega^h$ satisfies after application of Green's formula and for simplicity, by example, for $\theta = 0$:

$$
\begin{aligned}
0 = & - \int_\Omega (\mathrm{div}\,(\sigma(\tilde{p}_\Omega^h)) - \mathcal{M}'(u_\Omega^h)) \cdot q^h dx + \int_{\Gamma_N \cup \Gamma_{C,b} \cup \Gamma_{C,i}} (\sigma(\tilde{p}_\Omega^h)n + \mathcal{N}'(u_\Omega^h)) \cdot q^h ds(x) \\
& + \int_{\Gamma_{C,a}} \left(\sigma(\tilde{p}_\Omega^h)n \cdot q^h + \gamma(\tilde{p}_\Omega^h)_n q_n^h - \sigma_n(q^h)(\tilde{p}_\Omega^h)_n + \mathcal{N}'(u_\Omega^h) \cdot q^h\right) ds(x),
\end{aligned}
$$

which enforces both $(\tilde{p}_\Omega^h)_n = 0$ and $\sigma(\tilde{p}_\Omega^h)n = -\mathcal{N}'(u_\Omega^h)$ asymptotically on $\Gamma_{C,a}$ when h goes to zero. This is symptomatic of the non-self-adjoint nature of Nitsche's method for $\theta \neq 1$.

Remark 22. *Although we cannot demonstrate a convergence result from the discrete adjoint state to its continuous counterpart, at least for $\theta \neq 1$, the use of $\tilde{p}_\Omega^h$ in (2.14) allows to properly define the gradient of the discrete energy J^h which can be use to minimize J^h using a gradient algorithm, as we proposed earlier in the previous chapter.*

2.3.3 Nitsche-based formulation for the adjoint state and consistency

A second approach is the discretization of Problem (2.8) with a Nitsche-based method. It can be formulated as follows

$$
\begin{cases}
\text{Find } p_\Omega^h \in V^h \text{ such that } \forall q^h \in V^h \\
a(p_\Omega^h, q^h) - \int_{\Gamma_C} \frac{\theta}{\gamma}(\sigma_n(p_\Omega^h) + (\mathcal{N}'(u_\Omega^h))_n)\sigma_n(q^h)\mathrm{d}s(x) \\
+ \int_{\Gamma_C} \frac{1}{\gamma}H(-(\sigma_n(u_\Omega^h) - \gamma(u_n^h - g))))(\sigma_n(p_\Omega^h) + (\mathcal{N}'(u_\Omega^h))_n - \gamma(p_\Omega^h)_n)(\theta\sigma_n(q^h) - \gamma q_n^h)\mathrm{d}s(x) \\
= -\int_\Omega \mathcal{M}'(u_\Omega^h) \cdot q^h \, \mathrm{d}x - \int_{\partial\Omega} \mathcal{N}'(u_\Omega^h) \cdot q^h \, \mathrm{d}s(x).
\end{cases}
$$

$$(2.16)$$

where $\theta \in \mathbb{R}$ and $\gamma > 0$. Note that expressions (2.16) and (2.15) are identical in the case $\theta = 1$ (this corresponds to the symmetric version of Nitsche's method) and when $\mathcal{N}'(u_\Omega^h)$ vanishes on Γ_C. The advantage of Formulation (2.16) over (2.15) is that a consistency result can be proved for (2.16)

Lemma 23. *The Nitsche-based adjoint state formulation* (2.16) *is consistent in the following sense: suppose that the solution p_Ω to* (2.8) *lies in $(H^{\frac{3}{2}+\nu}(\Omega))^d$ with $\nu \geq 0$ and $d = 2, 3$. Then if assumption 16 holds, p_Ω is also solution, $\forall q^h \in V^h$, of*

$$
a(q^h, p_\Omega) - \int_{\Gamma_C} \frac{\theta}{\gamma}(\sigma_n(p_\Omega) + (\mathcal{N}'(u_\Omega))_n)\sigma_n(q^h)\mathrm{d}s(x)
$$
$$
+ \int_{\Gamma_C} \frac{1}{\gamma}H(-(\sigma_n(u_\Omega) - \gamma((u_\Omega)_n - g))))((\sigma_n(p_\Omega) + (\mathcal{N}'(u_\Omega))_n) - \gamma(p_\Omega)_n)(\theta\sigma_n(q^h) - \gamma q_n^h)\mathrm{d}s(x)
$$
$$
= -\int_\Omega \mathcal{M}'(u_\Omega) \cdot q^h \, \mathrm{d}x - \int_{\partial\Omega} \mathcal{N}'(u_\Omega) \cdot q^h \, \mathrm{d}s(x).
$$

$$(2.17)$$

Proof. Using Green's formula on the adjoint state problem (2.8), $\forall q^h \in V^h$, it holds

$$
a(q^h, p_\Omega) - \int_{\partial\Omega} (\sigma(p_\Omega)n + \mathcal{N}'(u_\Omega)) \cdot q^h\mathrm{d}s(x) = -\int_\Omega \mathcal{M}'(u_\Omega) \cdot q^h \, \mathrm{d}x - \int_{\partial\Omega} \mathcal{N}'(u_\Omega) \cdot q^h \, \mathrm{d}s(x).
$$

As p_Ω satisfies $\sigma(p_\Omega)n = -\mathcal{N}'(u_\Omega)$ in $\Gamma_{C,i} \cup \Gamma_N$, we have

$$
\int_{\Gamma_{C,i}\cup\Gamma_N} (\sigma(p_\Omega)n + \mathcal{N}'(u_\Omega)) \cdot q^h\mathrm{d}s(x) = \int_{\Gamma_{C,i}} (\sigma_n(p_\Omega) + (\mathcal{N}'(u_\Omega))_n)\sigma_n(q^h)\mathrm{d}s(x) = 0.
$$

Recall also that p_Ω satisfies $(p_\Omega)_n = 0$ and $\sigma(p_\Omega)_t = -\mathcal{N}'(u_\Omega)_t$ in $\Gamma_{C,a}$, which gives

$$\int_{\Gamma_{C,a}} (\sigma(p_\Omega)n + \mathcal{N}'(u_\Omega)) \cdot q^h \mathrm{d}s(x) = \int_{\Gamma_{C,a}} q_n^h(\sigma_n(p_\Omega) + (\mathcal{N}'(u_\Omega))_n - \gamma(p_\Omega)_n)\mathrm{d}s(x),$$

and $\int_{\Gamma_{C,a}} \theta\sigma_n(q^h)(p_\Omega)_n\mathrm{d}s(x) = 0$. These equalities show that the adjoint state field $p_\Omega \in V$ satisfies

$$a(q^h, p_\Omega) - \int_{\Gamma_{C,i}} \frac{\theta}{\gamma}(\sigma_n(p_\Omega) + (\mathcal{N}'(u_\Omega))_n)\sigma_n(q^h)\mathrm{d}s(x) - \int_{\Gamma_{C,a}} \theta\sigma_n(q^h)(p_\Omega)_n\mathrm{d}s(x)$$

$$- \int_{\Gamma_{C,a}} q_n^h(\sigma_n(p_\Omega) + (\mathcal{N}'(u_\Omega))_n - \gamma(p_\Omega)_n)\mathrm{d}s(x)$$

$$= -\int_\Omega \mathcal{M}'(u_\Omega) \cdot q^h \, \mathrm{d}x - \int_{\partial\Omega} \mathcal{N}'(u_\Omega) \cdot q^h \, \mathrm{d}s(x), \quad \forall q^h \in V^h,$$

leading then to

$$a(q^h, p_\Omega) - \int_{\Gamma_C} \frac{\theta}{\gamma}(\sigma_n(p_\Omega) + (\mathcal{N}'(u_\Omega))_n)\sigma_n(q^h)\mathrm{d}s(x)$$

$$+ \int_{\Gamma_{C,a}} \frac{1}{\gamma}(\sigma_n(p_\Omega) + (\mathcal{N}'(u_\Omega))_n - \gamma(p_\Omega)_n)(\theta\sigma_n(q^h) - \gamma q_n^h)\mathrm{d}s(x)$$

$$= -\int_\Omega \mathcal{M}'(u_\Omega) \cdot q^h \, \mathrm{d}x - \int_{\partial\Omega} \mathcal{N}'(u_\Omega) \cdot q^h \, \mathrm{d}s(x).$$

Since $\Gamma_{C,a} := \{x \in \Gamma_C | \sigma_n(u_\Omega) < 0, (u_\Omega)_n = g\}$, then $H(-(\sigma_n(u_\Omega(x)) - \gamma(((u_\Omega)_n(x) - g))) = \chi_{\Gamma_{C,a}} = \begin{cases} 1 \text{ if } x \in \Gamma_{C,a}, \\ 0 \text{ otherwise}. \end{cases}$, which implies that (2.17) is satisfied. $\qquad\square$

Remark 24. *In the event that Assumption 16 is not satisfied, one cannot expect a convergence result because (2.7) prescribes a Neumann condition on $\Gamma_{C,b}$ which will not necessarily be asymptotically satisfied by the solution to (2.16). We address this problem in section 2.3.5 by a slight modification of the equation satisfied by p_Ω^h.*

2.3.4 Convergence analysis

The aim of this section is to present an a priori convergence result of the Nitsche-based formulation (2.7) with respect to the mesh parameter h. This result requires a supplementary assumption on the convergence of the effective contact area (i.e. a supplementary condition on the convergence of u_Ω^h towards u_Ω). For the sake of simplicity and clarity of this section and the next one, we will no longer indicate the dependence of the solution with respect to Ω and just use

$$u = u_\Omega, u^h = u_\Omega^h, p = p_\Omega \text{ and } p^h = p_\Omega^h.$$

Moreover, we introduce the two following quantities relative to the contact status:

$$\beta_h = -\sigma_n(u^h) + \gamma(u_n^h - g), \beta = -\sigma_n(u) + \gamma(u_n - g),$$

and recall that $\Gamma_{C,a} := \{x \in \Gamma_C | \beta > 0\}$ and introduce also the discrete effective contact area

$$\Gamma_{C,a}^h := \{x \in \Gamma_C | \beta_h > 0\}.$$

Remark 25. *In practice, β actually depends on h as $\gamma = \gamma_0/h_T$. However, $H(\beta)$ being the characteristic function of $\Gamma_{C,a}$, $H(\beta) = \chi_{\Gamma_{C,a}} = \begin{cases} 1 \ for \ x \in \Gamma_{C,a} \\ 0 \ otherwise \end{cases}$, it does not depend on h.*

We first introduce the following lemma on the weak convergence of $H(\beta^h)$ that is required for the main convergence result.

Lemma 26. *Suppose that the solution u to Problem (2.1) belongs to $(H^{\frac{3}{2}+\nu})^d$ with $\nu > 0$ and $d = 2$ or $d = 3$ and that assumptions 16 holds. Then, $|H(\beta) - H(\beta_h)| \xrightarrow{\ *\ } 0$ in L^∞ (Γ_C), in the sense that $\forall \phi \in L^1(\Gamma_C)$*

$$\lim_{h \to 0} \int_{\Gamma_C} |H(\beta) - H(\beta_h)| \phi \, \mathrm{d}s(x) = 0.$$

Consequently, $H(\beta_h) \xrightarrow{\ *\ } \chi_{\Gamma_{C,a}}$ in L^∞ (Γ_C).

Proof. Still for $\sigma_n(u)$ a particular element of its class in $L^2(\Gamma_C)$, we introduce the measurable set

$$A_\delta = \{x \in \Gamma_C | \sigma_n(u) \le -\delta\} \subset \Gamma_{C,a}. \tag{2.18}$$

It corresponds to the contact area where contact actually occurs for u and where the contact pressure is greater than δ. We also introduce N_δ^h a subset of A_δ where the contact does not occur for u^h defined by

$$N_\delta^h = \{x \in A_\delta | \sigma_n(u^h) - \gamma(u_n^h - g) > 0\}.$$

So on N_δ^h, it holds

$$|[\sigma_n(u^h) - \gamma(u_n^h - g)]_- + \sigma_n(u)| \ge \delta,$$

which implies

$$\int_{N_\delta^h} |[\sigma_n(u^h) - \gamma(u_n^h - g)]_- + \sigma_n(u)|^2 \, \mathrm{d}s(x) \ge \delta^2 |N_\delta^h|,$$

where $|\cdot|$ stands for the Lebesgue measure. Using (2.13) in Proposition 20, it finally holds

$$|N_\delta^h| \le \frac{Ch^{2\nu}}{\delta^2}. \tag{2.19}$$

Now, introducing I_δ the measurable set where no contact occurs for u with a separation greater than δ defined by

$$I_\delta = \{x \in \Gamma_C | u_n \le g - \delta\},$$

and

$$M_\delta^h = \{x \in I_\delta, \sigma_n(u^h) - \gamma(u_n^h - g) \le 0\},$$

its subset where contact occurs for u^h, we can write on M_δ^h

$$|-\frac{\sigma_n(u^h)}{\gamma} + (u_n^h - g) - (u_n - g)| \ge \delta.$$

This implies

$$\int_{M_\delta^h} |-\frac{\sigma_n(u^h)}{\gamma} + (u_n^h - u_n)|^2 \, \mathrm{d}s(x) \ge \delta^2 |M_\delta^h|.$$

Using (2.12) in Proposition 20, it finally holds

$$|M_\delta^h| \le \frac{Ch^{1+2\nu}}{\delta^2}. \tag{2.20}$$

Under Assumption 16, $\forall \delta > 0$ and $\forall \phi \in L^1(\Gamma_C)$, we write

$$\int_{\Gamma_C} |H(\beta) - H(\beta_h)|\phi \, \mathrm{d}s(x) = \int_{A_\delta} (1 - H(\beta_h))\phi \, \mathrm{d}s(x) + \int_{I_\delta} H(\beta_h)\phi \, \mathrm{d}s(x)$$
$$+ \int_{\Gamma_C/(A_\delta \cup I_\delta)} |H(\beta) - H(\beta_h)|\phi \, \mathrm{d}s(x).$$

However,

$$\int_{A_\delta} (1 - H(\beta_h))\phi \, \mathrm{d}s(x) = -\int_{N_\delta^h} \phi \, \mathrm{d}s(x),$$

and using (2.19)

$$\lim_{h \to 0} \int_{N_\delta^h} \phi \, \mathrm{d}s(x) = 0.$$

Similarly

$$\int_{I_\delta} H(\beta_h)\phi \, \mathrm{d}s(x) = \int_{M_\delta^h} \phi \, \mathrm{d}s(x),$$

and using (2.20)

$$\lim_{h \to 0} \int_{M_\delta^h} \phi \, \mathrm{d}s(x) = 0.$$

Since the measure $\Gamma_C \setminus (A_\delta \cup I_\delta)$ tends to 0 when δ tends to 0 under assumption 16, we finally obtain

$$\lim_{h \to 0} \int_{\Gamma_C} |H(\beta) - H(\beta_h)|\phi \, \mathrm{d}s(x) = 0.$$

$\square$

Let us consider the following assumption on the convergence of the effective contact area.

Assumption 27. *There exist $\omega > 0$, $C > 0$ independent of h such that $\Gamma_{C,a}^h \cap \Gamma_{C,i}$ is bounded as follows:*

$$|\Gamma_{C,a}^h \cap \Gamma_{C,i}| \leq Ch^\omega.$$

We present now our main convergence result of the discrete Nitsche-based adjoint state formulation (2.16).

Theorem 28. *Suppose that the solution p to Problem (2.7) and u the solution to Problem (2.1) belong to $(H^{\frac{3}{2}+\nu}(\Omega))^d$ with $\nu > 0$ and $d = 2$ or $d = 3$. Suppose that the parameter γ_0 is sufficiently large and that Assumptions 16 holds, then, it exists $C > 0$ independent of h such that the solution $p^h \in V^h$ to Problem (2.16) satisfies*

$$\|p - p^h\|_{1,\Omega}^2 + \|H(\beta_h)\gamma^{-\frac{1}{2}}(\sigma_n(p^h - p) - \gamma(p_n^h - p_n))\|_{0,\Gamma_C}^2$$

$$\leq C \left(\int_{\Gamma_{C,a}} (1 - H(\beta_h))\sigma_n^2(p)\mathrm{d}s(x) + \int_{\Gamma_{C,i}} H(\beta_h)\gamma p_n^2 \mathrm{d}s(x) \right)$$

$$+ C \inf_{q^h \in V^h} \left\{ \left(\|\gamma^{-\frac{1}{2}}\sigma_n(q^h - p)\|_{0,\Gamma_C}^2 + \|\gamma^{\frac{1}{2}}(q_n^h - p_n)\|_{0,\Gamma_C}^2 + \|q^h - p\|_{1,\Omega}^2 \right) \right\}$$

$$+ C \left(\|u - u^h\|_{1,\Omega}^2 + \|(H(\beta^h) - H(\beta))(\mathcal{N}'(u))_n\|_{0,\Gamma_C}^2 \right).$$

Moreover, if Assumption 27 holds for $\omega > 1$, we deduce that

$$\lim_{h \to 0} \|p^h - p\|_{1,\Omega}^2 = 0.$$

Proof. Using the coercivity and continuity of $a(\cdot, \cdot)$, we write for any $q^h \in V^h$

$$\alpha\|p - p^h\|_{1,\Omega}^2 \leq a(p - p^h, p - p^h)$$
$$= a(p - p^h, p - q^h + q^h - p^h)$$
$$\leq C\|p - p^h\|_{1,\Omega} \|p - q^h\|_{1,\Omega} + a(p - p^h, q^h - p^h)$$
$$\leq \frac{\alpha}{2}\|p - p^h\|_{1,\Omega}^2 + \frac{C^2}{2\alpha}\|p - q^h\|_{1,\Omega}^2 + a(p, q^h - p^h) - a(p^h, q^h - p^h),$$

where $\alpha > 0$ is the ellipticity constant of $a(\cdot, \cdot)$, and $C > 0$ a generic constant independent of h in the whole study. We can rewrite the term $a(p, q^h - p^h) - a(p^h, q^h - p^h)$ as p solves

(2.7), p^h solves (2.16) and using Lemma 23, it yields:

$$
\begin{aligned}
\frac{\alpha}{2}\|p - p^h\|_{1,\Omega}^2 \leq{} & \frac{C^2}{2\alpha}\|p - q^h\|_{1,\Omega}^2 - \int_{\Gamma_C} \frac{\theta}{\gamma}\sigma_n(p^h - p)\sigma_n(q^h - p^h)\,\mathrm{d}s(x) \\
& + \int_{\Gamma_C} \frac{1}{\gamma}H(\beta_h)(\sigma_n(p^h) - \gamma p_n^h - (\sigma_n(p) - \gamma p_n))(\theta\sigma_n(q^h - p^h) - \gamma(q_n^h - p_n^h))\,\mathrm{d}s(x) \\
& + \int_{\Gamma_C} \frac{1}{\gamma}(H(\beta_h) - H(\beta))(\sigma_n(p) - \gamma p_n)(\theta\sigma_n(q^h - p^h) - \gamma(q_n^h - p_n^h))\,\mathrm{d}s(x). \\
& + \int_{\Gamma_C} \frac{\theta}{\gamma}((1 - H(\beta))\mathcal{N}'(u) - (1 - H(\beta^h))\mathcal{N}'(u^h))_n\sigma_n(q^h - p^h)\,\mathrm{d}s(x) \\
& + \int_{\Gamma_C} (H(\beta)\mathcal{N}'(u) - H(\beta^h)\mathcal{N}'(u^h))_n(q_n^h - p_n^h)\,\mathrm{d}s(x) \\
& - \int_{\Omega} (\mathcal{M}'(u) - \mathcal{M}'(u^h)).(q^h - p^h)dx - \int_{\partial\Omega} (\mathcal{N}'(u) - \mathcal{N}'(u^h)).(q^h - p^h)ds(x).
\end{aligned}
\tag{2.21}
$$

The first integral term in (2.21) is bounded as follows, using Young's inequality for any $\xi_1 > 0$:

$$
\begin{aligned}
-\int_{\Gamma_C} \frac{\theta}{\gamma}\sigma_n(p^h - p)\sigma_n(q^h - p^h)\,\mathrm{d}s(x) &= -\int_{\Gamma_C} \frac{\theta}{\gamma}\sigma_n((p^h - q^h) + (q^h - p))\sigma_n(q^h - p^h)\,\mathrm{d}s(x) \\
&= \int_{\Gamma_C} \frac{\theta}{\gamma}\sigma_n(q^h - p^h)\sigma_n(q^h - p^h)\,\mathrm{d}s(x) - \int_{\Gamma_C} \frac{\theta}{\gamma}\sigma_n(q^h - p)\sigma_n(q^h - p^h)\,\mathrm{d}s(x) \\
&\leq \theta\|\gamma^{-\frac{1}{2}}\sigma_n(q^h - p^h)\|_{0,\Gamma_C}^2 + |\theta|\ \|\gamma^{-\frac{1}{2}}\sigma_n(q^h - p)\|_{0,\Gamma_C}\|\gamma^{-\frac{1}{2}}\sigma_n(q^h - p^h)\|_{0,\Gamma_C} \\
&\leq \theta\|\gamma^{-\frac{1}{2}}\sigma_n(q^h - p^h)\|_{0,\Gamma_C}^2 + \frac{\xi_1\theta^2}{2}\|\gamma^{-\frac{1}{2}}\sigma_n(q^h - p)\|_{0,\Gamma_C}^2 + \frac{1}{2\xi_1}\|\gamma^{-\frac{1}{2}}\sigma_n(q^h - p^h)\|_{0,\Gamma_C}^2 \\
&\leq (\theta + \frac{1}{2\xi_1})\|\gamma^{-\frac{1}{2}}\sigma_n(q^h - p^h)\|_{0,\Gamma_C}^2 + \frac{\xi_1\theta^2}{2}\|\gamma^{-\frac{1}{2}}\sigma_n(q^h - p)\|_{0,\Gamma_C}^2, \\
&\leq \frac{C_0}{\gamma_0}(\theta + \frac{1}{2\xi_1})\left(\|p - q^h\|_{1,\Omega}^2 + \|p - p^h\|_{1,\Omega}^2\right) + \frac{\xi_1\theta^2}{2}\|\gamma^{-\frac{1}{2}}\sigma_n(q^h - p)\|_{0,\Gamma_C}^2.
\end{aligned}
\tag{2.22}
$$

Concerning the second integral term in (2.21), we derive the following estimate for any

$\xi_2 > 0$:

$$\int_{\Gamma_C} \frac{1}{\gamma} H(\beta_h)(\sigma_n(p^h) - \gamma p_n^h - (\sigma_n(p) - \gamma p_n))(\theta\sigma_n(q^h - p^h) - \gamma(q_n^h - p_n^h)) \, \mathrm{d}s(x)$$

$$= -\int_{\Gamma_C} \frac{1}{\gamma} H(\beta_h)(\sigma_n(p^h - p) - \gamma(p_n^h - p_n))^2 \, \mathrm{d}s(x)$$

$$+ \int_{\Gamma_C} \frac{1}{\gamma} H(\beta_h)(\sigma_n(p^h - p) - \gamma(p_n^h - p_n))(\sigma_n(q^h - p) - \gamma(q_n^h - p_n)) \, \mathrm{d}s(x)$$

$$+ (\theta - 1) \int_{\Gamma_C} \frac{1}{\gamma} H(\beta_h)(\sigma_n(p^h - p) - \gamma(p_n^h - p_n))\sigma_n(q^h - p^h) \, \mathrm{d}s(x)$$

$$\leq (-1 + |\theta - 1|\frac{\xi_2}{2} + \frac{\xi_2}{2})\|H(\beta_h)\gamma^{-\frac{1}{2}}(\sigma_n(p^h - p) - \gamma(p_n^h - p_n))\|_{0,\Gamma_C}^2 \qquad (2.23)$$

$$+ \frac{1}{2\xi_2}\|H(\beta_h)\gamma^{-\frac{1}{2}}(\sigma_n(q^h - p) - \gamma(q_n^h - p_n))\|_{0,\Gamma_C}^2$$

$$+ \frac{1}{2\xi_2}|\theta - 1| \, \|H(\beta_h)\gamma^{-\frac{1}{2}}\sigma_n(q^h - p^h)\|_{0,\Gamma_C}^2,$$

$$\leq (-1 + |\theta - 1|\frac{\xi_2}{2} + \frac{\xi_2}{2})\|H(\beta_h)\gamma^{-\frac{1}{2}}(\sigma_n(p^h - p) - \gamma(p_n^h - p_n))\|_{0,\Gamma_C}^2$$

$$+ \frac{1}{2\xi_2} \left(\|\gamma^{-\frac{1}{2}}\sigma_n(q^h - p)\|_{0,\Gamma_C}^2 + \|\gamma^{\frac{1}{2}}(q_n^h - p_n)\|_{0,\Gamma_C}^2\right)$$

$$+ \frac{C_0}{\gamma_0}\frac{1}{2\xi_2}(\|p - q^h\|_{1,\Omega}^2 + \|p - p^h\|_{1,\Omega}^2).$$

The third integral term in (2.21) is split as follows:

$$\int_{\Gamma_C} \frac{1}{\gamma}(H(\beta_h) - H(\beta))(\sigma_n(p) - \gamma p_n)(\theta\sigma_n(q^h - p^h) - \gamma(q_n^h - p_n^h)) \, \mathrm{d}s(x)$$

$$= \int_{\Gamma_{C,a}} \frac{1}{\gamma}(H(\beta_h) - 1) \, \sigma_n(p)(\theta\sigma_n(q^h - p^h) - \gamma(q_n^h - p_n^h)) \, \mathrm{d}s(x) \qquad (2.24)$$

$$+ \int_{\Gamma_{C,i}} \frac{H(\beta_h)}{\gamma} \, (\sigma_n(p) - \gamma p_n)(\theta\sigma_n(q^h - p^h) - \gamma(q_n^h - p_n^h)) \, \mathrm{d}s(x).$$

For the first integral term of the right hand side of (2.24), on $\Gamma_{C,a}$, we obtain, using the trace

inequality and for any $\xi_3 > 0$

$$\int_{\Gamma_{C,a}} \frac{1}{\gamma}(H(\beta_h) - 1)\, \sigma_n(p)(\theta\sigma_n(q^h - p^h) - \gamma(q_n^h - p_n^h))\, \mathrm{d}s(x)$$

$$\leq \frac{1}{2\xi_3} \int_{\Gamma_{C,a}} (1 - H(\beta_h))\sigma_n^2(p)\mathrm{d}s(x) + \xi_3 \int_{\Gamma_{C,a}} (\frac{\theta^2}{\gamma^2}\sigma_n^2(q^h - p^h) + (q^h - p^h)^2)\mathrm{d}s(x)$$

$$\leq \frac{1}{2\xi_3} \int_{\Gamma_{C,a}} (1 - H(\beta_h))\sigma_n^2(p)\mathrm{d}s(x) + \xi_3(\theta^2\|\gamma^{-1}\sigma_n(q^h - p^h)\|_{0,\Gamma_{C,a}}^2 + C\|q^h - p^h\|_{1,\Omega}^2)$$

$$\leq \frac{1}{2\xi_3} \int_{\Gamma_{C,a}} (1 - H(\beta_h))\sigma_n^2(p)\mathrm{d}s(x) + \xi_3(\frac{\theta^2 C_0 h^T}{\gamma_0^2} + C)(\|q^h - p\|_{1,\Omega}^2 + \|p - p^h\|_{1,\Omega}^2).$$

$$(2.25)$$

For the second integral term of the right hand side of (2.24) on $\Gamma_{C,i}$, we obtain for any $\xi_4 > 0$

$$\int_{\Gamma_{C,i}} \frac{H(\beta_h)}{\gamma}\, (\sigma_n(p) - \gamma p_n)(\theta\sigma_n(q^h - p^h) - \gamma(q_n^h - p_n^h))\, \mathrm{d}s(x)$$

$$\leq \frac{1}{2\xi_4} \int_{\Gamma_{C,i}} \frac{H(\beta_h)}{\gamma}(\gamma p_n)^2 \mathrm{d}s(x)$$

$$+ \frac{\xi_4}{2} \int_{\Gamma_{C,i}} \frac{H(\beta_h)}{\gamma}(\theta\sigma_n(q^h - p + p - p^h) - \gamma(q_n^h - p_n + p_n - p_n^h))^2\, \mathrm{d}s(x)$$

$$\leq \frac{1}{2\xi_4} \int_{\Gamma_{C,i}} H(\beta_h)\gamma p_n^2 \mathrm{d}s(x) + 2\xi_4\|H(\beta_h)\gamma^{-\frac{1}{2}}(\sigma_n(p^h - p) - \gamma(p_n^h - p_n))\|_{0,\Gamma_{C,i}}^2,$$

$$+ 2\xi_4|\theta - 1|\, \|H(\beta_h)\gamma^{-\frac{1}{2}}\sigma_n(q^h - p^h)\|_{0,\Gamma_{C,i}}^2 + 2\xi_4\|H(\beta_h)(\sigma_n(q^h - p) - \gamma(q_n^h - p_n))\|_{0,\Gamma_{C,i}}^2$$

$$\leq \frac{1}{2\xi_4} \int_{\Gamma_{C,i}} H(\beta_h)\gamma p_n^2 \mathrm{d}s(x) + 2\xi_4\|H(\beta_h)\gamma^{-\frac{1}{2}}(\sigma_n(p^h - p) - \gamma(p_n^h - p_n))\|_{0,\Gamma_{C,i}}^2,$$

$$+ 2\xi_4|\theta - 1|\frac{C_0}{\gamma_0} \left(\|q^h - p\|_{1,\Omega}^2 + \|p - p^h\|_{1,\Omega}^2\right)$$

$$+ 2\xi_4 \left(\|\gamma^{-\frac{1}{2}}\sigma_n(q^h - p)\|_{0,\Gamma_C}^2 + \|\gamma^{\frac{1}{2}}(q_n^h - p_n)\|_{0,\Gamma_C}^2\right).$$

$$(2.26)$$

The fourth integral term in (2.21) can be estimated as follows using Lemma 21, the Lipschitz-

continuity of $\mathcal{N}'$ and for any $\xi_5 > 0$

$$
\int_{\Gamma_C} \frac{\theta}{\gamma}((1 - H(\beta))\mathcal{N}'(u) - (1 - H(\beta^h))\mathcal{N}'(u^h))_n \sigma_n(q^h - p^h) \, ds(x)
$$
$$
= \int_{\Gamma_C} \frac{\theta}{\gamma}((H(\beta^h) - H(\beta))\mathcal{N}'(u) + (1 - H(\beta^h))(\mathcal{N}'(u) - \mathcal{N}'(u^h)))_n \sigma_n(q^h - p^h) \, ds(x)
$$
$$
\leq |\theta| \left((\|(H(\beta^h) - H(\beta))(\mathcal{N}'(u))_n\|_{0,\Gamma_C} + \|\mathcal{N}'(u) - \mathcal{N}'(u^h)\|_{0,\Gamma_C})\|\gamma^{-1}\sigma_n(q^h - p^h)\|_{0,\Gamma_C} \right)
$$
$$
\leq C \frac{h^{1/2}}{\gamma_0} |\theta| (\|(H(\beta^h) - H(\beta))(\mathcal{N}'(u))_n\|_{0,\Gamma_C} + \|u - u^h\|_{0,\Gamma_C})\|q^h - p^h\|_{1,\Omega}
$$
$$
\leq C \frac{h^{1/2}}{\gamma_0} |\theta| \left(\frac{1}{\xi_5} \|(H(\beta^h) - H(\beta))(\mathcal{N}'(u))_n\|_{0,\Gamma_C} \right.
$$
$$
\left. + \frac{1}{\xi_5} \|u - u^h\|_{0,\Gamma_C}^2 + \xi_5 \|q^h - p\|_{1,\Omega}^2 + \xi_5 \|p - p^h\|_{1,\Omega}^2 \right),
$$
$$
(2.27)
$$

and similarly for the fifth integral term in (2.21), we obtain

$$
\int_{\Gamma_C} (H(\beta)\mathcal{N}'(u) - H(\beta^h)\mathcal{N}'(u^h))_n (q_n^h - p_n^h) \, ds(x)
$$
$$
= \int_{\Gamma_C} ((H(\beta) - H(\beta^h))\mathcal{N}'(u) + H(\beta^h)(\mathcal{N}'(u) - \mathcal{N}'(u^h)))_n (q_n^h - p_n^h) \, ds(x)
$$
$$
\leq \int_{\Gamma_C} (H(\beta) - H(\beta^h))(\mathcal{N}'(u))_n (q_n^h - p_n^h) \, ds(x) + \|\mathcal{N}'(u) - \mathcal{N}'(u^h)\|_{0,\Gamma_C} \|q_n^h - p_n^h\|_{0,\Gamma_C},
$$
$$
\leq C \left(\frac{1}{\xi_5} \|(H(\beta^h) - H(\beta))(\mathcal{N}'(u))_n\|_{0,\Gamma_C} + \frac{1}{\xi_5} \|u - u^h\|_{1,\Omega}^2 + \xi_5 \|q^h - p\|_{1,\Omega}^2 + \xi_5 \|p - p^h\|_{1,\Omega}^2 \right),
$$
$$
(2.28)
$$

and for the two last integral terms in (2.21) using additionally the Lipschitz-continuity of $\mathcal{M}'$

$$
- \int_{\Omega} (\mathcal{M}'(u) - \mathcal{M}'(u^h)).(q^h - p^h) dx - \int_{\partial\Omega} (\mathcal{N}'(u) - \mathcal{N}'(u^h)).(q^h - p^h) ds(x)
$$
$$
\leq C \left(\frac{1}{2\xi_5} \|u - u^h\|_{1,\Omega}^2 + \xi_5 \|q^h - p\|_{1,\Omega}^2 + \xi_5 \|p - p^h\|_{1,\Omega}^2 \right).
$$
$$
(2.29)
$$

Gathering now (2.22), (2.23), (2.25), (2.26), (2.27), (2.28) and (2.29) we obtain for ξ_2, ξ_3, ξ_4

and ξ_5 sufficiently small and for γ_0 sufficiently large the existence of $C > 0$ such that

$$\|p - p^h\|_{1,\Omega}^2 + \|H(\beta_h)\gamma^{-\frac{1}{2}}(\sigma_n(p^h - p) - \gamma(p_n^h - p_n))\|_{0,\Gamma_C}^2$$

$$\leq C \left(\int_{\Gamma_{C,a}} (1 - H(\beta_h))\sigma_n^2(p)\mathrm{d}s(x) + \int_{\Gamma_{C,i}} H(\beta_h)\gamma p_n^2\mathrm{d}s(x) \right)$$

$$+ C \left(\|\gamma^{-\frac{1}{2}}\sigma_n(q^h - p)\|_{0,\Gamma_C}^2 + \|\gamma^{\frac{1}{2}}(q_n^h - p_n)\|_{0,\Gamma_C}^2 + \|q^h - p\|_{1,\Omega}^2 \right)$$

$$+ C \left(\|u - u^h\|_{1,\Omega}^2 + \|(H(\beta^h) - H(\beta))(\mathcal{N}'(u))_n\|_{0,\Gamma_C} \right).$$

Finally, the proof of convergence is obtained thanks to the interpolation error exposed in [25] (Theorem 3.8), which shows that choosing q^h the Lagrange interpolate of p leads to

$$\lim_{h \to 0} \|p - q^h\|_{1,\Omega}^2 = 0, \quad \lim_{h \to 0} \|\gamma^{-\frac{1}{2}}\sigma_n(q^h - p)\|_{0,\Gamma_C}^2 = 0, \quad \lim_{h \to 0} \|\gamma^{\frac{1}{2}}q_n^h - p_n)\|_{0,\Gamma_C}^2 = 0.$$

Moreover, thanks to Lemma 26, $H(\beta_h) \xrightarrow{\;*\;} \chi_{\Gamma_{C,a}}$ gives $\lim_{h \to 0} \int_{\Gamma_{C,a}} (1 - H(\beta_h))\sigma_n^2(p)\mathrm{d}s(x) = 0$ and $|H(\beta) - H(\beta_h)| \xrightarrow{\;*\;} 0$ ensures $\lim_{h \to 0} \|(H(\beta^h) - H(\beta))(\mathcal{N}'(u))_n\|_{0,\Gamma_C} = 0$. Moreover, the continuity of p_n ensures $|p_n| \leq C$ with $C > 0$. With assumption 27, we can bound the first term in (2.26) as

$$\int_{\Gamma_{C,i}} H(\beta_h)\gamma p_n^2\mathrm{d}s(x) = \int_{\Gamma_{C,a}^h \cap \Gamma_{C,i}} \gamma \, p_n^2 \, \mathrm{d}s(x) \leq \frac{\gamma_0}{h}Ch^\omega \leq Ch^{\omega - 1}.$$

It suffices that $\omega > 1$ so that

$$\lim_{h \to 0} \int_{\Gamma_{C,a}^h \cap \Gamma_{C,i}} \gamma \, p_n^2 \, \mathrm{d}s(x) = 0.$$

$\square$

Note that in the numerical tests we provide in section 2.4.1, the condition $\omega > 1$ is satisfied for the studied range of mesh size.

2.3.5 Improved convergence result with an extended Neumann zone for the adjoint state

The aim of this section is to give a convergence result without the consideration of assumptions 16 and 27, i.e. without the consideration of zero measure of $\Gamma_{C,b}$ and without any assumption on the rate of convergence of the effective contact area. This result is obtained with a slight modification of the discrete adjoint state, extending a bit the part of the boundary where the Neumann condition is applied and with the use of quadratic finite elements.

Let us consider $\xi > 0$ a small parameter which is assumed to tend to zero when $h \to 0$, then the consideration of the following modified problem for the adjoint state:

$$
\begin{cases}
\text{Find } p^h \in V^h \text{ such that } \forall q^h \in V^h \\
a(p^h, q^h) - \displaystyle\int_{\Gamma_C} \frac{\theta}{\gamma} \sigma_n(p^h)\sigma_n(q^h)\mathrm{d}s(x) \\
+ \displaystyle\int_{\Gamma_C} \frac{1}{\gamma} H(-(\sigma_n(u^h) - \gamma(u_n^h - g)) - \xi))(\sigma_n(p^h) - \gamma p_n^h)(\theta\sigma_n(q^h) - \gamma q_n^h)\mathrm{d}s(x) \\
= -\displaystyle\int_{\Omega} \mathcal{M}'(u^h) \cdot q^h \, \mathrm{d}x - \int_{\partial\Omega} \mathcal{N}'(u^h) \cdot q^h \, \mathrm{d}s(x),
\end{cases} \tag{2.30}
$$

allows to state the following result.

Theorem 29. *Suppose that the solution u to Problem (2.1) belongs to $(H^{\frac{3}{2}+\nu}(\Omega))^d$ with $\nu > 1/2$ and p the solution to Problem (2.7) belongs to $(H^{\frac{3}{2}+\nu_2}(\Omega))^d$ with $\nu_2 > 0$ and $d = 2$ or $d = 3$. Suppose that the parameter γ_0 is sufficiently large, $k = 2$ (k being the degree of the finite element method) and $\xi \geq Ch^{\nu-1/2}$ with $C > 0$ arbitrary small enough and $\lim\limits_{h\to 0} \xi = 0$. Then, the solution $p^h \in V^h$ to Problem (2.30) satisfies*

$$
\lim_{h\to 0} \|p^h - p\|_{1,\Omega} = 0.
$$

Proof. We observe first that the consistency result of Lemma 23 is still valid using the convention $H(0) = 0$ (i.e. replacing $H(-(\sigma_n(u) - \gamma(u_n - g)))$ by $\chi_{\Gamma_{C,a}}$). Then the proof of Theorem 28 can be followed with limited modifications that we focus on. Let us denote

$$
\tilde{\beta}_h = -\sigma_n(u^h) + \gamma(u_n^h - g) - \xi.
$$

The estimate (2.21) of the proof of Theorem 28 becomes

$$
\begin{aligned}
\frac{\alpha}{2}\|p - p^h\|_{1,\Omega}^2 &\leq \frac{C^2}{2\alpha}\|p - q^h\|_{1,\Omega}^2 - \int_{\Gamma_C} \frac{\theta}{\gamma}\sigma_n(p^h - p)\sigma_n(q^h - p^h)\,\mathrm{d}s(x) \\
&+ \int_{\Gamma_C} \frac{1}{\gamma}H(\tilde{\beta}_h)(\sigma_n(p^h) - \gamma p_n^h - (\sigma_n(p) - \gamma p_n))(\theta\sigma_n(q^h - p^h) - \gamma(q_n^h - p_n^h))\,\mathrm{d}s(x) \\
&+ \int_{\Gamma_C} \frac{1}{\gamma}(H(\tilde{\beta}_h) - H(\beta))(\sigma_n(p) - \gamma p_n)(\theta\sigma_n(q^h - p^h) - \gamma(q_n^h - p_n^h))\,\mathrm{d}s(x).
\end{aligned} \tag{2.31}
$$

The first and second integral terms in (2.31) are estimated thanks to (2.22) and (2.23), respectively, replacing β_h by $\tilde{\beta}_h$ and the same convergence to zero is obtained at the end. The third term in (2.31) is split similarly as in (2.24) taking into account the fact that $\Gamma_{C,b}$

is no longer supposed to be of zero measure. So it gives

$$\int_{\Gamma_C} \frac{1}{\gamma}(H(\tilde{\beta}_h) - H(\beta))(\sigma_n(p) - \gamma p_n)(\theta\sigma_n(q^h - p^h) - \gamma(q_n^h - p_n^h)) \, \mathrm{d}s(x)$$

$$= \int_{\Gamma_{C,a}} \frac{1}{\gamma}(H(\tilde{\beta}_h) - 1) \, \sigma_n(p)(\theta\sigma_n(q^h - p^h) - \gamma(q_n^h - p_n^h)) \, \mathrm{d}s(x) \tag{2.32}$$

$$+ \int_{\Gamma_{C,i}\cup\Gamma_{C,b}} \frac{H(\tilde{\beta}_h)}{\gamma} \, (\sigma_n(p) - \gamma p_n)(\theta\sigma_n(q^h - p^h) - \gamma(q_n^h - p_n^h)) \, \mathrm{d}s(x).$$

The first integral term of the right hand side of (2.32) is treated as in (2.25). It remains to verify that

$$\lim_{h\to 0} \frac{1}{2\xi_3} \int_{\Gamma_{C,a}} (1 - H(\tilde{\beta}_h))\sigma_n^2(p)\mathrm{d}s(x) = 0. \tag{2.33}$$

Let us still denote A_δ the set defined by (2.18) where the contact actually occurs for u and the contact pressure is greater than δ, and consider

$$\tilde{N}_{\delta,\xi}^h = \{x \in A_\delta | \sigma_n(u^h) - \gamma(u_n^h - g) > -\xi\},$$

the subset where the discrete adjoint state is submitted to a Neumann condition. We obtain on $\tilde{N}_{\delta,\xi}^h$ for $\xi < \delta$,

$$|[\sigma_n(u^h) - \gamma(u_n^h - g)]_- + \sigma_n(u)| \geq \delta - \xi,$$

so that

$$\int_{\tilde{N}_\delta^h} |[\sigma_n(u^h) - \gamma(u_n^h - g)]_- + \sigma_n(u)|^2 \, \mathrm{d}s(x) \geq (\delta - \xi)^2|\tilde{N}_\delta^h|,$$

which leads, using (2.13) in Proposition 20 to $|\tilde{N}_\delta^h| \leq \frac{Ch^{2\nu}}{(\delta-\xi)^2}$. We have

$$0 \leq \int_{\Gamma_{C,a}} (1 - H(\tilde{\beta}_h))\sigma_n^2(p)\mathrm{d}s(x) \leq \int_{\tilde{N}_\delta^h} \sigma_n^2(p)\mathrm{d}s(x) + \int_{\Gamma_{C,a}\backslash A_\delta} \sigma_n^2(p)\mathrm{d}s(x).$$

For an arbitrary $\delta > 0$, the term $\displaystyle\int_{\tilde{N}_\delta^h} \sigma_n^2(p)\mathrm{d}s(x)$ tends to zero as h tends to zero and the term $\displaystyle\int_{\Gamma_{C,a}\backslash A_\delta} \sigma_n^2(p)\mathrm{d}s(x)$ tends to zero when δ tends to zero. So that we obtain (2.33).

Now, concerning the second integral term of the right hand side of (2.32), we follow (2.26) and it remains only to prove that

$$\lim_{h\to 0} \int_{\Gamma_{C,i}\cup\Gamma_{C,b}} H(\beta_h)\gamma p_n^2\mathrm{d}s(x) = 0. \tag{2.34}$$

To this aim, denoting $\Gamma_{C,a}^h = \{x \in \Gamma_C | \tilde{\beta} > 0\}$, we obtain

$$\int_{(\Gamma_{C,i}\cup\Gamma_{C,b})\cap\Gamma_{C,a}^h} |[\sigma_n(u^h) - \gamma(u^n - g)]_- + \sigma_n(u)|^2\mathrm{d}s(x) \geq \xi^2|(\Gamma_{C,i} \cup \Gamma_{C,b}) \cap \Gamma_{C,a}^h|,$$

and still using (2.13) we deduce $|(\Gamma_{C,i} \cup \Gamma_{C,b}) \cap \Gamma_{C,a}^h| \leq C\frac{h^{2\nu}}{\xi^2}$. So that

$$\int_{\Gamma_{C,i} \cup \Gamma_{C,b}} H(\beta_h)\gamma p_n^2 \mathrm{d}s(x) = \int_{(\Gamma_{C,i} \cup \Gamma_{C,b}) \cap \Gamma_{C,a}^h} \gamma p_n^2 \mathrm{d}s(x) \leq C\gamma_0\frac{h^{2\nu-1}}{\xi^2},$$

since p is bounded on Γ_C. Consequently, (2.34) holds for $\nu > 1/2$ and $\xi > Ch^{\nu-1/2}$ which ends the proof. □

Extending the part of the boundary on which a Neumann condition is considered, makes the discrete adjoint problem tend to the continuous adjoint which satisfies a Neumann condition on $\Gamma_{C,b}$. Of course, this continuous adjoint may not allow to recover the conical shape derivative given by Theorem 13 for all direction Θ. An interesting and open question would be to verify that it allows to obtain a descent direction of the shape optimization problem.

2.4 Numerical experiments

In this section, we illustrate the convergence analysis with some numerical tests on an elastic hollow cylinder in contact with a plane rigid foundation. We refer to [**?**] for more details on our optimization method. The different tests are performed using GetFEM++ [87] with quadratic Lagrange finite elements on a polar mesh shown in Figure 2.2.
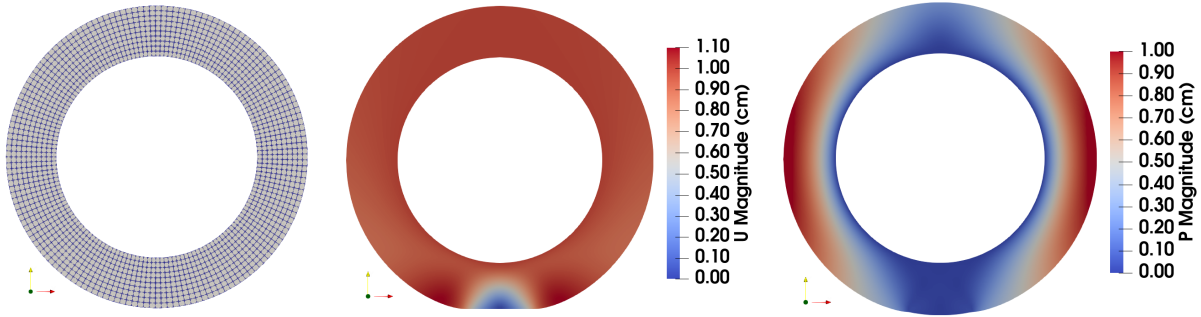
Figure 2.2: Hollow cylinder in contact with the obstacle. From left to right: structured polar mesh of the hollow cylinder; approximated displacement; approximated adjoint state.

We consider the elastic hollow cylinder presented in Figure 2.2 with an interior radius $R_i = 20$ cm and an exterior radius $R_e = 30$cm. The contact might occur between the boundary Γ_C on the exterior radius with a horizontal and rigid obstacle located at the bottom of the cylinder. The gravity forces are neglected and $f = 0$. We impose a vertical displacement $u_D = [0, -1\text{cm}]$ on the rigid boundary Γ_D. The optimization criteria are set to $\mathcal{M}(u) = F \cdot u$ where $F = [0, -1N]$ and $\mathcal{N}(u) = 0$ for the sake of simplicity. The result of the finite element computation for both the contact problem and the consistent Nitsche-based adjoint state problem (2.16) are shown in Figure 2.2.

2.4.1 Convergence of the Nitsche-based approximation of the adjoint state problem

We first focus on the convergence rate of the Nitsche-based approximation of the adjoint state problem (2.16). The reference solution p_{ref}^h of (2.16) is computed on a very thin mesh ($h = 0.0625$ cm). The slopes plotted in Figure 2.3 describe the convergence rates associated to the direct problem (2.11) for the variable u^h and the adjoint state problem (2.16) for the variable p^h. The relative $H^1(\Omega)-$norm is

$$\frac{\|p_{ref}^h - p^h\|_{1,\Omega}^2}{\|p_{ref}^h\|_{1,\Omega}^2},$$

for

$$\|v^h\|_{1,\Omega}^2 = \int_\Omega (v^h)^2 \mathrm{d}x + \int_\Omega |\nabla v^h|^2 \mathrm{d}x.$$

The left graph of Figure 2.3 presents both the convergence rate for the solution u^h to the direct problem (2.11) and the solution p^h to the adjoint state problem (2.16). The convergence rate for u^h is in good accordance with the theoretical results given in [25].
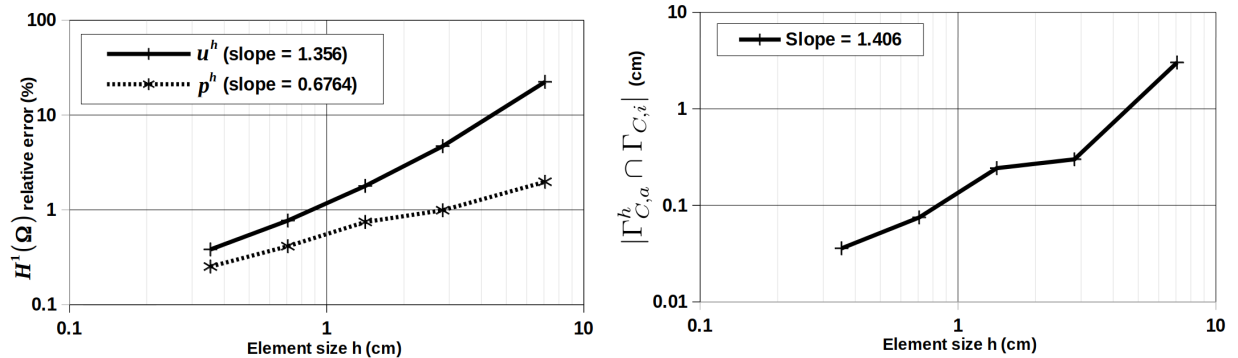
Figure 2.3: Error curves for $\theta = -1$. Left: relative $H^1(\Omega)$-norm on the displacement and the adjoint state variable. Right: length of $\Gamma_{C,a}^h \cap \Gamma_{C,i}$.

The convergence of p^h towards p solution to (2.7) is also observed, accordingly to our theoretical results, but with a slower convergence rate compared to u^h. This slower convergence has at least two causes: a Dirichlet-Neumann transition between $\Gamma_{C,a}$ and $\Gamma_{C,i}$, which limits the regularity of p, and the convergence of $\Gamma_{C,a}^h$ towards $\Gamma_{C,a}$ which depends on u^h. The convergence of the effective contact area is illustrated in the right graph of Figure 2.3. The coefficient ω of Assumption 27 is found approximately equal to 1.406, which is compatible with the requirement of Theorem 28 ($\omega > 1$). One can see on the left part of Figure 2.4 that the maximum of difference between p and p^h is indeed located on the transition between $\Gamma_{C,a}$ and $\Gamma_{C,i}$.
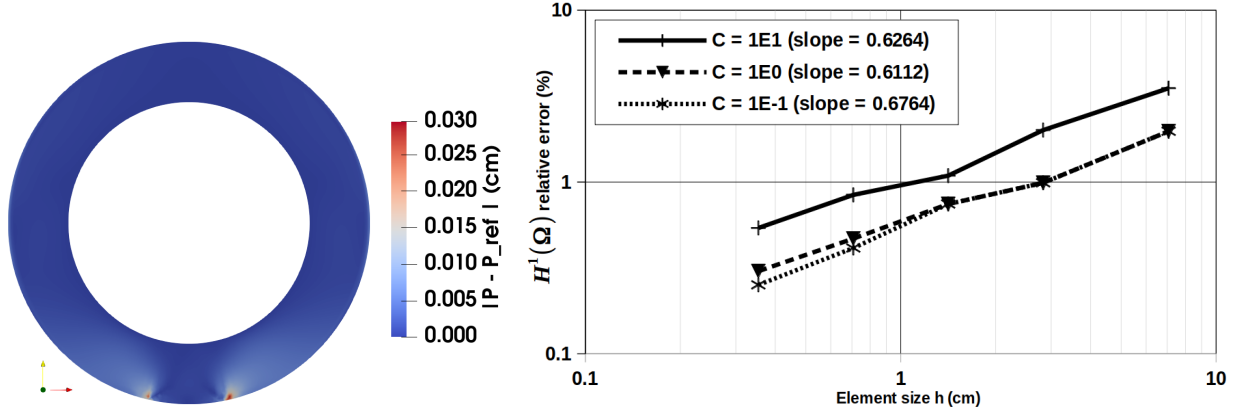
Figure 2.4: Left: Error map $|p^h - p^h_{ref}|$. Right: Error curves for the adjoint state problem p^h for $\theta = -1$. Relative $H^1(\Omega)$-norm on the displacement and the adjoint state variable for different values of C.

Now, concerning the strategy described in Section 2.3.5 with an extended Neumann zone on the contact boundary, we present a convergence test in the right graph of Figure 2.4. We recall that this strategy consists in replacing $H(\beta_h)$ by $H(\beta_h - \xi)$ in the proposed Nitsche-based method. We choose $\xi = C\sqrt{h_T}$ with different values of $C > 0$. Theorem 29 ensures the convergence of p^h for any value of $C > 0$. The strategy is respectively performed for C values of $0.1, 1$ and 10. We can see that this strategy does not deteriorate the order of convergence of p^h and starts to degrade the approximation error for a too high value of the constant ($C = 10$). This strategy can therefore be interesting since it ensures convergence without degradation of the approximation as soon as the constant C is taken with a moderate value.

2.4.2   Comparison of Nitsche-based adjoint state formulations

We focus now on the convergence rate of the adjoint state of the Nitsche-based formulation (2.15). Again, the reference solution p^h_{ref} is computed on problem (2.16) for a very thin mesh ($h = 0.0625$cm). Despite the non-consistence of this formulation, one can see on the slopes presented in Figure (2.5) that the convergence of $\tilde{p}^h$ solution to problem (2.15) is still ensured, with a convergence rate slightly deteriorated according to the one for the Nitsche-based approximation of the adjoint state presented in Figure 2.3.
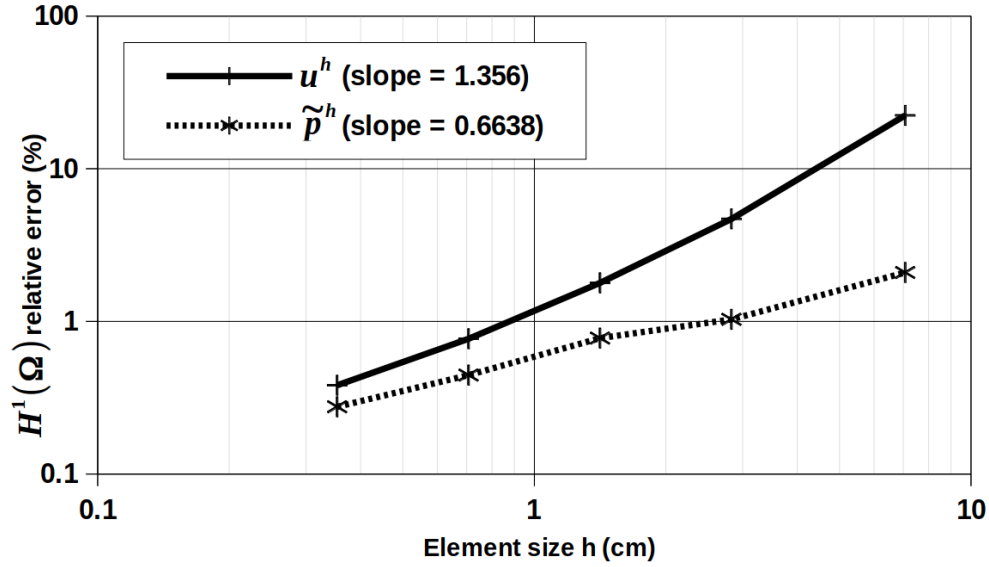
Figure 2.5: Error curves for the direct problem using Nitsche's method and for the adjoint state problem of the Nitsche-based approximation ($\theta = -1$).

Finally, in Figure 2.6, we present an example of shape optimization process which is taken from the previous chapter (see Figure 1.24 for the shape optimization with a slightly stronger load magnitude and for the sole energy criterion minimization J_e). The optimizable boundary is only the interior part, which is submitted to a homogeneous Neumann condition. For the same initial geometry, the shape optimization is performed either with the adjoint state variable approximated by (2.16) or (2.15). One can see on Figure 2.6 that both of the two approximations lead to quasi-identical shapes, meaning that, at least for this example, the two strategies can be indifferently applied.
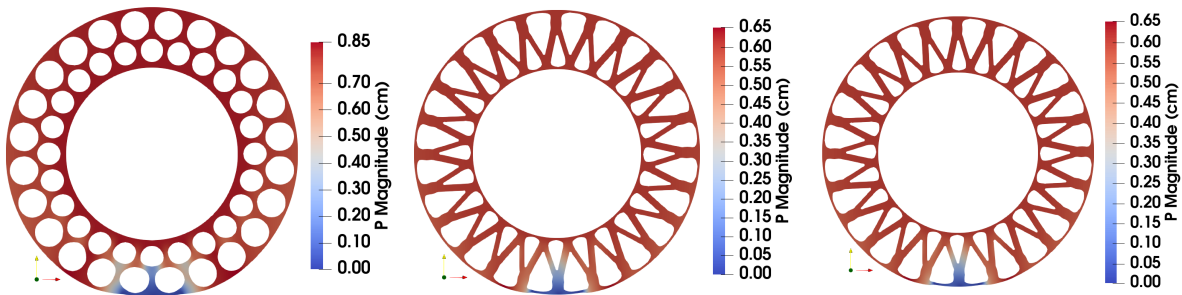
Figure 2.6: Shape optimization. The adjoint state variable is displayed. From left to right: initial geometry, optimal geometry with adjoint state computed on formulation (2.16), optimal geometry with adjoint state computed on formulation (2.15).

2.5 Conclusion

The context of this chapter is the shape optimization of an elastic structure under sliding contacts where the contact terms are treated with the Nitsche method and the shape gradients are calculated using the adjoint state method.

In the previous chapter, we proposed an adjoint state discretization based on the discrete approximation of the optimization criterion. Unfortunately, this approach does not seem to be consistent although in practice it allows us to optimize elastic structures. The objective of this chapter was therefore to propose a more consistent discretization based on the Nitsche approximation of the continuous adjoint state. We have thus developed an a priori convergence analysis of our new approach in the case where the bi-active contact area $\Gamma_{C,b}$ is zero and under assumptions of convergence rate of the contact zones. We also explained how to slightly adapt the discretization method in order to relax these last assumptions while keeping a convergence result. Some numerical experiments were also presented to illustrate these convergence results.

We want now to focus on the industrial application that motivated this work: the shape optimization of an "airless" tyre. In this particular industrial application, other non linearities occur owing to the large solicitations of such a structure. In the next chapter, we illustrate our shape optimization procedure in large strain and its applications.

Chapter 3

Shape optimization in large deformations

Contents

3.1   Introduction

We saw in the previous chapter that under regularity assumptions, gradient descent directions exist in linear elasticity and a shape gradient formulation makes sense. We were able to reach optimality conditions using the linear elasticity model. In other words, assuming the geometry and material behaviors as linear, we were able to ensure the convergence analysis of the shape sensitivity. This was performed for a contact problem treated by Nitsche's method.

We recall at this step of the study that, in the two first chapters, we optimized the shape of an elastic load-bearing rolling structure. Actually, the studied structure is called "airless" tyre and is for instance described in [103, 89] and can be observed in Figure 1. In our study case, large deformations occur as the "airless" tyre must bear the load of the vehicle and so a significant quantity of deformation energy. A contact area occurs and must be large enough to transmit the different efforts between the tyre and the ground. While large strains and/or large rotations occur, the assumption from infinitesimal strain theory are invalidate and a more general framework must be taken into account: the finite strain theory. To establish the stress-strain relationship, we introduce hyperelastic laws providing models for the stress-strain behavior of a material (see [78]).

Our contribution consists in presenting geometric shape optimization with contact in the framework of the finite strain theory. In this chapter, we follow the approach of Cea's method leading to a Lagrangian formulation of the optimization problem, as in the first chapter for linear elasticity. To reach a shape gradient expression, it is much easier to follow this approach through the finite strain theory than the classical method of derivation. We introduce the mechanical problem with unilateral contact, approximated by Nitsche's method. We compare different elastic laws and show the limits of the small deformations assumptions while large deformations occur. We also introduce two strategies to deal with the uniformity criteria while the structure is rolling. The first strategy relies on the uniformity of the contact stress whereas the second strategy relies on the uniformity of the deflection of the structure. We show that the two strategies lead to competitive and complementary results.

The optimization procedure is very similar to the one introduced in the first chapter, only novelties according to large deformations will be presented here.

Contact or Signorini's conditions are more intricate conditions than Dirichlet and Neumann conditions. They lead to a highly non-linear problem classically set in terms of a variational inequality. In the framework of large deformation, no proof of well-posedness or differentiability exists for geometric shape optimization owing to the non regularity of the mechanical formulations. Yet we numerically test the performance of such an algorithm with various geometries and prove the pertinence of such an algorithm.

Classically, all the mechanical quantities will be described in their reference configuration. Let X be a point of Ω^0 (the domain representing the body in its reference configuration) and x its position in the deformed configuration. The Lagrangian description (or material coordinates) depicts the motion of a solid body from its reference to its deformed configuration. For an elastic body, some relations can be announced to link both configurations (see Figure 3.1).

Let $\Phi : \mathbb{R}_+ \times \Omega^0 \to \Omega^t$ be the deformation and $u : \mathbb{R}_+ \times \Omega^0 \to \Omega^t$ the displacement of X as

$$x = \Phi(X) = X + u(X).$$
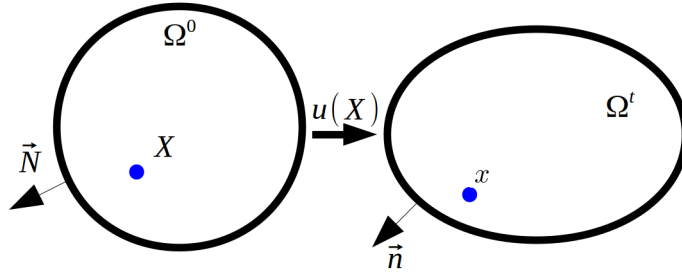
Figure 3.1: Deformation description of an elastic body.

We consider an "airless" tyre occupying in its reference configuration a domain $\Omega^0 \subset \mathbb{R}^d, d = 2$ or 3 that we want to optimize the shape, a representation being proposed in Figure 3.2. The reference boundary $\partial\Omega^0$ of the domain is split into three non-overlapping parts, Γ_N^0, Γ_C^0 and Γ_D^0. A Neumann condition is considered on Γ_N^0, representing holes in the "airless" tyre where a force density g_N^0 might be prescribed in case where pressure occurs. A contact with friction might occurs with a flat and horizontal rigid obstacle on the "airless" tyre tread Γ_C^0, and as a first approach, a homogeneous Dirichlet condition is prescribed on Γ_D^0, representing the tyre rim. In order to describe a more realistic behavior, a load on a rigid boundary will be set on the rim Γ_D^0 and will be depicted in section 3.4.1.
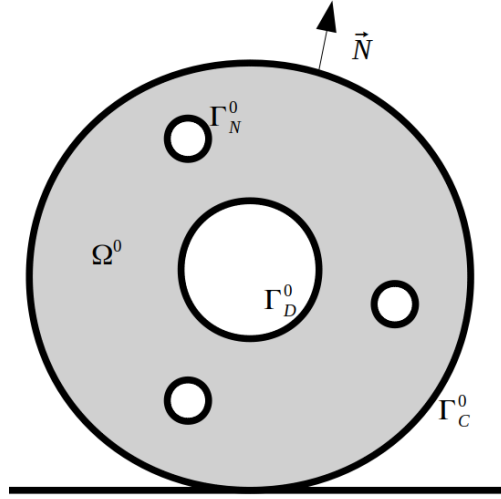
Figure 3.2: Schematic representation of Ω standing for an "airless" tyre and the rigid obstacle.

Let F be the deformation gradient as

$$F(u) = \nabla\Phi = I_d + \nabla u.$$

Let C be the Cauchy-Green deformation tensor defined as $C(u) = F^T(u)F(u)$. It denotes the evolution of local change in distances due to deformation. Let E be the Green-Lagrange deformation tensor defined as

$$E(u) = \frac{1}{2}(C(u) - I_d) = \frac{1}{2}(\nabla u + \nabla u^T + \nabla u^T \nabla u).$$

Classically we consider $\hat{\sigma}$ as the first Piola-Kirchhoff stress which reads

$$\hat{\sigma} = \det(F(u))\, \sigma F^{-T}(u), \tag{3.1}$$

where σ is the Cauchy stress tensor and $\hat{\hat{\sigma}}$ the second Piola-Kirchhoff stress defined as

$$\hat{\hat{\sigma}} = \det(F(u))F^{-1}(u)\sigma F^{-T}(u) = F^{-1}(u)\hat{\sigma}. \tag{3.2}$$

In case, as in chapter one, we consider a linear elastic constitutive law, the Cauchy stress tensor is linear related to the small deformation tensor by (1.2). Here, we consider an hyperelastic constitutive law defined by the strain energy density function W as

$$\hat{\hat{\sigma}}(u) = \frac{\partial W}{\partial E}(E(u)) = 2\frac{\partial W}{\partial C}(C(u)),$$

where the definition of W depends on the considered hyperelastic law, that we will precise later. Let dX be a infinitesimal vector around X. At the first order, it holds

$$x + dx = \Phi(X + dX) = \Phi(X) + F(u)dX,$$

which gives

$$\mathrm{d}x = \det(F)\mathrm{d}X.$$

The deformed outward unit vector n is linked to the reference outward unit vector N by the following relation: $n = \frac{F^{-T}(u)N}{\|F^{-T}(u)N\|}$. The displacement $u_\Omega : \Omega \to \mathbb{R}^d$ of the body according to its reference configuration is solution to the following elasticity problem:

$$\begin{cases} - \operatorname{div}\left(F(u_\Omega)\,\hat{\sigma}(u_\Omega)\right) = f^0 & \text{in } \Omega^0, \\ \hat{\sigma}(u_\Omega) \cdot N = g_N^0(u_\Omega) & \text{on } \Gamma_N^0, \\ u_\Omega = 0 & \text{on } \Gamma_D^0. \end{cases} \tag{3.3}$$

The "airless" tyre is solicited in large deformations. We wonder if it has a preponderant influence on the elastic shape optimization. We want to highlight the interest in hyperelastic law models in order to lead a shape optimization. The main contribution of this chapter is then the comparison of linear elastic and hyperelastic laws following the same procedure as in the first chapter concerning the shape optimization.

The present chapter is structured as follows. Section 3.2 is dedicated to the introduction of the frictional contact problem in large deformations and to a consistent formulation based on Nitsche's method. In section 3.3, the geometric shape optimization in the framework of large deformations is presented. In section 3.4, we introduce the discretization used and the optimization method. Finally, in section 3.5, we present some numerical results which highlight the interest of hyperelastic laws while large deformations occur and the efficiency of the criteria previously introduced to optimize an "airless" tyre.

3.2   Mechanical problem in large deformations

In this section, we introduce two hyperelastic laws and the unilateral contact condition with friction on the boundary Γ_C^0. We provide the weak formulation of the elastic unilateral problem for Nitsche's method in large deformations.

3.2.1   Hyperelastic material models

An elastic law aims at describing the mechanical and reversible behavior of a material and depends only on the deformation according to the reference configuration, i.e. a priori F. As any physical law, the following objectivity principle must be verified.

Principle 30 (Objectivity Principle). *The Cauchy stress vector must not depend on the orthonormal basis chosen to compute the Cauchy stress tensor from the elastic law.*

As a consequence, the Cauchy stress tensor only depends on the deformation tensor E or C. In case of hyperelastic laws, the stress-strain relationship derives from a strain energy

density function W (see [26, 40, 78]) as

$$\hat{\sigma}(u) = \frac{\partial W}{\partial E}(E(u)) = 2\frac{\partial W}{\partial C}(C(u)),$$

where the partial derivative is $\hat{\sigma}_{ij} = \frac{\partial W}{\partial E_{ij}}$. In the present part, the tensors will be described in a 3 dimensional framework ($d = 3$). Let γ_1, γ_2 and γ_3 be the principal stretches of a 3×3 matrix A. Invariants of a squared matrix A can be used to describe the strain energy density functions. It holds

$$i_1(A) = \mathrm{tr}(A) = \gamma_1 + \gamma_2 + \gamma_3,$$
$$i_2(A) = \frac{1}{2}((\mathrm{tr}(A))^2 - \mathrm{tr}(A^2)) = \gamma_1\gamma_2 + \gamma_2\gamma_3 + \gamma_3\gamma_1,$$
$$i_3(A) = \det(A) = \gamma_1\gamma_2\gamma_3,$$

where $\mathrm{tr}(A)$ and $\det(A)$ respectively denote the trace and the determinant of A. For an isotropic material, the strain energy density function depends on the invariants of the Cauchy-Green tensor C or equivalently of the Green-Lagrange tensor E, which means that the elastic law will be written as $W(i_1(C), i_2(C), i_3(C))$ or $W(i_1(E), i_2(E), i_3(E))$.

Saint-Venant–Kirchhoff model

The Saint-Venant–Kirchhoff model (see [13]) is the simplest hyperelastic model. It depicts an isotropic material whose law is linear. The strain energy density function reads

$$W(E(u)) = \frac{1}{2}\lambda(i_1(E(u)))^2 + \mu\, i_1(E(u)^2),$$

where λ and μ are still the Lamé material parameters, depending on the Young modulus and the Poisson ratio. The first Piola-Kirchhoff stress tensor (3.1) can then be rewritten using the invariants as

$$\hat{\sigma}(u) = \lambda i_1(E(u))I_d + 2\mu E(u).$$

That law is available while the deformation remains small enough. It can be used whether large rotations appear. Yet, another model must be used to take into account large deformations.

Remark 31. *The Saint-Venant–Kirchhoff model is an extension of the geometrically linear elasticity. The law is identical to the Hooke's law in linear elasticity*

$$\sigma(u) = \lambda i_1(\varepsilon(u))I_d + 2\mu\varepsilon(u).$$

where the deformation is linear $\varepsilon(u) = \frac{1}{2}(\nabla u + \nabla u^T)$. In the case of linear elasticity, the strain energy potential reads

$$W(\varepsilon(u)) = \frac{1}{2}\lambda(i_1(\varepsilon(u)))^2 + \mu\, i_1(\varepsilon(u)^2).$$

Mooney-Rivlin model

The Mooney-Rivlin model is mainly used for polymers and especially for rubber, as it is the case in this current study where we want to optimize the shape of an "airless" tyre. The law is isotropic and takes into account the incompressibility of the material. Mooney proposed first the model [73] in 1940 which was generalized by Rivlin in 1948 using the invariants [88]. For an incompressible Mooney-Rivlin material, the strain energy density function is

$$W(C(u)) = c_1(j_1(C(u)) - 3) + c_2(j_2(C(u)) - 3) + d_1(i_3(C(u))^{1/2} - 1)^2,$$

where c_1, c_2 are empirical material constants and d_1 is a penalization parameter for the incompressibility. $j_1(C)$ and $j_2(C)$ are some invariants defined as

$$j_1(C) = i_1(C) \ i_3(C)^{-1/3},$$
$$j_2(C) = i_2(C) \ i_3(C)^{-2/3}.$$

Remark 32. *While the material studied is incompressible, $\det(F(u)) = 1$ and the third invariant $i_3(C(u)) = 1$. If the material is considered as near-incompressible, $\det(F(u)) = i_3(C(u)) \simeq 1$.*

The Piola-Kirchhoff stress tensors (3.1) and (3.2) can then be rewritten using the invariants. We first need some derivative expressions as

$$\frac{\partial i_1}{\partial C}(C) = I_d,$$
$$\frac{\partial i_2}{\partial C}(C) = i_1(C)I_d - C^T,$$
$$\frac{\partial i_3}{\partial C}(C) = i_3(C)C^{-T},$$
$$\frac{\partial j_1}{\partial C}(C) = i_3(C)^{-1/3}(\frac{\partial i_1}{\partial C}(C) - \frac{i_1(C)}{3i_3(C)}\frac{\partial i_3}{\partial C}(C)),$$
$$\frac{\partial j_2}{\partial C}(C) = i_3(C)^{-2/3}(\frac{\partial i_2}{\partial C}(C) - \frac{2i_2(C)}{3i_3(C)}\frac{\partial i_3}{\partial C}(C)),$$

which leads to

$$\hat{\sigma}(u) = \frac{\partial W}{\partial E}(E) = 2\frac{\partial W}{\partial C}(C)$$
$$= 2c_1\frac{\partial j_1}{\partial C}(C) + 2c_2\frac{\partial j_2}{\partial C}(C) + 2d_1(1 - i_3(C)^{-1/2})\frac{\partial i_3}{\partial C}(C).$$

What's more, the second derivatives of the invariants with respect to the tensor C can be

expressed as

$$\frac{\partial^2 i_1}{\partial C^2}(C) = 0,$$

$$\frac{\partial^2 i_2}{\partial C^2}(C)_{ijkl} = \delta_{ij}\delta_{kl} - \delta_{il}\delta_{jk},$$

$$\frac{\partial^2 i_3}{\partial C^2}(C)_{ijkl} = i_3(C)(C_{ji}^{-1}C_{lk}^{-1} - C_{jk}^{-1}C_{li}^{-1}),$$

where δ_{kl} is the Kronecker delta and for the modified invariants $j_1(C)$ and $j_2(C)$, it holds

$$\begin{aligned}
\frac{\partial^2 j_1}{\partial C^2}(C)_{ijkl} = i_3(C)^{-1/3}\bigg(& \frac{4i_1(C)}{9i_3(C)^2}\frac{\partial i_3(C)}{\partial C}(C) \otimes \frac{\partial i_3}{\partial C}(C) \\
& - \frac{1}{3i_3(C)}\bigg(\frac{\partial i_3}{\partial C}(C) \otimes \frac{\partial i_1}{\partial C}(C) + \frac{\partial i_1}{\partial C}(C) \otimes \frac{\partial i_3(C)}{\partial C}(C)\bigg) \\
& - \frac{i_1(C)}{3i_3}\frac{\partial^2 i_3}{\partial C^2}(C)\bigg),
\end{aligned}$$

$$\begin{aligned}
\frac{\partial^2 j_2}{\partial C^2}(C)_{ijkl} = i_3(C)^{-2/3}\bigg(& \frac{\partial^2 i_2}{\partial C^2}(C) + \frac{10i_1(C)}{9i_3(C)^2}\frac{\partial i_3(C)}{\partial C}(C) \otimes \frac{\partial i_3}{\partial C}(C) \\
& - \frac{2}{3i_3(C)}\bigg(\frac{\partial i_3}{\partial C}(C) \otimes \frac{\partial i_2}{\partial C}(C) + \frac{\partial i_2}{\partial C}(C) \otimes \frac{\partial i_3(C)}{\partial C}(C)\bigg) \\
& - \frac{2i_2(C)}{3i_3}\frac{\partial^2 i_3}{\partial C^2}(C)\bigg).
\end{aligned}$$

For the sake of formulations in the optimization part, we also develop the second derivative of the strain energy density $W(C)$ as

$$\frac{\partial \hat{\sigma}}{\partial E}(E)_{ijkl} = \frac{\partial^2 W}{\partial E^2}(E)_{ijkl} = (\mathcal{E}_{ijkl} + \mathcal{E}_{jikl})/2,$$

where

$$\begin{aligned}
\mathcal{E} = {} & 4c_1\frac{\partial^2 j_1}{\partial C^2}(C) + 4c_2\frac{\partial^2 j_2}{\partial C^2}(C) \\
& + 4\,d_1\bigg((1 - i_3(C)^{-1/2})\frac{\partial^2 i_3}{\partial C^2}(C) + \frac{1}{2}i_3(C)^{-2/3}\frac{\partial i_3(C)}{\partial C}(C) \otimes \frac{\partial i_3}{\partial C}(C)\bigg).
\end{aligned}$$

3.2.2 Pressure term

The source and boundary terms are generally defined on the reference domain Ω^0 and independent on the displacement. A case must be specified: Pressure as a Neumann condition in large strain. If a pressure g_N is imposed on the Neumann boundary Γ_N in the deformed configuration of the domain, a density of force must be defined as

$$g_N(u) = -p^{hl}\,n,$$

where n is the outward vector in the deformed configuration and p^{hl} is the pressure magnitude imposed into the hole. The transformation between the reference and deformed domain leads to

$$g_N^0(u) = \det(F(u))\|F^{-T}(u)N\|g_N(u) = -p^{hl}\det(F(u))F^{-T}(u)N,$$

where $g_N^0(u)$ depends on u and N in its reference configuration.

3.2.3   Frictional unilateral contact condition

The obstacle is supposed to be rigid and flat. We consider N_y, the inward unit vector to the rigid obstacle and g the initial gap between the elastic body and the obstacle (see Figure 3.3). We note that in this special case, n_y is equal to N_y. The displacement $u : \Omega \to \mathbb{R}^d$, is decomposed on the contact boundary Γ_C^0 into its normal part $u_N = u \cdot N_y$ and its tangent part $u_T = (I_d - N_y \otimes N_y)u$ such that

$$u = u_N N_y + u_T.$$
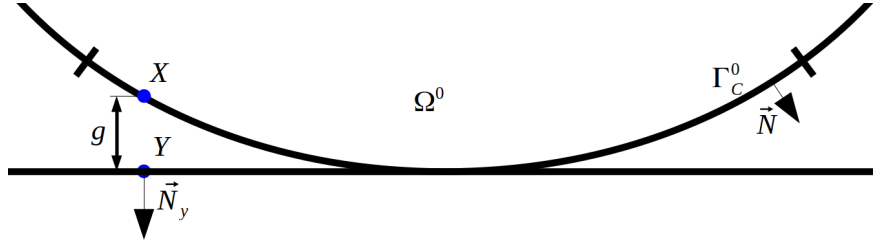
Figure 3.3: Contact surface representation for the vertical load configuration.

Two strategies can be developed to map a point X of Γ_C^0 on the obstacle at a point Y. The classic strategy consists in defining Y as the closest point projection of X onto the reference surface Γ_C^0, thereby depending on N_y. We refer for instance to [65] for more details. Another strategy consists in defining Y as the closest intersection of the contact surface with the line passing through point X and directed by N. This strategy, often called ray-tracing, can be found for instance in [84]. We choose to deal with the first strategy called projection as N_y is constant in this work (flat and rigid obstacle). The initial gap between the body and the obstacle is defined on $X \in \Gamma_C^0$ by

$$g = N_y \cdot (Y - X),$$

where Y is the orthogonal projection of X upon the rigid obstacle. We also note the decomposition of the Piola-Kirchhoff stress tensor on Γ_C^0 into normal and tangent parts:

$$\hat{\sigma}_N(u) = (\hat{\sigma}(u)N) \cdot N_y \text{ and } \hat{\sigma}_T(u) = (I_d - N_y \otimes N_y)(\hat{\sigma}(u)\,N).$$

The unilateral contact condition on Γ_C^0 can be expressed by the following complementary condition:

$$(u_N - g) \leq 0,$$
$$\hat{\sigma}_N(u) \leq 0,$$
$$(u_N - g)\,\hat{\sigma}_N(u) = 0.$$

The classical Coulomb law of friction can also be written on Γ_C^0, using the Piola-Kirchhoff stress tensors in large deformations, as

$$\begin{cases} |\hat{\sigma}_T(u)| \leq -\mathcal{F}\hat{\sigma}_N(u) & \text{if } \dot{u}_T = 0, \\ \hat{\sigma}_T(u) = \mathcal{F}\hat{\sigma}_N(u)\frac{\dot{u}_T}{|\dot{u}_T|} & \text{otherwise,} \end{cases}$$

where $\mathcal{F} \geq 0$ is the friction coefficient, depending on the couple of materials in contact (the tyre and the ground) and $\dot{u}_T$ is the sliding velocity. The Coulomb law of friction is usually approximated by replacing the sliding velocity by the following finite difference

$$\frac{u_T - u_T^0}{\Delta t},$$

where u_T^0 stands for the tangent displacement at an initial time step and Δt the time step. For the sake of simplicity, we take $u_T^0 = 0$ which leads to the so called static Coulomb's law of friction in large deformations:

$$\begin{cases} |\hat{\sigma}_T(u)| \leq -\mathcal{F}\hat{\sigma}_N(u) & \text{if } \dot{u}_T = 0, \\ \hat{\sigma}_T(u) = \mathcal{F}\hat{\sigma}_N(u)\frac{u_T}{|u_T|} & \text{otherwise.} \end{cases} \tag{3.5}$$

Using Green's formula on Problem (3.3), the displacement field $u_\Omega : \Omega \mapsto \mathbb{R}^d$ satisfies

$$\int_{\Omega^0} (F(u)\hat{\hat{\sigma}}(u)) : \nabla v \, dX - \int_{\Gamma_N^0} g_N^0(u) \cdot v \, ds(X)$$
$$- \int_{\Gamma_C^0} \hat{\sigma}(u)N \cdot v \, ds(X) = \int_{\Omega^0} f^0 \cdot v \, dX,$$

with, in addition, the condition $u = 0$ on Γ_D^0 and $\forall v : \Omega \mapsto \mathbb{R}^d$ sufficiently smooth with $v = 0$ on Γ_D^0.

3.2.4 A Nitsche-based weak formulation

The Nitsche method introduces a contact term which weakly prescribes the frictional contact conditions (3.4)-(3.5) in a consistent manner. We adapt the work of R. Mlika et al. in [71] where the Nitsche method is developed for bilateral contact to the unilateral contact studied

here. It is based on the equivalent reformulation of the contact conditions which has been originally derived from the augmented Lagrangian approach [3] and reads as

$$\hat{\sigma}_N(u) = -[\hat{\sigma}_N(u) - \gamma(u_N - g)]_-,$$
$$\hat{\sigma}_T(u) = P_{\mathcal{B}(N_y, \rho(u))}(\hat{\sigma}(u)N - \gamma u),$$

where $\rho(u) = \mathcal{F}[\hat{\sigma}_N(u) - \gamma(u_N - g)]_-$ is the friction threshold.

In case of unilateral contact, the Nitsche-based weak formulation in large deformation reads:

$$\begin{cases} \text{Find } u : \Omega \mapsto \mathbb{R}^d \text{ such that } u = 0 \text{ on } \Gamma_D^0, \\[2mm] \displaystyle\int_{\Omega^0} (F(u)\hat{\sigma}(u)) : \nabla v \, \mathrm{d}X - \int_{\Gamma_N^0} g_N^0(u) \cdot v \, \mathrm{d}s(X) + \mathcal{I}(u, v, N) = \int_{\Omega^0} f^0 \cdot v \, \mathrm{d}X, \\[2mm] \forall v : \Omega \mapsto \mathbb{R}^d \text{ sufficiently smooth with } v = 0 \text{ on } \Gamma_D^0, \end{cases} \qquad (3.6)$$

where the contact term $\mathcal{I}(u, v, N)$ satisfies

$$\begin{aligned} \mathcal{I}(u, v, N) = &-\int_{\Gamma_C^0} \frac{\theta}{\gamma} \hat{\sigma}(u)N \cdot \mathcal{D}_u \, \hat{\sigma}(u)N[v] \, \mathrm{d}s(X) \\ &- \int_{\Gamma_C^0} \frac{1}{\gamma} [\hat{\sigma}_N(u) + \gamma(u_N - g)]_- \, \mathcal{D}_u(\theta\hat{\sigma}_N(u) - \gamma(u_N - g))[v] \, \mathrm{d}s(X) \\ &+ \int_{\Gamma_C^0} \frac{1}{\gamma} P_{\mathcal{B}(N_y, \rho(u))}(\hat{\sigma}(u)N - \gamma u) \cdot \mathcal{D}_u(\theta\hat{\sigma}_T(u) - \gamma(u_T - g))[v] \, \mathrm{d}s(X). \end{aligned}$$

Remark 33. *We precise here that the aim of this chapter is to extend the optimization in large deformation. We present formal formulations in a continuous framework for the sake of simplicity.*

There exists no proof of the well-posedness for such formulation. Once again, only numerical tests led in [71] validate the Nitsche's method in large deformation where the influence of the contact parameter γ for different variants θ is numerically analyzed.

Remark 34. *Note that we can set the parameter θ to particular values that lead to different variants acting on the symmetry, skew-symmetry or non-symmetry of the contact term (see [25]). In particular, in the frictionless case, the formulation is symmetric when $\theta = 1$ and admits a potential energy. A classic method close to the penalization approach is recovered when $\theta = 0$. The tangent system involves the second order derivative of $\hat{\sigma}(u)N$, which encourages the use of this variant $\theta = 0$ for which the second order derivative does not appear. Finally, when $\theta = -1$, the contact term is skew-symmetric and leads to crucial properties for convergence independent of Nitsche's parameter.*

The directional derivative $\mathcal{D}_u \, \hat{\sigma}(u)N[v] = \mathcal{D}_u \, \hat{\sigma}(u)[v]N$ is detailed in the following proposition (see for instance [37]).

Proposition 35. *The directional derivatives of $F(u)$ and $E(u)$ are:*

$$\mathcal{D}_u\, F(u)[v] = \nabla v,$$
$$\mathcal{D}_u\, E(u)[v] = sym\,(F^T(u)\nabla v),$$

where $sym(\cdot)$ is the symmetric part of a second order tensor. The directional derivatives of $\hat{\overset{\circ}{\sigma}}$ and $\hat{\sigma}$ are:

$$\mathcal{D}_u\, \hat{\overset{\circ}{\sigma}}(u)[v] = \frac{\partial\,\hat{\overset{\circ}{\sigma}}}{\partial E}(u) : \frac{\partial E(u)}{\partial u}[v] = \frac{\partial^2 W}{\partial E^2}(E(u)) : sym\,(F^T(u)\nabla v),$$

$$\mathcal{D}_u\, \hat{\sigma}(u)[v] = \mathcal{D}_u\, F(u)\, \hat{\overset{\circ}{\sigma}}(u)[v] = F(u)\, \mathcal{D}_u\, \hat{\overset{\circ}{\sigma}}(u)[v] + \mathcal{D}_u\, F(u)[v]\, \hat{\overset{\circ}{\sigma}}(u)$$

$$= F(u)\left(\frac{\partial^2 W}{\partial E^2}(E(u)) : sym\,(F^T(u)\nabla v)\right) + \nabla v\, \hat{\overset{\circ}{\sigma}}(u).$$

3.3   Geometric shape optimization

In this section, we present the geometric shape optimization in the framework of the large strain theory. It aims at minimizing the energy of the structure $J(\Omega)$ that can be expressed as a target criterion to find the optimal shape. In case where a multi-criterion optimization is performed, the energy can be a combination of different criteria and lead to a multi-criterion optimization. The generic formulation for the energy or the target criterion is presented in its reference configuration as

$$J(\Omega) = \int_{\Omega^0} \mathcal{M}(u_\Omega)\, \mathrm{d}X + \int_{\partial\Omega^0} \mathcal{N}(u_\Omega)\, \mathrm{d}s(X), \tag{3.7}$$

where u_Ω is defined as the solution to (3.6).

Here, $\mathcal{M}$ and $\mathcal{N}$ are two functions assumed to be sufficiently smooth so that the shape derivative of J makes sense.

As in the previous chapters, we recall that the shape optimization consists then in finding some domains $\Omega \subset \Omega_{ad}$ minimizing the target criterion $J(\Omega)$ with a volume constraint.

3.3.1   Shape gradient formulation

We follow the same procedure as in chapter one, adapting the formulations to the finite strain theory.

Theorem 36. *Let $\Omega \in \mathscr{C}^2$ and assume that $f^0 \in H^1(\Omega; \mathbb{R}^d)$, $g_N^0 \in H^2(\Omega; \mathbb{R}^d)$ and that (3.6) admits a unique solution u_{Ω_t} sufficiently smooth for t small enough and $\Theta \in W^{1,\infty}(\mathbb{R}^d; \mathbb{R}^d)$. We denote $\mathcal{D}\, J(\Omega)[\Theta]$ the directional derivative of $J(\Omega)$ with respect to Ω in the direction*

$\Theta \in W^{1,\infty}(\mathbb{R}^d; \mathbb{R}^d)$, *we have when the derivative exists:*

$$
\begin{aligned}
\mathcal{D}\, J(\Omega)[\Theta] &= \int_{\Gamma_m^0} (\Theta \cdot N)\, (\mathcal{M}(u_\Omega) + F(u_\Omega)\frac{\partial W}{\partial E}(E(u_\Omega)) : \nabla p_\Omega - f^0(X) \cdot p_\Omega)\, \mathrm{d}s(X) \\
&+ \int_{\Gamma_m^0} (\Theta \cdot N)\, (\kappa_m \mathcal{N}(u_\Omega) + \nabla \mathcal{N}(u_\Omega) \cdot N)\, \mathrm{d}s(X) \\
&+ \int_{\Gamma_m^0 \cap \Gamma_N^0} (\Theta \cdot N)\, p^{hl}\mathrm{div}\,(\det(F(u_\Omega))F(u_\Omega)^{-T}p_\Omega)\, \mathrm{d}s(X),
\end{aligned}
$$

where Γ_m^0 *being a moving boundary of* Ω^0 *assuming* $\Gamma_m^0 \cap \Gamma_C^0 = \Gamma_m^0 \cap \Gamma_D^0 = \emptyset$ *(we recall that the only boundary* Γ_N^0 *is optimizable),* κ_m *is the mean curvature of* Γ_m^0*, and* $p_\Omega \in V$ *(where, in this chapter,* $V = \{v \in H^1(\Omega^0; \mathbb{R}^d) : v = 0 \text{ on } \Gamma_D^0\}$*) is the adjoint state defined as the solution,* $\forall q \in V$*, of*

$$
\begin{aligned}
&\int_{\Omega^0} \mathcal{D}_u(F(u_\Omega)\hat{\hat{\sigma}}(u_\Omega))[q] : \nabla p_\Omega\, \mathrm{d}X - \int_{\Gamma_N^0} \mathcal{D}_u\, g_N^0(u_\Omega)[q] \cdot p_\Omega\, \mathrm{d}X \\
&+ \mathcal{D}_u\, \mathcal{I}(u_\Omega, p_\Omega, N)[q] + \int_{\Omega^0} \mathcal{D}_u\, \mathcal{M}(u_\Omega)[q]\, \mathrm{d}X + \int_{\partial\Omega^0} \mathcal{D}_u\, \mathcal{N}(u_\Omega)[q]\, \mathrm{d}s(X) = 0.
\end{aligned}
\tag{3.8}
$$

We develop the method proposed by J. Céa [18] based on the Lagrangian formulation describing a constrained optimization problem. The method is described for instance by A. Maury in [69].

Proof of theorem (36)*:*
Céa's method consists in minimizing the criterion $J(\Omega)$ in (3.7) under the constraint that the weak formulation (3.6) is respected. Let $\mathcal{L}$ the Lagrangian application defined by

$$
\begin{aligned}
\mathcal{L}(u, v, N, \Omega) &= J(\Omega, u) \\
&+ \int_{\Omega^0} (F(u)\hat{\hat{\sigma}}(u)) : \nabla v \mathrm{d}X - \int_{\Gamma_N^0} g_N^0(u) \cdot v \mathrm{d}s(X) + \mathcal{I}(u, v, N) - \int_{\Omega^0} f^0 \cdot v \mathrm{d}X.
\end{aligned}
$$

where $J(\Omega, u) = \int_{\Omega^0} \mathcal{M}(u)\, \mathrm{d}X + \int_{\partial\Omega^0} \mathcal{N}(u)\, \mathrm{d}s(X)$. The key is to remark that $J(\Omega) = J(\Omega, u_\Omega)$ and then to identify $J(\Omega)$ as

$$
J(\Omega) = \mathcal{L}(u_\Omega, v, N, \Omega).
$$

If $\mathcal{L}$ is differentiated with respect to the domain Ω in the direction Θ, it gives according to each variable dependent on Ω

$$
\begin{aligned}
\mathcal{D}\, J(\Omega)[\Theta] &= \mathcal{D}\, [\mathcal{L}(u_\Omega, v, N, \Omega)]\, [\Theta] \\
&= \mathcal{D}_\Omega\, \mathcal{L}(u_\Omega, v, N, \Omega)[\Theta \cdot N] + \mathcal{D}_n\, \mathcal{L}(u_\Omega, v, N, \Omega)[\mathcal{D}_\Omega\, N[\Theta]] \\
&+ \mathcal{D}_u\, \mathcal{L}(u_\Omega, v, N, \Omega)[\mathcal{D}_\Omega\, u_\Omega[\Theta]].
\end{aligned}
\tag{3.9}
$$

Yet the shape derivative $\mathcal{D}_\Omega\, u_\Omega[\Theta]$ can not be calculted and the shape gradient is not explicit. In order to vanish the last term of equation (3.9) and obtain an computable formulation of the shape derivative of J, we follow the method proposed by J.-L. Lions in [66], often called the adjoint state method. Therefore, we introduce $p_\Omega \in V$ the adjoint state, assumed to be smoothed, as the solution of

$$\mathcal{D}_u\, \mathcal{L}(u_\Omega, p_\Omega, N, \Omega)[q] \; = 0, \; \forall q \in V.$$

Now, if we evaluate the equation (3.9) at $v = p_\Omega$, the last term vanishes and we show that

$$\mathcal{D}\, \mathcal{L}(u_\Omega, p_\Omega, N, \Omega)[\Theta] \; = \; \mathcal{D}_\Omega\, \mathcal{L}(u_\Omega, p_\Omega, N, \Omega)[\Theta \cdot N] + \mathcal{D}_n\, \mathcal{L}(u_\Omega, p_\Omega, N, \Omega)[\mathcal{D}_\Omega\, N[\Theta]],$$

as $\mathcal{D}_\Omega\, u[\Theta] \in V$. What's more, the term $\mathcal{D}_u\, \mathcal{L}(u, p, n, \Omega)[q]$ corresponds to the adjoint state problem and reads

$$\mathcal{D}_u\, \mathcal{L}(u, p, n, \Omega)[q] = \int_{\Omega^0} \mathcal{D}_u(F(u)\hat{\sigma}(u))[q] : \nabla p \; \mathrm{d}X$$
$$- \int_{\Gamma_N^0} \mathcal{D}_u\, g_N^0(u)[q] \cdot p \; \mathrm{d}X + \mathcal{D}_u\, \mathcal{I}(u, p, N)[q]$$
$$+ \int_{\Omega^0} \mathcal{D}_u\, \mathcal{M}(u)[q] \; \mathrm{d}X + \int_{\partial\Omega^0} \mathcal{D}_u\, \mathcal{N}(u)[q] \; \mathrm{d}s(X), \forall q \in V.$$

And so we have

$$\mathcal{D}\, J(\Omega)[\Theta] \; = \int_{\Gamma_m^0} (\Theta \cdot N) \left(\mathcal{M}(u_\Omega) + F(u_\Omega)\frac{\partial W}{\partial E}(E(u_\Omega)) : \nabla p_\Omega - f^0(X) \cdot p_\Omega\right) \mathrm{d}s(X)$$
$$+ \int_{\Gamma_m^0} (\Theta \cdot N) \left(\kappa_m \mathcal{N}(u_\Omega) + \nabla\mathcal{N}(u_\Omega) \cdot N\right) \mathrm{d}s(X)$$
$$- \int_{\Gamma_m^0 \cap \Gamma_N^0} (\Theta \cdot N) \left(\kappa_m p_\Omega \cdot g_N^0(u_\Omega) + \nabla(p_\Omega \cdot g_N^0(u_\Omega)) \cdot N\right) \mathrm{d}s(X)$$
$$- \int_{\Gamma_m^0 \cap \Gamma_N^0} \frac{\partial g_N^0 \cdot p_\Omega}{\partial N} \cdot N'(\Theta) \; \mathrm{d}s(X).$$

as $\Gamma_m^0 \cap \Gamma_C^0 = \emptyset$ and $\mathcal{I}(u, p, N)$ is an integral defined on Γ_C^0 and where $N'(\Theta) = -\nabla_T(\Theta \cdot N) = -\nabla(\Theta \cdot N) + (\Theta \cdot N)N$. We recall the following relation, if Ω is a closed and regular set of $\mathbb{R}^d$, $f \in W^{2,1}(\mathbb{R}^d, \mathbb{R}^d)$ and for all $\Theta \in W^{1,\infty}(\mathbb{R}^d, \mathbb{R}^d)$:

$$\int_{\Gamma^0} f \mathrm{div}_{\Gamma}\Theta \; \mathrm{d}s(X) = \int_{\Gamma^0} ((\Theta \cdot N)(f\kappa_m) - \nabla_T f \cdot \Theta) \; \mathrm{d}s(X),$$

where $\mathrm{div}_{\Gamma}\Theta = \mathrm{div}\,\Theta - \nabla(\Theta \cdot n) \cdot n$. This leads to the explicit expression of the shape

gradient in large deformations:

$$
\begin{aligned}
\mathcal{D}\, J(\Omega)[\Theta] \;=\; & \int_{\Gamma_m^0} (\Theta \cdot N)\,\Big(\mathcal{M}(u_\Omega) + F(u_\Omega)\frac{\partial W}{\partial E}(E(u_\Omega)) : \nabla p_\Omega - f^0(X)\cdot p_\Omega\Big)\,\mathrm{d}s(X) \\
& + \int_{\Gamma_m^0} (\Theta \cdot N)\,\big(\kappa_m \mathcal{N}(u_\Omega) + \nabla \mathcal{N}(u_\Omega)\cdot N\big)\,\mathrm{d}s(X) \\
& + \int_{\Gamma_m^0 \cap \Gamma_N^0} p^{hl}(\Theta \cdot N)\,\big(\kappa_m p_\Omega \cdot (\Phi(u_\Omega)N) + \nabla(p \cdot (\Phi(u_\Omega)N))\cdot N\big)\,\mathrm{d}s(X) \\
& - \int_{\Gamma_m^0 \cap \Gamma_N^0} p^{hl}\frac{\partial \Phi(u_\Omega)N \cdot p_\Omega}{\partial N}\cdot \nabla_T(\Theta \cdot N)\,\mathrm{d}s(X),
\end{aligned}
$$

with $\Phi(u) = \det(F(u))F^{-T}(u)$ that can be rewritten as

$$
\begin{aligned}
\mathcal{D}\, J(\Omega)[\Theta] \;=\; & \int_{\Gamma_m^0} (\Theta \cdot N)\,\Big(\mathcal{M}(u_\Omega) + F(u_\Omega)\frac{\partial W}{\partial E}(E(u_\Omega)) : \nabla p_\Omega - f^0(X)\cdot p\Big)\,\mathrm{d}s(X) \\
& + \int_{\Gamma_m^0} (\Theta \cdot N)\,\big(\kappa_m \mathcal{N}(u_\Omega) + \nabla \mathcal{N}(u_\Omega)\cdot N\big)\,\mathrm{d}s(X) \\
& + \int_{\Gamma_m^0 \cap \Gamma_N^0} (\Theta \cdot N)\,p^{hl}\mathrm{div}\,(\Phi(u_\Omega)p_\Omega)\,\mathrm{d}s(X).
\end{aligned}
$$

$\square$

3.3.2   Adjoint state formulation

In this section, we give explicit formulations of the directional derivatives proposed in the adjoint state equation (3.8).

Pressure term

The directional derivative of the pressure term (see Section 3.2.2) from (3.8) can be computed as follows

$$
\mathcal{D}_u\, g_N^0(u)[q] \cdot p = -p^{hl}\det(F(u))(((F^{-T}(u) : \nabla q)I_d - F^{-T}(u)\nabla q)F^{-T}(u)N)\cdot p,
$$

as $\mathcal{D}_u \det(F(u))[q] = \det(F(u))F^{-T}(u) : \nabla q$.

Contact term

In this section, we give an explicit formulation of the Nitsche's term and its directional derivative in the adjoint state equation. Recall that we have

$$\mathcal{I}(u, v, N) = -\int_{\Gamma_C^0} \frac{\theta}{\gamma} \hat{\sigma}(u)N \cdot \mathcal{D}_u \, \hat{\sigma}(u)N[v] \, \mathrm{d}s(X)$$

$$-\int_{\Gamma_C^0} \frac{1}{\gamma} [\hat{\sigma}_N(u) + \gamma(u_N - g)]_- \, \mathcal{D}_u(\theta \hat{\sigma}_N(u) - \gamma(u_N - g))[v] \, \mathrm{d}s(X)$$

$$+\int_{\Gamma_C^0} \frac{1}{\gamma} P_{\mathcal{B}(N_y, \rho)}(\hat{\sigma}(u)N - \gamma u) \cdot \mathcal{D}_u(\theta \hat{\sigma}_T(u) - \gamma(u_T - g))[v] \, \mathrm{d}s(X),$$

and $\rho(u) = -\mathcal{F}[\hat{\sigma}_N(u) - \gamma(u_N - g)]_-$.
The directional derivative $\mathcal{D}_u \mathcal{I}(u, p, N)[q]$ from (3.8) can be computed as follows

$$\mathcal{D}_u \mathcal{I}(u, p, n)[q] = -\int_{\Gamma_C^0} \frac{\theta}{\gamma} \mathcal{D}_u(\hat{\sigma}(u)N \cdot \mathcal{D}_u(\hat{\sigma}(u)N)[p])[q] \, \mathrm{d}s(X)$$

$$-\int_{\Gamma_C^0} \frac{1}{\gamma} \mathcal{D}_u \left([\hat{\sigma}_N(u) + \gamma(u_N - g)]_- \, (\theta \, \mathcal{D}_u \, \hat{\sigma}_N(u)[p] - \gamma p_n) \right)[q] \, \mathrm{d}s(X)$$

$$+\int_{\Gamma_C^0} \frac{1}{\gamma} \mathcal{D}_u \, P_{\mathcal{B}(N_y, \rho(u))}(\hat{\sigma}_T(u) - \gamma u_T) \cdot (\theta \, \mathcal{D}_u \, \hat{\sigma}_T(u)[p] - \gamma p_T)[q] \, \mathrm{d}s(X).$$

The adjoint state problem reads as follows

$$\begin{cases}
\text{Find } p_\Omega \in V \text{ such that } \forall q \in V \\[4pt]
\displaystyle\int_{\Omega^0} \mathcal{D}_u(F(u_\Omega)\hat{\sigma}(u_\Omega))[q] : \nabla p_\Omega \, \mathrm{d}X - \int_{\Gamma_N^0} \mathcal{D}_u \, g_N^0(u_\Omega)[q] \cdot p_\Omega \, \mathrm{d}X \\[10pt]
\displaystyle -\int_{\Gamma_C^0} \frac{\theta}{\gamma} \mathcal{D}_u(\hat{\sigma}(u_\Omega)N \cdot \mathcal{D}_u(\hat{\sigma}(u_\Omega)N)[p_\Omega])[q] \, \mathrm{d}s(X) \\[10pt]
\displaystyle -\int_{\Gamma_C^0} \frac{1}{\gamma} \mathcal{D}_u \left([\hat{\sigma}_N(u) + \gamma((u_\Omega)_N - g)]_- \, (\theta \, \mathcal{D}_u \, \hat{\sigma}_N(u_\Omega)[p_\Omega] - \gamma (p_\Omega)_N) \right)[q] \, \mathrm{d}s(X) \\[10pt]
\displaystyle +\int_{\Gamma_C^0} \frac{1}{\gamma} \mathcal{D}_u(P_{\mathcal{B}(N_y, \rho(u_\Omega))}(\hat{\sigma}_T(u_\Omega) - \gamma(u_\Omega)_T) \cdot (\theta \, \mathcal{D}_u \, \hat{\sigma}_T(u_\Omega)[p_\Omega] - \gamma (p_\Omega)_T))[p_\Omega] \, \mathrm{d}s(X) \\[10pt]
\displaystyle = -\int_{\Omega^0} \mathcal{D}_u \, \mathcal{M}(u_\Omega)[q] \, \mathrm{d}X - \int_{\partial\Omega^0} \mathcal{D}_u \, \mathcal{N}(u_\Omega)[q] \, \mathrm{d}s(X).
\end{cases}$$

What's more, the computation of $\mathcal{D}_u \, P_{\mathcal{B}(N_y, \rho(u))}((\gamma u))$ can be obtained thanks to the partial derivatives of the projection ball $P_{\mathcal{B}(N_y, \tau)}(q)$ according to q and τ. Indeed, we can find in [84] the following and useful estimates

$$\partial_q P_{\mathcal{B}(N, \tau)}(q) = \begin{cases}
0 & \text{for } \tau \leq 0, \\[4pt]
T_N & \text{if } |q_T| \leq \tau, \\[4pt]
\frac{\tau}{|q_T|}(T_N - \frac{q_T}{|q_T|} \otimes \frac{q_T}{|q_T|}) & \text{otherwise,}
\end{cases}$$

and

$$\partial_\tau P_{\mathcal{B}(N,\tau)}(q) = \begin{cases} 0 & \text{for } \tau \leq 0 \text{ or } |q_T| \leq \tau, \\ \frac{q_T}{|q_T|} & \text{otherwise.} \end{cases}$$

Here T_N is defined by $T_N = I_d - N \otimes N$, $q_T = T_N q$.

3.3.3   Criterion minimization

Minimization of the strain energy density

The most classical energy criterion concerns the energy density of elastic deformation and is defined as the strain energy density function W whose expression depends on the hyperelastic law:

$$J_e(\Omega, u_\Omega) = \int_{\Omega^0} W(E(u_\Omega)) \, \mathrm{d}X, \tag{3.10}$$

This objective functional can then be expressed in the general form (3.7) by considering

$$\mathcal{M}(u_\Omega) = W(E(u_\Omega)) \text{ and } \mathcal{N}(u_\Omega) = 0.$$

The directional derivative of the strain energy potential (3.10) from the adjoint state equation (3.8) can be computed as follows

$$\mathcal{D}_u J_e(\Omega, u_\Omega)[q] = \int_{\Omega^0} \mathcal{D}_u W(E(u))[q] \, \mathrm{d}x,$$

where

$$\mathcal{D}_u W(E(u))[q] = \frac{\partial W}{\partial E}(E(u)) : \frac{\partial E(u)}{\partial u}[q] = \hat{\sigma}(u) : sym(F^T(u)\nabla q).$$

Uniformity of the contact stress

The "airless" tyre must roll as uniformly as possible. It can be depicted through uniform criteria of optimization. An additional criterion developed in this chapter consists in uniforming the contact stress close to the contact boundary of the rolling structure according to the load positions. To this aim, we introduce the mean contact stress on the tyre tread or contact boundary Γ_C^0, through the expression of the first Piola-Kirchhoff stress tensor:

$$p_{mean}^0 = \frac{1}{N_l} \sum_{i=1}^{N_l} \hat{\sigma}(u_\Omega^i)N,$$

where N_l is the number of load positions (see section 1.4). We try to uniform the stress on the contact boundary according to the different load positions u_Ω^i

$$J_p(\Omega, u_\Omega, p_{mean}^0) = \frac{1}{2}\|\hat{\sigma}(u_\Omega)N - p_{mean}^0\|_{-1/2,\Gamma_C}^2. \tag{3.11}$$

As studied in the first chapter in linear elasticity, it is a good strategy to correctly uniform the contact stress. We follow the exact same approach as the uniformity of the contact stress using a $H^{-\frac{1}{2}}(\Gamma_C, \mathbb{R}^d)-$norm in section 1.3.3. The criterion for the uniformity of the contact stress reads

$$
\begin{aligned}
J_p(\Omega, u_\Omega, p^0_{mean}) &= \frac{1}{2}\|\hat{\sigma}(u_\Omega)N - p^0_{mean}\|^2_{-1/2,\Gamma_C} = \frac{1}{2}\|w_\Omega\|^2_{V_0} \\
&= \frac{1}{2}\int_\mathcal{B} \sigma(w_\Omega) : \varepsilon(w_\Omega)\ \mathrm{d}x = \frac{1}{2}\int_{\Gamma_C} g \cdot w_\Omega\ \mathrm{d}s(x) \\
&= \frac{1}{2}\int_{\Gamma^0_C} (\hat{\sigma}(u_\Omega)N - p^0_{mean}) \cdot w_\Omega\ \mathrm{d}s(X),
\end{aligned}
$$

where $w_\Omega = \omega[\sigma(u_\Omega)n - p^t_{mean}]$ is the solution to (1.29) for $g = \sigma(u_\Omega)n - p^t_{mean}$ with

$$
p^t_{mean} = \frac{1}{N_l}\sum_i^{N_l} \sigma(u^i_\Omega)n.
$$

We assume here that p^t_{mean} is known in advance so that it is constant according to the variable u_Ω and its derivative is equal to zero. Again, this criterion can be rewritten as the general functional form (3.7) by considering

$$
\mathcal{M}(u_\Omega) = 0 \text{ and } \mathcal{N}(u_\Omega) = \frac{1}{2}(\hat{\sigma}(u_\Omega)N - p^0_{mean}) \cdot w_\Omega.
$$

The directional derivative of the $H^{-1/2}(\Gamma^0_C, \mathbb{R}^d)$-norm criterion (3.11) from the adjoint state equation (3.8) can be computed as follows

$$
\begin{aligned}
\mathcal{D}_u J_p(\Omega, u_\Omega, p^0_{mean})[q] &= \frac{1}{2}\int_\mathcal{B} \mathcal{D}_u(\sigma(w_\Omega) : \varepsilon(w_\Omega))[q]\ \mathrm{d}x \\
&= \int_\mathcal{B} \sigma(w_\Omega) : \varepsilon(w[\mathcal{D}_u(\sigma(u)n)[q]])\ \mathrm{d}x \\
&= \int_{\Gamma^0_C} \mathcal{D}_u(\hat{\sigma}(u)N)[q] \cdot w_\Omega\ \mathrm{d}s(X),
\end{aligned}
$$

where $w[\mathcal{D}_u(\sigma(u)n)[q]]$ is defined as the solution to (1.29) for $g = \mathcal{D}_u(\sigma(u)n)[q]$ as proposed in the first chapter.

Remark 37. *The remark 8 still holds. The preference given here to the linear elasticity problem is guided by mechanical considerations and is faster solved than a formulation in large deformations, as the resolution is direct. Additionally, the deformations are small in the intermediary problem as the domain $\mathcal{B}$ does not contain holes in contrary to Ω.*

Uniformity of the deflection

Another strategy consists in uniforming the deflection on the Dirichlet boundary among all the load positions. It reads

$$J_d(\Omega, u_\Omega, d^0_{mean}) = \int_{\Gamma^0_D} \frac{E}{2h_T} (u_\Omega \cdot N_y - d^0_{mean})^2 \, \mathrm{d}s(X), \qquad (3.12)$$

where

$$d^0_{mean} = \frac{1}{N_l} \sum_{i=1}^{N_l} u^i_\Omega \cdot N_y.$$

This objective functional can then be expressed in the general form (3.7) by considering

$$\mathcal{M}(u_\Omega) = 0 \text{ and } \mathcal{N}(u_\Omega) = \frac{E}{2h_T}(u_\Omega \cdot N_y - d_{mean})^2.$$

The expression of the directional derivative of the deflection uniformity criterion (3.12) from the adjoint state equation (3.8) is rather straightforward and can be computed as follows

$$\mathcal{D}_u \, J_d(\Omega, u_\Omega, p_{mean})[q] = \int_{\Gamma^0_D} \frac{E}{h_T}(u_\Omega \cdot N_y - d_{mean})(q \cdot N_y) \, \mathrm{d}s(X).$$

Multi-criterion optimization

Finally, we will consider the following global energy

$$J(\Omega) = \sum_{i=1}^{N_l} J_g(\Omega_i, u^i_\Omega, p^0_{\text{mean}}, d^0_{\text{mean}}), \qquad (3.13)$$

where

$$J_g(\Omega_i, u^i_\Omega, p^0_{\text{mean}}, d^0_{\text{mean}}) = J_e(\Omega_i, u^i_\Omega) + \alpha J_p(\Omega_i, u^i_\Omega, p^0_{mean}) + \beta J_d(\Omega_i, u^i_\Omega, d^0_{mean}). \qquad (3.14)$$

3.4   Numerical strategy

In this section, we present the numerical strategy for the shape optimization. As the strategy is very similar with the one presented in the first chapter, section 1.4, we only present novelties according to the large strain framework.

3.4.1   Load condition on a rigid rim

In order to lead a more realistic mechanical load, we change the homogeneous Dirichlet condition to correctly depict the rigid rim supporting the "airless" tyre. To do so, the homogeneous Dirichlet condition on Γ_D is replaced by a rigid boundary condition that the rim only has a vertical rigid motion and is subject to a global load, standing for the vehicle weight. Denoting g_D^0 the prescribed load and α_D the unknown vertical rigid displacement on Γ_D^0, the weak formulation reads now: Find $u : \Omega \mapsto \mathbb{R}^d$, $\alpha_D \in \mathbb{R}$ and $\lambda_D \in H^{-1/2}(\Gamma_D)^d$ such that $\forall v : \Omega \mapsto \mathbb{R}^d, \forall \beta_D \in \mathbb{R}$ and $\forall \mu_D \in H^{-1/2}(\Gamma_D)^d$,

$$\int_{\Omega^0} (F(u)\hat{\sigma}(u)) : \nabla v \, \mathrm{d}X - \int_{\Gamma_N^0} g_N^0(u) \cdot v \, \mathrm{d}s(X) + \mathcal{I}(u,v,N) = \int_{\Omega^0} f^0(x) \cdot v \, \mathrm{d}X$$

$$+ \int_{\Gamma_D^0} (\lambda_D \cdot v + (u - \alpha_D N_y) \cdot \mu_D + (\lambda_D \cdot N_y - g_D^0)\beta_D) \, \mathrm{d}s(X),$$

where λ_D is a multiplier which represents the density of force on Γ_D^0 introduced to enforce the condition.

As a consequence, a new term appears in the adjoint state problem on Γ_D^0. We consider α_D and λ_D in the Lagrangian. It now reads $\forall q \in V, \forall q_{\alpha_D} \in \mathbb{R}$ and $\forall q_{\lambda_D} \in H^{1/2}(\Gamma_D)^d$,

$$\mathcal{D}_u \, \mathcal{L}(u, p, \alpha_D, \lambda_D, N, \Omega)[q] + \mathcal{D}_{\alpha_D} \, \mathcal{L}(u, p, \alpha_D, \lambda_D, N, \Omega)[q_{\alpha_D}]$$
$$+ \mathcal{D}_{\lambda_D} \, \mathcal{L}(u, p, \alpha_D, \lambda_D, N, \Omega)[q_{\lambda_D}] = 0,$$

which leads finally to find $p \in V, p_{\alpha_D} \in \mathbb{R}, p_{\lambda_D} \in H^{1/2}(\Gamma_D)^d$ such that $\forall q \in V, \forall q_{\alpha_D} \in \mathbb{R}$ and $\forall q_{\lambda_D} \in H^{1/2}(\Gamma_D)^d$,

$$\int_{\Omega^0} \mathcal{D}_u(F(u)\hat{\sigma}(u))[q] : \nabla p \, \mathrm{d}X - \int_{\Gamma_N^0} \mathcal{D}_u \, g_N^0(u)[q] \cdot p \, \mathrm{d}X + \mathcal{D}_u \mathcal{I}(u,p,N)[q]$$

$$+ \int_{\Omega^0} \mathcal{D}_u \, \mathcal{M}(u)[q] \, \mathrm{d}X + \int_{\partial\Omega^0} \mathcal{D}_u \, \mathcal{N}(u)[q] \, \mathrm{d}s(X)$$

$$= \int_{\Gamma_D^0} (p_{\lambda_D} \cdot q + (p - p_{\alpha_D} N_y) \cdot q_{\lambda_D} - p_{\lambda_D} \cdot N_y q_{\alpha_D}) \, \mathrm{d}s(X).$$

3.4.2   Gradient jump penalty

We only notice here that the stabilization term is slightly different than in linear elasticity:

$$G(u, v, N) = \sum_{E \in \mathcal{E}^k} \frac{1}{2} \int_{\partial T} \xi \gamma h_T^2 [\![\nabla u \cdot N]\!] \, [\![\nabla v \cdot N]\!] \, \mathrm{d}s(X).$$

where $\mathcal{E}^k$ denotes the set of edges (for $d = 2$) or faces (for $d = 3$) of the mesh having a non empty intersection with $\partial\Omega(k)$, $[\![\nabla u \cdot N]\!]$ denotes the inter-element gradient jump over

E, N is a unit normal vector to E and ξ is the penalization parameter. The same term is imposed on the adjoint state equation (3.8) and reads

$$\mathcal{D}_u\, G(u, p, N)[q] = \sum_{E \in \mathcal{E}^k} \frac{1}{2} \int_{\partial T} \xi \gamma h_T^2 \left[\!\left[\nabla q \cdot N \right]\!\right] \left[\!\left[\nabla p \cdot N \right]\!\right] \, \mathrm{d}s(X).$$
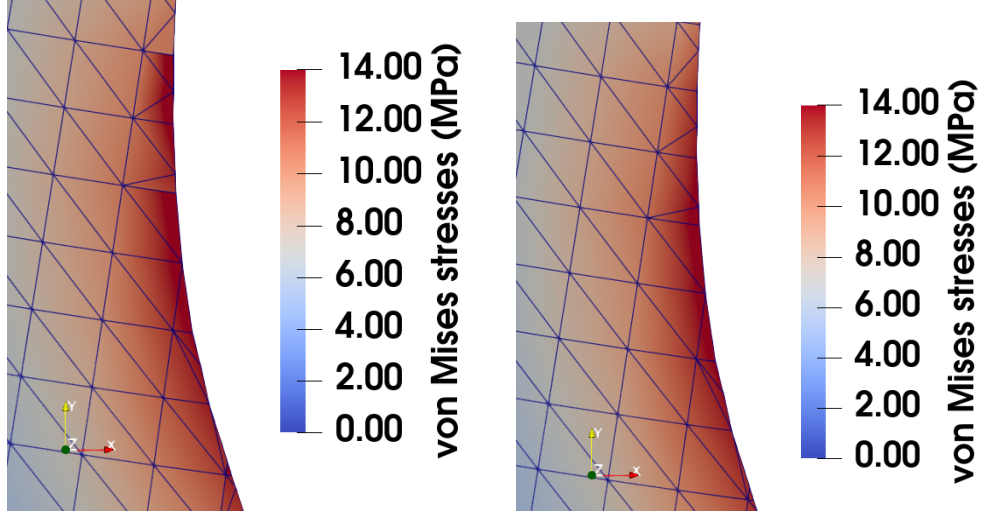
Figure 3.4: Focus on the von Mises stress of two solutions of the direct problem near a hole. On the left the gradient jump is not penalized to compute the solution ($\xi = 0$) and on the right the gradient jump is penalized ($\xi = 10^{-3}$).

As for the stress jump penalty in linear elasticity, a gradient jump penalty tends to recover a good approximation of the stress (here the von Mises stress in Figure 3.4) on elements largely cut by the frontier. Therefore, the following computations will be performed with a gradient jump penalty with $\xi = 10^{-3}$.

3.5 Numerical applications

In this section, we introduce numerical applications of the geometric shape optimization with contact. Different geometries will illustrate the performances of the presented shape optimization algorithm. The structure is supposed to be homogeneous and isotropic in the whole section. The purpose is successively to highlight the optimal shape differences for several elastic laws, then to emphasize the efficiency of the two criteria aiming at uniforming the rolling structure.

3.5.1 Geometries setting

We consider a ring with an inner radius $R_i = 20$ cm and an outer radius $R_e = 34$ cm. The ring width is set to $w_r = 22$ cm. The inner and outer radii are areas that can not be optimized. The Young modulus is set to 100 MPa and the Poisson ratio is 0.48. A contact might occur on boundary Γ_C upon the outer radius R_e (tyre tread) with a fictitious rigid body representing the ground. A load condition is set on the rigid boundary Γ_D upon the inner radius R_i (tyre rim). Concerning the Nitsche method, the contact parameter is set to $\gamma_0 = 100$ MPa and $\theta = -1$ to ensure an optimal convergence of the Newton-Raphson algorithm which is intricate in large deformations (see [71]). For the Mooney-Rivlin model, we use the following set of parameters $[c_1, c_2, d_1] = [\mu/3, \mu/6, \gamma_0]$.

First we compare three elastic laws on different topologies: linear elasticity, Saint-Venant – Kirchhoff model and Mooney-Rivlin model. Then, we show the influence of friction in the contact term and pressure into holes. Finally, we give some multi-criterion shape optimization results and we study the influence of the parameters α and β in (3.14).

3.5.2 Comparison of elastic laws

We first intend to minimize the strain energy potential W on the initial geometry proposed in Figure 3.5 and we compare different elastic models.

Figure 3.5: Initial geometry studied in the next sections with 108 initial holes.

The load is first supposed to be 100 kg, so that the deformation is low. Figure 3.6 shows that while the deformation is low, the optimal shape looks very similar whatever the elastic law considered.
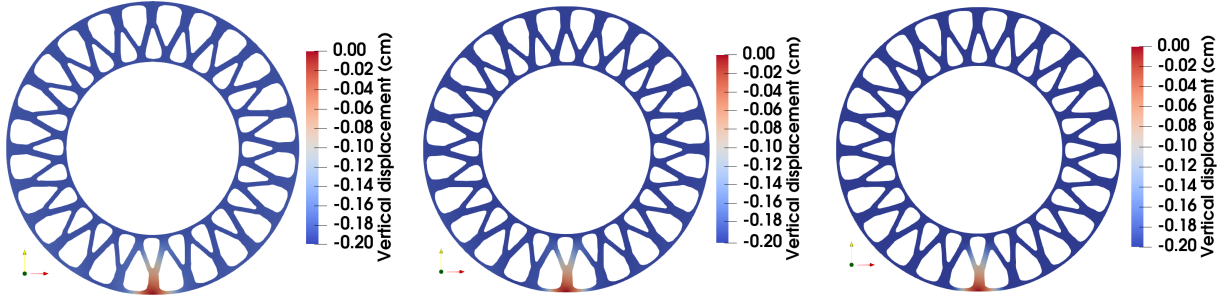
Figure 3.6: Optimal shapes. The load is set to 100 kg. Left to right: linear elasticity, Saint-Venant–Kirchhoff model and Mooney-Rivlin model.

The three elastic models show very close minimizations of the strain energy as presented in Figure 3.7, even though the linear elasticity already shows a light under estimate of the strain energy. Yet while small deformations occur, the three elastic models are almost equivalent leading to the same optimal shapes and so the linear elasticity model is sufficient to solve a shape optimization problem whereas considering hyperelastic models slows down the mechanical problem resolution.
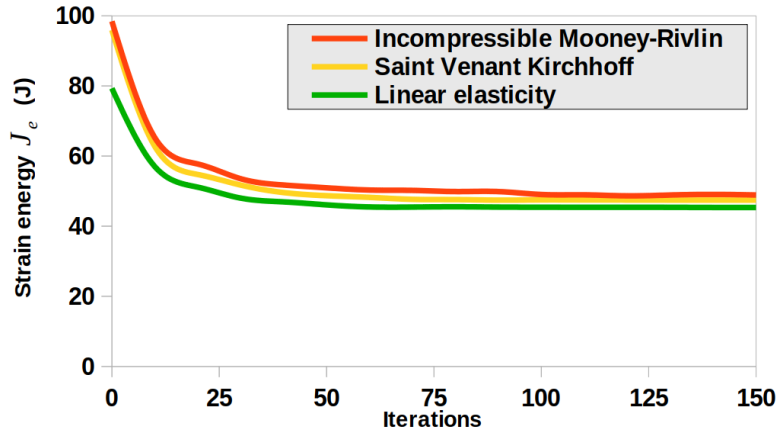
Figure 3.7: Minimization of the strain energy potential for the models exposed in Figure 3.6.

Nonetheless, an "airless" tyre must show better performances according to its bearing capacities and is largely solicited in large deformations. We set the load to 500 kg so that stronger mechanical solicitations occur and we compare the differences between the elastic laws. Figure 3.8 shows that the optimal shapes and mechanical behaviors differ according to the elastic model considered. More especially, the two hyperelastic models lead to very close optimal shapes and the difference largely comes from the linear elasticity model where the optimal shape differs. In addition, concerning the linear elasticity, we observe the same shape as the one obtained while the mechanical solicitation is low (see Figure 3.6). Regard-

ing the strain energy associated to each optimization test in Figure 3.9, we remark that the strain energy potential W differs according to the elastic law considered.

Figure 3.8: Optimal shapes. The load is set to 500 kg. Left to right: linear elasticity, Saint-Venant–Kirchhoff model and Mooney-Rivlin model.

Figure 3.9: Minimization of the strain energy J_e.

We then lead the same study on the initial geometry proposed in Figure 3.10 and we compare different elastic models.
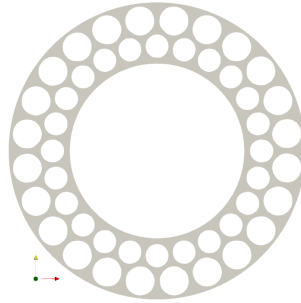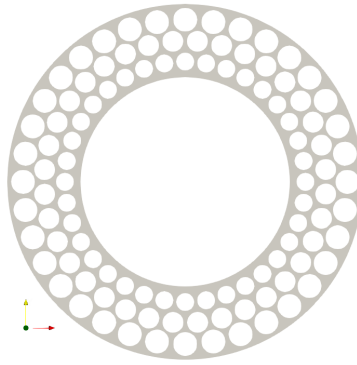
Figure 3.10: Initial geometry studied in the next sections with 108 initial holes.

Again, the load is first supposed to be 100 kg, so that the deformation is low. Figure 3.11 shows that the optimal shapes are very similar while the deformation is low, so as the strain energy evolution in Figure 3.12. And again, while the load is set to 500 kg, the optimal shapes differ according to the considered law as highlighted in Figure 3.13, so as the strain energy (see Figure 3.14). This is particularly the case for the linear elasticity.
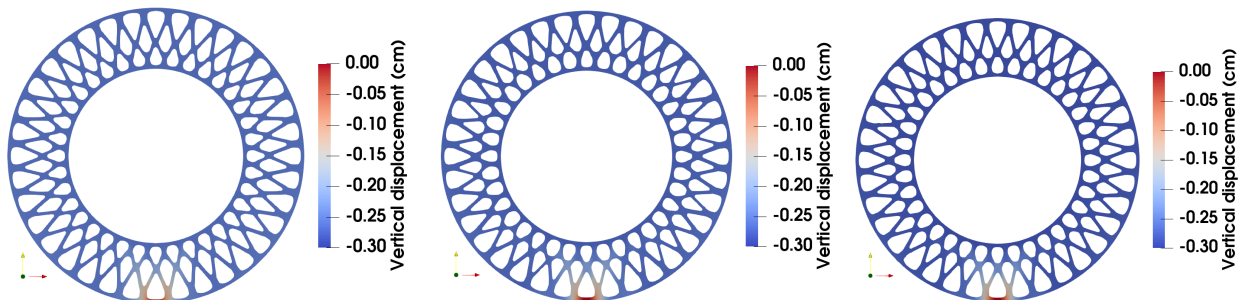
Figure 3.11: Optimal shapes. The load is set to 100 kg. Left to right: linear elasticity, Saint-Venant–Kirchhoff model and Mooney-Rivlin model.
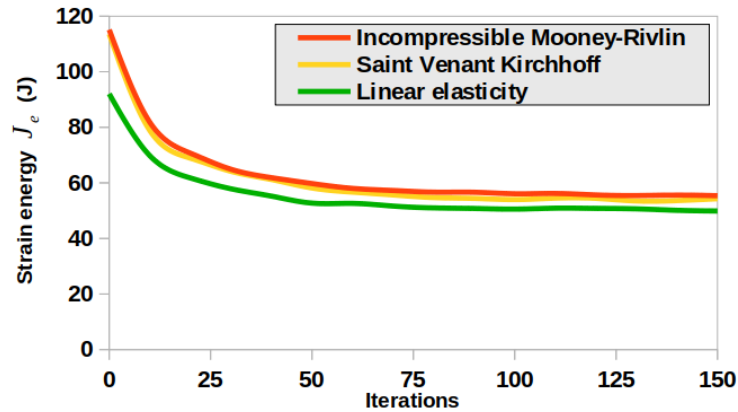
Figure 3.12: Minimization of the strain energy J_e for the models exposed in Figure 3.11.
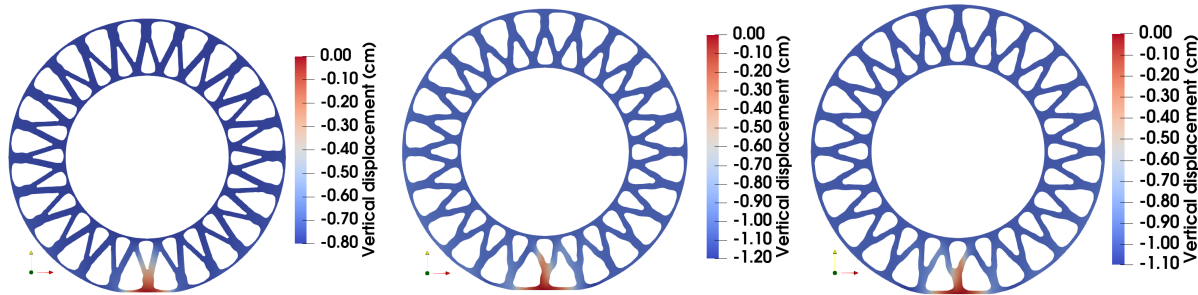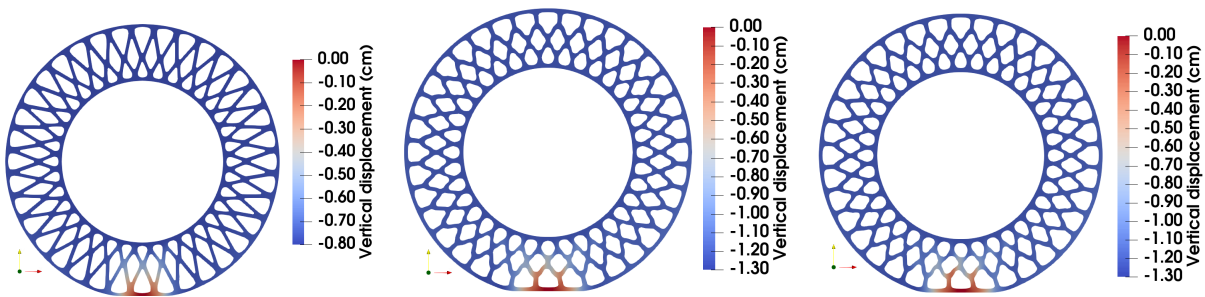

Figure 3.13: Optimal shapes. The load is set to 500 kg. Left to right: linear elasticity, Saint-Venant–Kirchhoff model and Mooney-Rivlin model.
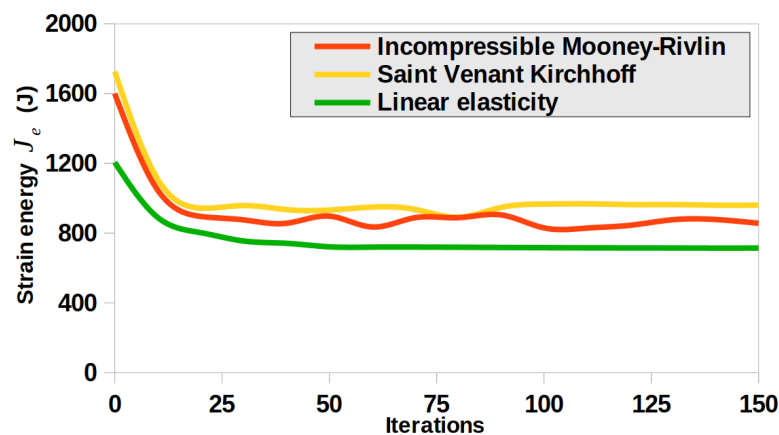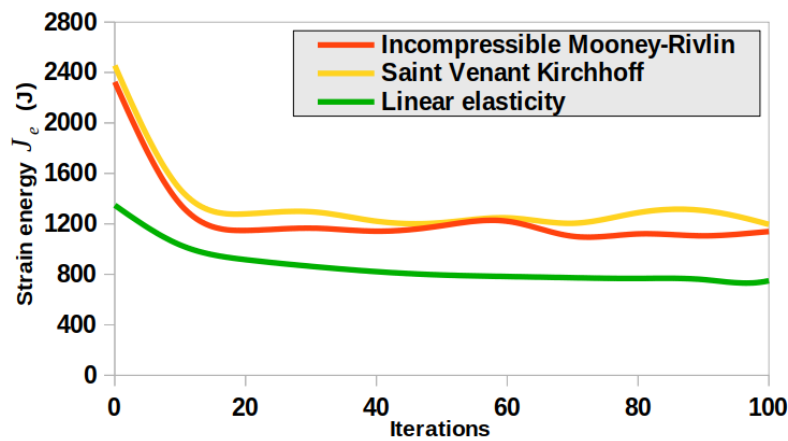

Figure 3.14: Minimization of the strain energy J_e for the models exposed in Figure 3.13.

What's more, if we try to apply the Mooney-Rivlin model on the optimal shape previously obtained with the linear elasticity model in Figure 3.13, we show that the mechanical behavior is a physical nonsense. A detachment appears in the contact between the tyre and the ground which is not convenient and the deformations are critical as presented in Figure 3.15.
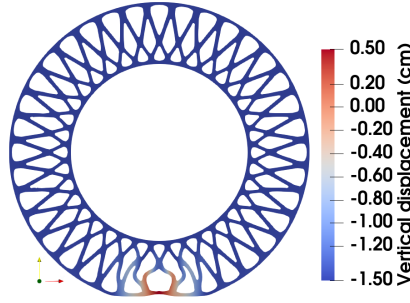
Figure 3.15: Deformations with Mooney-Rivlin model on the optimal shape previously obtained with the shape optimization led with linear elasticity in Figure 3.13.

We can already conclude the pertinence of hyperelastic laws for shape optimization. Even though the linear elasticity model is faster solved, it leads to inaccurate deformations and optimal shapes while large deformations occur. The Saint-Venant–Kirchhoff model and Mooney-Rivlin model show very close performances. This means that we only expose the geometric non linearity linked to the high rate of deformations and the material non linearity is not exposed. The Saint-Venant–Kirchhoff model can actually be unrealistic as nothing prevent the potential $\det(C)$ from being zero, leading to a total crushing of the material, or even worse to its reversal as observed in Figure 3.16.
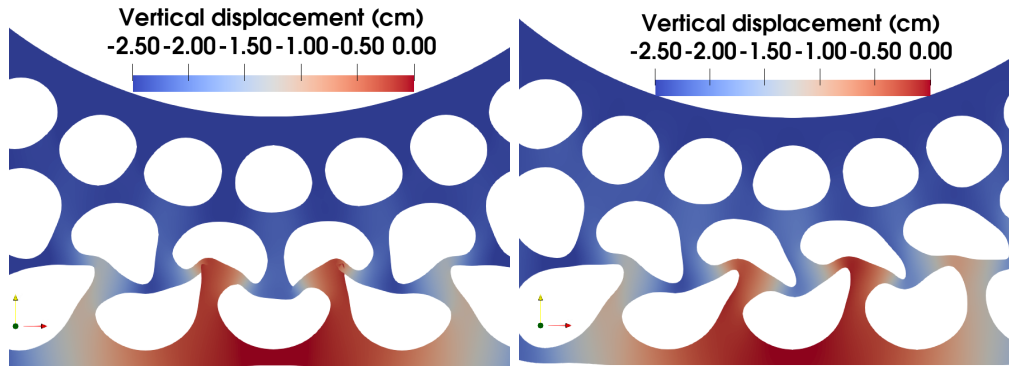
Figure 3.16: Focus on the contact zone for the initial shapes. On the left: Saint-Venant–Kirchhoff model and the reversal of the material and on the right: Mooney-Rivlin model.

The Saint-Venant–Kirchhoff model must be cautiously manipulated as it can lead to inaccurate material behaviors. Now if we optimize the shape of a more complex initial geometry in Figure 3.17, the optimal topologies can change according to the elastic model.
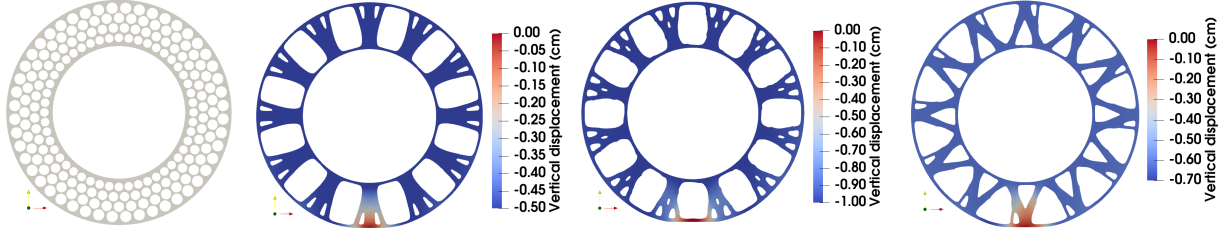
Figure 3.17: Shape optimization. Left to right: initial geometry set with 192 circular holes, linear elasticity, Saint-Venant–Kirchhoff model and Mooney-Rivlin model.

Two conclusions can be established: First the linear elasticity shows good performances while small deformations occur. Nevertheless, this simplified model shows limits while large strains occur and the optimization is inaccurate as the physical behavior of the structure is badly estimated. The Saint-Venant–Kirchhoff model can be unrealistic while large strains occur. A wise choice of the hyperelastic law must be done then. Secondly, the optimal geometry depends on the elastic law set. Finally, in order to lead an accurate shape optimization of the "airless tyre", we focus on both the material and geometry behaviors to select the Mooney-Rivlin model for the next experimental sections. For all the next optimizations, the load is set to 500 kg.

3.5.3   Multi-criterion optimization

Uniformization of the contact stress

We focus on the geometry initialized with 48 circular holes presented in Figure 3.5. We intend to minimize the criterion $J(\Omega)$ defined in (3.13) through three different tests where we respectively set $\alpha = 10$, $\alpha = 20$ and $\alpha = 50$ so that it aims at minimizing J_e and J_p ($\beta = 0$) with different weights. The optimal shapes are exposed in Figure 3.18. The criterion J_p actually tends to minimize the contact stress uniformity (see Figure 3.19) and the optimal shape differs from the optimization led with only J_e (see Figure 3.5). It is remarkable that the deformations are larger while J_p is implemented with a high weight ($\alpha = 50$) which shows that a compromise must be reached in order to minimize J_p without disturbing the minimization of J_e.
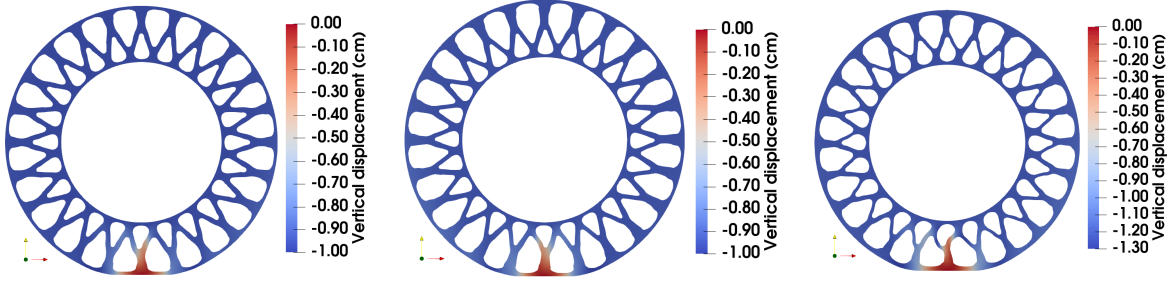
Figure 3.18: Optimal shapes with J_e and J_p. From left to right: optimal shape with $\alpha = 10$; $\alpha = 20$ and $\alpha = 50$.
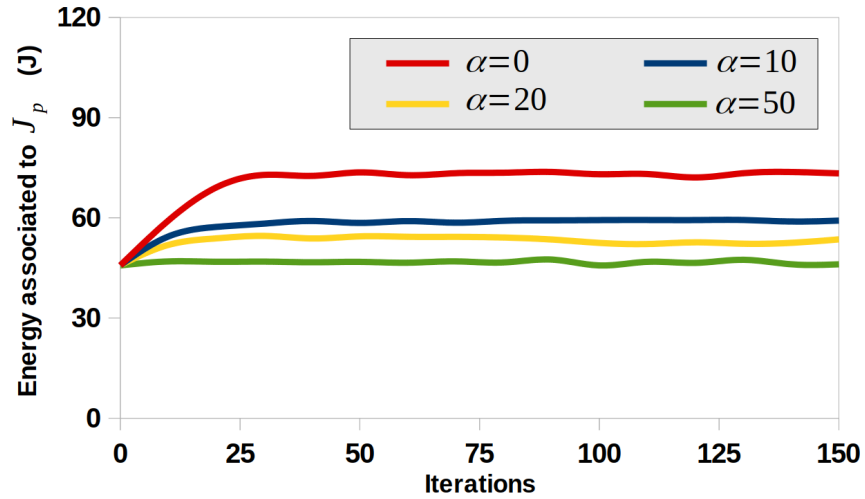
Figure 3.19: Minimization of the criterion J_p with different values of α.

Uniformization of the deflection

We perform a shape optimization where we intend to minimize the criterion $J(\Omega)$ defined in (3.13) where we successively set $\beta = 0.05$ and $\beta = 0.1$, so that Figure 3.20 shows the optimal shapes while we intend to minimize J_e and J_d ($\alpha = 0$).
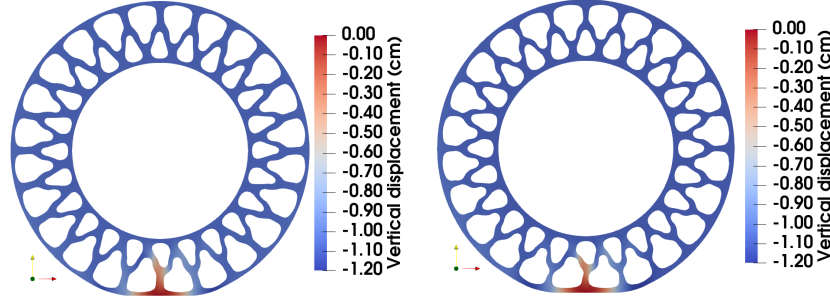
Figure 3.20: Optimal shapes with J_e and J_d. On the left: optimal shape with $\beta = 0.05$ and on the right: optimal shape with $\beta = 0.1$.

We calculate the standard deviation on all the deflections u_Ω^i in Table 3.1 so that

$$\sigma_{stdev} = \sqrt{\frac{1}{N_d} \sum_i^{N_d} (u_\Omega^i \cdot N - d_{mean})^2}.$$

We can conclude that the deflection uniformity criterion is efficient in the optimization process as we minimize the standard deviation of the deflection on all the load positions while J_d is set.

$\beta = 0$	$\beta = 0.05$	$\beta = 0.1$
0.0561	0.0497	0.0304

Table 3.1: Comparison of the standard deviations obtained in the shape optimizations according to the criterion weight β set.

Once again, the deformations are larger while J_d is implemented with a strong weight. A compromise must be reached in order to minimize J_d without disturbing the minimization of J_e.

Shape optimization with the three criteria

We now perform a shape optimization where we intend to minimize the criterion $J(\Omega)$ defined in (3.13) considering J_e, J_p and J_d. We set $[\alpha, \beta] = [10, 0.05]$ as a compromise to actually minimize the three criteria as exposed in Figure 3.21.
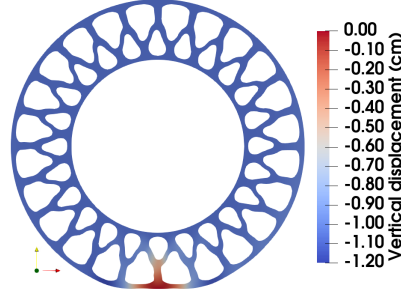
Figure 3.21: Optimal shape with J_e, J_p and J_d.

The three criteria don't necessary respectively lead to the same minimization directions and the same optimal shapes. Setting a multi-criterion optimization is a sensitive manipulation that can lead to a compromise in the criteria minimization (see Figure 3.22 and Table 3.2). Therefore a careful choice of the criteria weight must be observed.
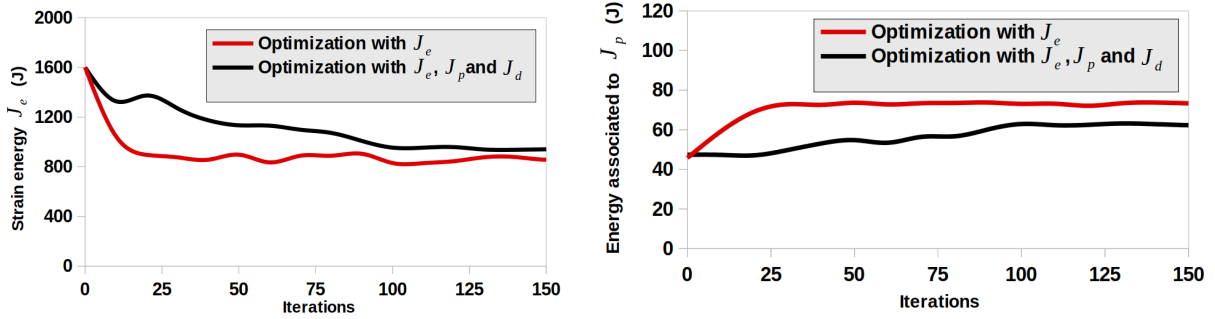
Figure 3.22: Evolution of the criteria. On the left: minimization of the strain energy J_e criterion and on the right: minimization of the contact stress uniformity criterion J_p.

$\alpha = 0$ and $\beta = 0$	$\alpha = 10$ and $\beta = 0.05$
0.0561	0.0481

Table 3.2: Comparison of the standard deviation deflection in the shape optimizations according to the criterion weights α and β.

Now if we lead a multi-criterion optimization on the geometry presented in Figure 3.10 with J_e, J_p and J_d , we see in Figure 3.23 that the different elastic models can lead to different optimal topologies.
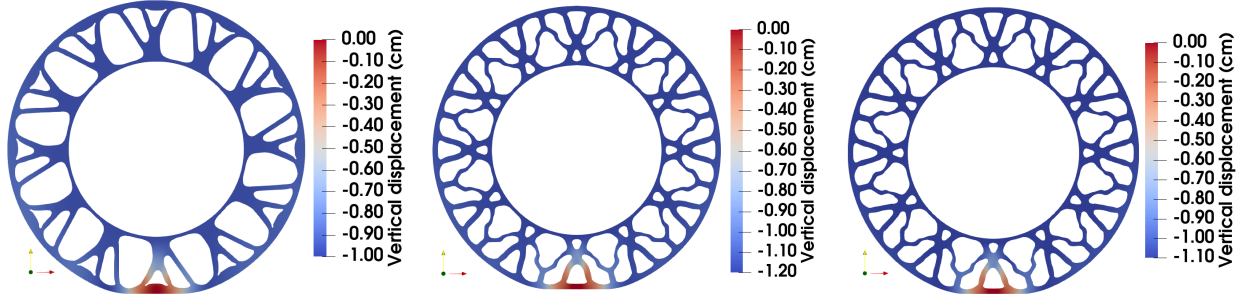
Figure 3.23: Shape optimization of the initial geometry with 108 holes (see Figure 3.10). Multi-criterion optimization J_e, J_p and J_d ($\alpha = 50$, $\beta = 0.005$). Left to right: linear elasticity, Saint-Venant–Kirchhoff model and Mooney-Rivlin model.

3.5.4   Physical parameters analysis

In this section, we perform two different shape optimizations on the previous initial configuration with 48 holes (see Figure 3.5). We first set pressure into the holes (see section 3.2.2) with $p^{hl} = 3$ bar. In a second time, we perform a shape optimization taking into account a frictional contact (see section 3.2.3) with $\mathcal{F} = 1$.
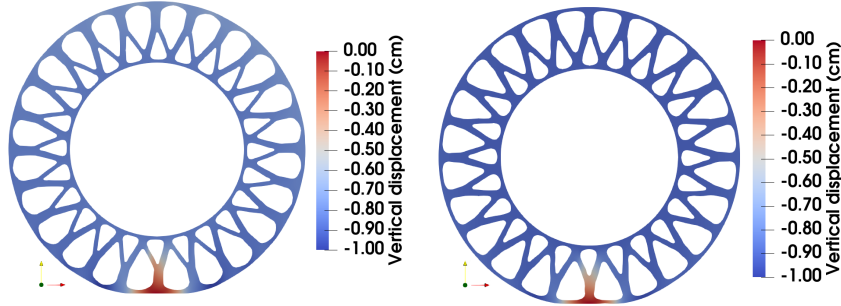
Figure 3.24: Optimal shapes. On the left: Shape optimization with pressure into the holes ($p^{hl} = 3$ bar) and on the right: Shape optimization with friction ($\mathcal{F} = 1$).

It is obvious that pressure and friction change the optimization as optimal shapes in Figure 3.24 are different than the one obtained with the Mooney-Rivlin model in Figure 3.8.

3.5.5   Shape optimization with a variable volume

We finally perform a shape optimization intending to minimize J_e and changing the volume constraint. Concerning the initial geometry with 48 holes (see Figure 3.5), the volume was forced to be close to 32% of matter amount for all the previous tests performed. First we force the evolution of the volume from 32% of matter to 26%. This leads to the increase of

the material deformation since the matter decreases. Second, we free the volume constraint but we force the mean deflection to be close to -1.2 cm on all the load positions, which causes a volume decrease and in the same time, the increase of the deformations in the material. The results can be observed in Figure 3.25.
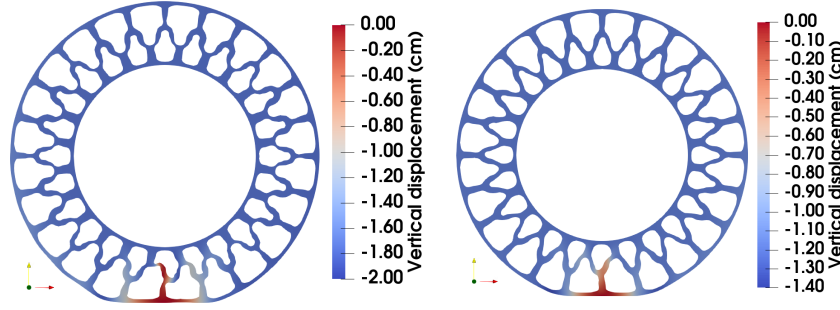
Figure 3.25: Optimal shapes with J_e. On the left: optimal shape with a target volume ratio of 26% and on the right: optimal shape with a target mean deflection of -1.2 cm.

3.5.6   More complex geometries

We aim at enlarging the numerical experiments with more complex initial geometries, as we know that shape optimization is largely dependent on the initial geometry. Different optimal shapes can be obtained from geometries where a multitude of small holes are initialized. We intend to minimize J_e, J_p and J_d on a geometry with 432 initial holes presented in Figure 3.26. The material characteristics are similar as the previous tests and we propose the Mooney-Rivlin model.
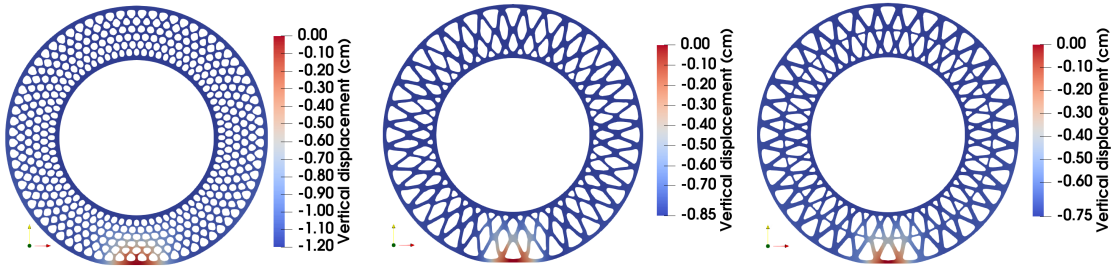
Figure 3.26: Shape optimization of a more complex geometry. From left to right: the initial geometry with 432 holes; optimal shape with J_e ($\alpha = \beta = 0$); optimal shape with J_e, J_p ($\alpha = 1$) and J_d ($\beta = 0.05$).

3.6   Conclusion

Shape optimization of an "airless" tyre requires the right choice of material behavior laws. Especially while large deformations occur, linear elasticity, which could be natural in a first model approximation as it is easy to be implemented, leads to inaccurate optimal shapes and bad estimates of deformations. Hyperelastic laws must be considered while high solicitations occur.

A multi-load strategy is determinant to illustrate the tyre rotation and leads, in this chapter, to the formulation of two criteria to uniform the structure. Both strategies are efficient and seem complementary but can be concurrent in the criteria minimization process. A sensitive choice of the criteria weights must be perform according to the wanted shape optimization and a compromise is unavoidable to satisfy the criteria optimization.

Conclusion and prospects

Shape optimization shows convincing results to improve mechanical structures and help industrial deciders in their designs. We saw that many results already exist concerning the optimization of an elastic linear structure with classical boundary conditions and through the small perturbations assumption. Nevertheless, our special study case, the "airless" tyre, operates in much more complex conditions. The non linearities introduced by the contact condition between the tyre and the ground, in addition to the large deformations that might occur while soliciting the tyre, involve some difficulties to solve the mechanical problem but also the shape optimization. Many questions were raised in that sense, especially according to the non differentiability of elements at stake. In this study, we decided to decompose the problem to progressively build the shape optimization responding to the initial need: optimize the shape of the "airless" tyre with contact in large deformations.

In the first chapter, we focus on a shape optimization algorithm, presenting a simple study case in linear elasticity. We introduce the contact condition with simple mathematical concerns, in order first to compare different approximation methods. That leads to emphasize the quality of Nitsche's method to deal with contact, the latter being used for the rest of the study. We also introduce the shape optimization process, describing the studied structure as a periodic object. The multi-load optimization is then proposed to optimize the tyre all around its rotation. We then compare different criteria. The first criterion, called the energy of elastic deformation, is present in the whole study as a crucial criterion in shape optimization. Yet, based on the multi-load optimization, a second criterion appears dealing with the uniformity of the contact stress. We pay a special attention to its mathematical formulation and compare different approaches to finally highlight the interest of a rigorous mathematical approach. That first chapter follows the Lagrangian approach to deal with shape optimization, also called the fast derivation where we did not focus on mathematical issues. This brings tricky questions about convergence owing to the non differentiability of the contact terms, which opens the second chapter.

Actually, the adjoint state of the Nitsche-based formulation introduced in the first chapter is not consistent. We want to focus on a different approach where we apply Nitsche's method to the adjoint state, which brings to a consistent formulation. In the second chapter, we mainly perform an a priori convergence analysis of the shape sensitivity of a contact problem approximated by a Nitsche-based finite element method. Indeed, due to the non-self-adjoint characteristic of Nitsche's method, especially the $\theta \neq 1$ variants, we study two different

approximations of the shape gradient. We prove that the second one is consistent and converges under reasonable assumptions, which we illustrate on a simple numerical example. An aspect on which our study could be extended is the case of a non-zero size grazing contact zone $\Gamma_{C,b}$. In this non-differentiable case, it would be interesting to extend the notion of shape gradient (2.10), possibly by a generalized shape gradient. It is then possible that the improved convergence result given in section 2.3.5 can be seen as the convergence towards an element of the generalized gradient. This would justify the use of the presented adapted method in case of non-zero size $\Gamma_{C,b}$. After having solved mathematical issues according to the shape gradient formulation in linear elasticity, we want to focus on the physical application that motivated this whole study. This leads to the third chapter.

In the third chapter, we care about the shape optimization in the finite strain framework. We first depict hyperelastic laws that model the mechanical behavior while elastic large deformations occur. We use a Nitsche-based formulation to deal with contact in large deformations. We also introduce the shape optimization process in case of large deformations. We follow the fast derivation method to formulate the shape gradient and the adjoint state problem, as in the first chapter, which is easier than the classical method. We adapt the process in the large deformations case and we derive new shape gradient and adjoint state formulations. Then numerical results highlight the interest in the hyperelastic laws to model the tyre mechanical behavior. We illustrate the efficiency of various criteria and the pertinence of our shape optimization algorithm for a multi-load and multi-criterion optimization, leading to relevant optimal shapes.

That third chapter leads to prospects that could extend our work and especially the optimization of the contact area. We could propose other criteria concerning the durability or the dynamic behavior. In addition, other physical phenomena could be taken into account, such as thermal solicitation as it is the case in the tyre behavior. We could also study the aerodynamic or hydrodynamic phenomena while the tyre rolls at high speed and formulate a multi-physics shape gradient in consequence. We could also study multi-material structures and intend to optimize different areas with different mechanical properties.

Appendices

Appendix A

Geometric representation

A.1   Introduction

Geometric shape optimization requires an efficient representation of the geometry to permit its evolution. Classical strategies consist in adapting the mesh to geometry at each optimization iteration according to the evolutions forced by the frontier variation method and so displace the boundary between matter and vacuum. Some methods arised in litterature to split the manipulation of the mesh and the geometry, in particular the level set method. This method was first presented in the shape optimization framework in [92] where an elastic problem is exposed with immersed interface methods, then in [80] that studied a Laplacian problem with two materials for matter and vacuum, and finally in [8] where an elastic problem is analysed and the shape gradient is formulated to reach descent directions. Some works deal then with the adaptation of the mesh according to the level set function (see the work of C. Dapogny et al. in [5, 6, 7]) to correctly approximate the mechanical problem. We present here how the level set method is treated on a polar grid and the different manipulations to ensure its regularity, in order to maintain the quality of the geometric evolution.

A.2   Level set method

Osher and Sethian introduced in [79] the level set method to describe the geometry and its evolutions. The first applications of the level set method were about geodesics, lithography, generation of minimal surfaces, propagation of flame fronts and fluid interfaces. This method is also efficient for shape optimization applications. The main idea developed by Osher and Sethian is to describe the boundaries of any structure by an implicit function. This method is indeed particularly efficient to compute fronts propagation and their evolutions. Let $\mathcal{D} \subset \mathbb{R}^d$ be a bounded domain in which the domain Ω is included. The representation of the domain

Ω in $\mathcal{D}$ might be expressed by a function ψ defined in $\mathcal{D}$ as:

$$\begin{cases} \psi(x) = 0 \text{ if } x \in \partial\Omega, \\ \psi(x) < 0 \text{ if } x \in \Omega, \\ \psi(x) > 0 \text{ otherwise.} \end{cases}$$

The interface between holes and matter is represented by a zero value of the level set function, which draws a curve whose value is set to 0 in a two-dimensional framework ($d = 2$) or a surface in a three dimensional framework ($d = 3$). This curve (respectively this surface) stands for the interface between the two regions and creates a clear boundary.

One way to represent the level set function ψ is to define the latter as a signed distance function according to the domain boundaries:

$$\psi(x) = \begin{cases} -d(x, \partial\Omega) & \text{if } x \in \Omega, \\ d(x, \partial\Omega) & \text{otherwise,} \end{cases}$$

where $d(x, \partial\Omega)$ is the distance between x and $\partial\Omega$.

Let a ring of minor radius R_i and of major radius R_e be the domain Ω illustrated in Figure A.1. Six holes are set through the ring as the optimization process only takes place at the interface of the different holes.
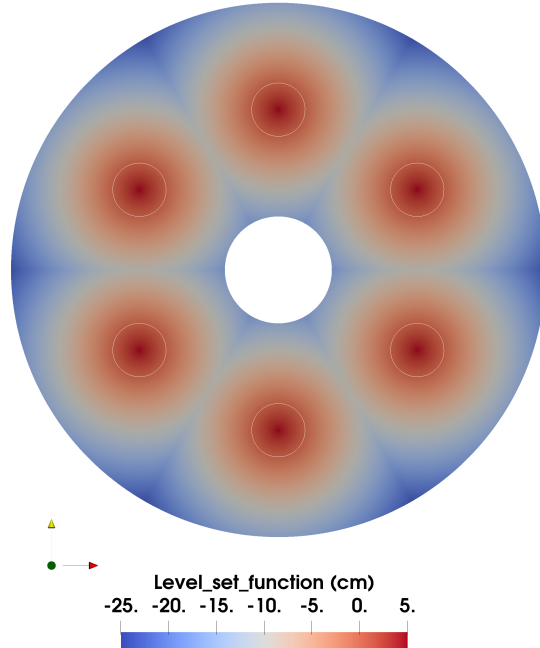
Figure A.1: Representation of domain $\Omega \subset \mathcal{D}$ by the level set function. The white curve stands for the 0-curve of the level set.

Remark 38. *In this work, we use a unique, structured and regular grid to build both the finite element method and the level set method, independently of the geometry. This is another advantage as a unique mesh is used for both usages and makes the computations faster. Indeed, the mesh does not need to adapt to the geometry changes at each optimization step. Only cut elemen for the mechanical computation must adapt at each iteration, which is much faster than a total remeshing.*

A.2.1 Algorithms for the level set function evolution

For each step, the domain Ω^k is represented by the function ψ^k. The crucial step consists of transporting the level set function ψ^k by the perturbed shape gradient G^k (see section 1.4). To do so, we solve the following transport equation

$$\begin{cases} \partial_t \varphi(x) & = -\tilde{G}^k \, |\nabla\varphi(x)|, \\ \varphi(0,x) & = \psi^k(x), \end{cases} \tag{A.1}$$

where we take $\psi^{k+1} = \varphi(\delta_k, x)$, for δ_k the descent step in the shape gradient algorithm. To numerically approximate this transport step, we develop in the next part the Sethian's schemes presented in [91] adapted to a polar grid for the sake of efficiency and simplicity.

Level set redistancing

After a few steps of transport, it is well-known that the level set properties can be deprecated. In particular, the function gradually moves away from a signed distance. In order to rectify this degradation, we classically apply some reinitialization steps (see for instance [104]), also based on Sethian's schemes. Thereby, the following system of equations is solved at each optimization iteration k:

$$\begin{cases} \varphi^{i+1}(x) = \varphi^i(x) + \delta_r S(\psi^k(x))(1 - |\nabla\varphi(x)|), \\ \varphi^0(x) = \psi^k(x), \end{cases} \tag{A.2}$$

for δ_r the step in the redistancing algorithm and where $S(\psi^k(x))$ stands for the sign of $\psi^k(x)$ in $\mathcal{D}$, ensuring that the redistancing of the level set does not impact the definition of the domain Ω^k. The number of iterations i and the descent step δ_r will be discussed in the further section A.3.3.

Level set smoothing

The level set redistancing tends to force the function ψ to look like a distance function, but does not prevent from sharp gradients of the function that might appear. Additionally, some

smoothing steps are also performed to avoid irregularities brought by the level set transport. It consists in finding, for each smoothing step j, the minimum of

$$E(\varphi^j(x)) = \int_{\mathcal{D}} \frac{1}{2}(\varphi^j(x) - \varphi^{j+1}(x))^2 \mathrm{d}x + \int_{\mathcal{D}} \frac{\delta_s}{2}|\nabla\varphi^j(x)|^2 \mathrm{d}x,$$

as proposed in [27] for example. The smoothing parameter δ_s must be wisely set to smooth the solution without disrupting it. The associated gradient of this cost function reads

$$E'(\varphi^j(x)) = \int_{\mathcal{D}} (\varphi^j(x) - \varphi^{j+1}(x))\mathrm{d}x + \int_{\mathcal{D}} \delta_s|\Delta\varphi^j(x)|\mathrm{d}x = \int_{\mathcal{D}} ((\varphi^j(x) - \varphi^{j+1}) + \delta_s|\Delta\varphi^j(x)|)\mathrm{d}x.$$

A minimum of E is reached when its gradient equals zero. It holds

$$E'(\varphi^j(x)) = 0 \Leftrightarrow \varphi^{j+1}(x) = \varphi^j(x) + \delta_s|\Delta\varphi^j(x)|, \tag{A.3}$$

where φ^{j+1} is the smoothed level set function of φ^j. Again, the number of iterations of j and the step δ_s will be discussed in the further section A.3.3. We then use the weak form associated to (A.3) and a classical Galerkin decomposition to obtain

$$(M(x) + \delta_s K(x))\varphi^j(x) = M(x)\varphi^{j+1}(x) \tag{A.4}$$

with

$$M_{yz}(x) = \int_{\mathcal{D}} \phi_y(x)\phi_z(x)\mathrm{d}x \text{ and } K_{yz}(x) = \int_{\mathcal{D}} \nabla\phi_y(x) \cdot \nabla\phi_z(x)\mathrm{d}x.$$

The method is close to the curvature effects explained for instance in [91] where the curvature is taken into account in the front propagation, which leads to a better representation of the level set evolution.

A.2.2   Computation of the mean curvature

We saw in the previous sections that, in order to compute the shape gradient, we need to estimate the mean curvature $\kappa_m = \mathrm{div}\, n$ on the optimizable frontier of Ω, where n is the outward unit vector of that same boundary. One of the main advantages of the level set representation is that it considerably eases the estimation of n and so of κ_m as $n = \frac{\nabla\psi(x)}{|\nabla\psi(x)|}$. Two methods lead to an estimation of k_m according to n. The first method is said to be explicit and consists of directly computing $\kappa_m = \mathrm{div}\, n$. The second method is said to be implicit and we use the same tools previously presented to smooth the level set function in order to compute the mean curvature since

$$\kappa_m = \frac{1}{\delta_s}((M(x) + \delta_s K(x))^{-1}M(x)\psi(x) - \psi(x))$$

where δ_s, $M(x)$ and $K(x)$ were presented in equation (A.4). Both methods are illustrated in Figure A.2. For the computation of the mean curvature κ_m in the optimization algorithm, we prefer the implicit calculation as it is much smoother and avoids irregularities.
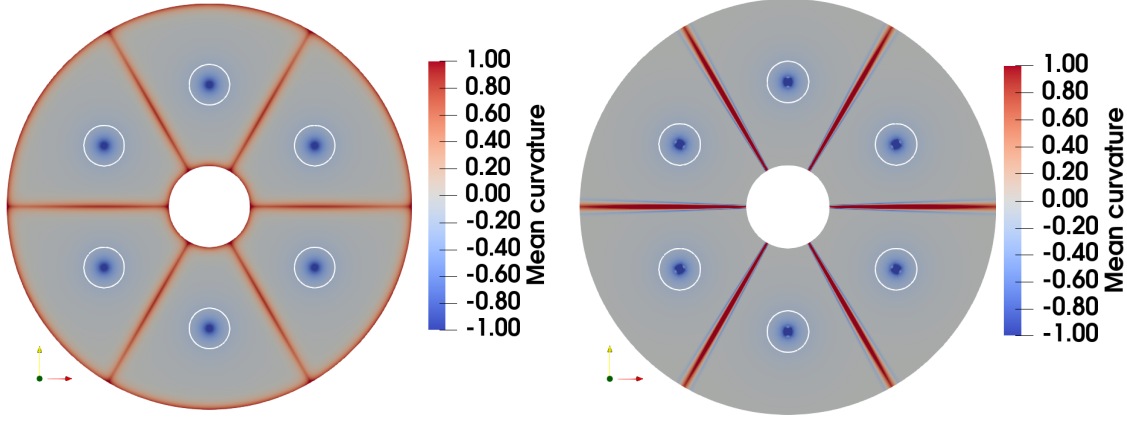
Figure A.2: Computation of the mean curvature on the domain previously initialized. On the left: the implicit representation and on the left: the explicit representation.

A.3   Numerical implementation

A.3.1   General schemes

In the previous section, the two equations expressed for the transport (A.1) and the redistancing (A.2) of the level set function might both be written as an Eikonal equation with a generic time step:

$$\partial_t \psi(x) - F(x) \left| \nabla \psi(x) \right| = 0.$$

Two parallel resolutions can be performed according to the expression of $F(x)$:

1. $F(x) = -\tilde{G}(x)$ the perturbed shape gradient in the transport case of the level set function in equation (A.1).

2. $F(x) = -S(\psi_0(x))(1 - \frac{1}{|\nabla \psi(x)|})$ in case of redistancing of the level set function corresponding to the equation (A.2).

The generic Hamilton-Jacobi equation is solved with the variable ψ which is always the level set function and F the generic function. Thereby, whatever the resolution led, the Sethian's first order schemes developed in [79] are used. The schemes are solved by finite differences.
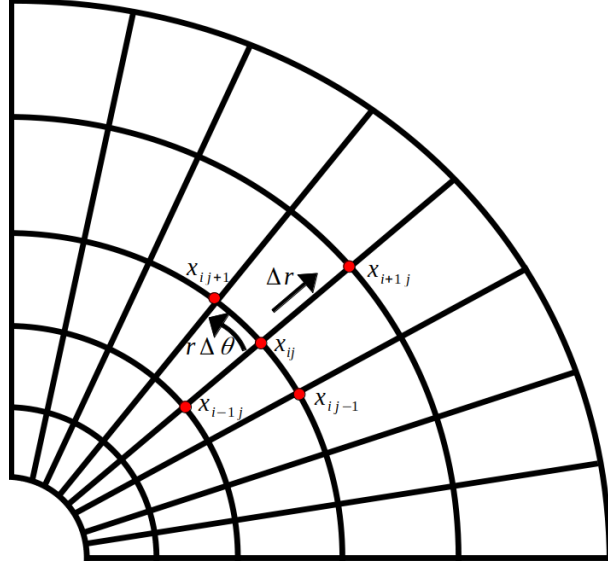
Figure A.3: Regular and polar mesh used both for the finite element and the level set methods.

The different schemes and equations are performed on a polar grid, as presented in Figure A.3. The two dimensional framework here is exposed although the three dimensional framework is straightforward. The Sethian's first order schemes read

$$\psi_{ij}^{n+1} = \psi_{ij}^n - \delta \mathcal{H}(x_{ij}, D_{ij}^{-r}\psi, D_{ij}^{+r}\psi, D_{ij}^{-\theta}\psi, D_{ij}^{+\theta}\psi),$$

where the Hamiltonian operator $\mathcal{H}\left(x_{ij}, D_{ij}^{-r}\psi, D_{ij}^{+r}\psi, D_{ij}^{-\theta}\psi, D_{ij}^{+\theta}\psi\right)$ is an approximation of $\mathcal{H}\left(x_{ij}, \nabla\psi(x_{ij})\right)$,

$$D_{ij}^{-r}\psi = \frac{\psi_{ij} - \psi_{i-1j}}{\Delta r} \ , \ D_{ij}^{+r}\psi = \frac{\psi_{i+1j} - \psi_{ij}}{\Delta r},$$

and

$$D_{ij}^{-\theta}\psi = \frac{\psi_{ij} - \psi_{ij-1}}{r\Delta\theta} \ , \ D_{ij}^{+\theta}\psi = \frac{\psi_{ij+1} - \psi_{ij}}{r\Delta\theta},$$

i and j are the indexes of the grid in the two dimensional framework. In our particular case, the equation might be solved as the advection equation thanks to an upwind first order scheme [82] as

$$\psi_{ij}^{n+1} = \psi_{ij}^n - \delta \left[F_{ij}^+ \nabla^+ \psi + F_{ij}^- \nabla^- \psi\right],$$

with $\nabla^- \psi$ and $\nabla^+ \psi$ as

$$\nabla_{ij}^{-}\psi = \Bigg(\max(\max(D_{ij}^{-r}\psi_{ij}, 0), -\min(D_{ij}^{+r}\psi_{ij}, 0))^2$$
$$+ \max(\max(D_{ij}^{-\theta}\psi_{ij}, 0), -\min(D_{ij}^{+\theta}\psi_{ij}, 0))^2 \Bigg)^{0.5},$$

and

$$\nabla_{ij}^{+}\psi = \Bigg(\max(\max(D_{ij}^{+r}\psi_{ij}, 0), -\min(D_{ij}^{-r}\psi_{ij}, 0))^2$$
$$+ \max(\max(D_{ij}^{+\theta}\psi_{ij}, 0), -\min(D_{ij}^{-\theta}\psi_{ij}, 0))^2 \Bigg)^{0.5},$$

with $F_{ij}^{+} = \max(F_{ij}, 0)$ and $F_{ij}^{-} = \min(F_{ij}, 0)$.

Remark 39. *The generic schemes are told to be upwind since the finite differences respect the propagation direction of the information concerning the level set evolution.*

These schemes are consistent (see [1] for the analysis). It is moreover monotonous if the Courant–Friedrichs–Lewy - also called CFL - condition (see [67]) is fulfilled, so that the information is spread a few less than an edge of the grid per step, i.e.

$$\sup_{ij}(F_{ij}) \frac{\delta}{\min(\Delta r, r\Delta\theta)} \leq 1,$$

and so the schemes converge.

A.3.2 Applications and results

A few tests have been led on the transport, the redistancing and the smoothing of the level set function in simple cases to show the effects of each treatment.

Transport results

Let G be the advection velocity (shape gradient) as defined in (A.1). We do not impose the redistancing and the smoothin of the level set in this unique section. As an example, G is set with a simple value to observe the level set transport and the 0-curve propagation:

$$\begin{cases} G(x) & = 1 \text{ if } \theta \in [0, \pi] \\ G(x) & = -1 \text{ otherwise.} \end{cases}$$
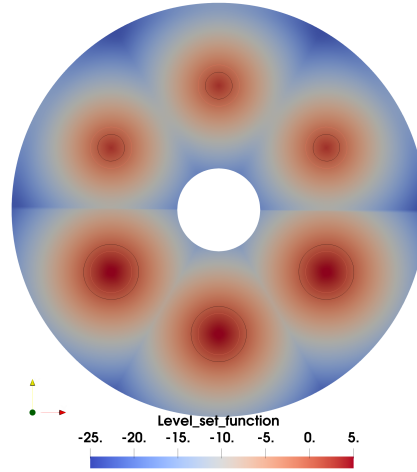
Figure A.4: Level set transport for a ring drilled in 6 positions after 10 iterations.

In Figure A.4, the white curve stands for the initial 0-curve of the level set whereas the black curve was transported and stands for the new level set 0-curve.

Redistancing results

To force the level set redistancing, we initialize the level set with a gradient higher than 1. The following domain in Figure A.5 shows a level set function whose gradient is set to $|\nabla\psi| = 1.5$.
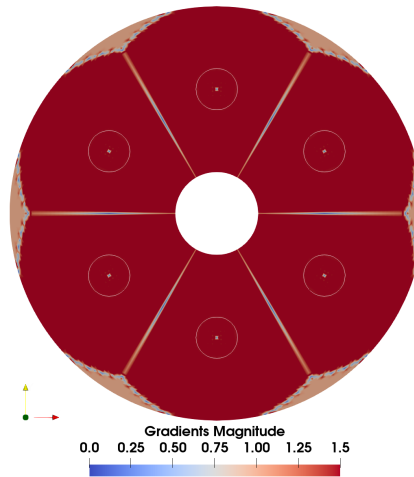
Figure A.5: Level set gradient for a ring drilled in 6 positions. $|\nabla\psi|$ is forced to 1.5 around the holes.

Then we initialize the redistancing of the level set function in Figure A.6.
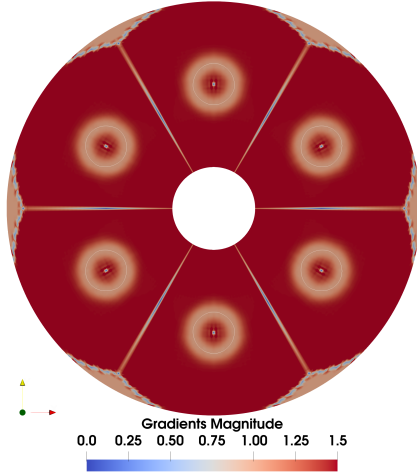
Figure A.6: Redistancing of the level set function. 200 iterations, redistancing step $\delta_r = h_T/100$.

A few observations might be done:

1. The redistancing of the level set function spreads from the 0-curve. This is an important property. Indeed, the evolution of the level set function starts from the sign change of the level set function, i.e. at the interface between matter and holes and the schemes used are upwind (see Remark 39). This is exactly where it is necessary to redistanciate the level set function in order to transport it later. It is then possible to locally redistanciate around this interface without treating the areas far away from the interface.

2. It is remarkable that a high number of iterations might slightly displace the 0-curve during the redistancing process, whereas this phenomenon is not beneficial. The generated displacement of the level set is yet smaller than a cell size, as values of the level set at nodes can not change of sign, and so the boundary displacement is limited. However, the redistancing should not displace the geometry boundaries. This implies to find out a good compromise between the time step and the number of iterations, to regularise the level set function without displacing the 0-curve, in a acceptable duration. That analysis is led in A.3.3.

Smoothing results

Redistancing results previously exposed do not prevent from local discontinuities of the level set gradient. A smoothing step might be implemented as proposed in section A.2.1 and the result is presented in Figure A.7.
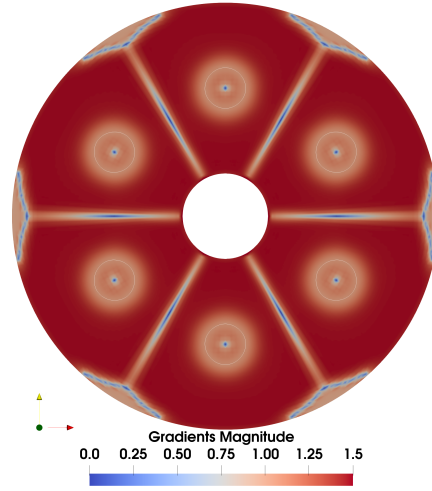
Figure A.7: Level set function redistanciated and smoothed. 200 iterations, redistancing step $\delta_r = h_T/100$ and smoothing step $\delta_s = h_T/200$.

It seems that the smoothing treatment tends to improve the redistancing effects around the 0-curve. What's more, the sharp gradients, previously observed at sector interfaces, have been smoothed. That smoothing process involves a higher processing time as a linear matrix system (A.4) must be solved, but worths it since the level set function is much more stable if regularised and smoothed at each optimization step. The solving time is calculed with the python function *process_time()* and the durations are presented in Table A.1.

	Process time (s)
Redistancing	146
Redistancing and smoothing	257

Table A.1: Solving time for the redistancing and the smoothing process computed by the python function *process_time()*. 30132 grid nodes. 200 iterations, redistancing step $\delta_r = h_T/100$ and smoothing step $\delta_s = h_T/200$.

The smoothing of the level set is however very deprecating as shown in Figure A.8: if the level set is too much smoothed, the 0-curve might move and thus change the geometry representation. The smoothing step is analysed in the following section A.3.3.
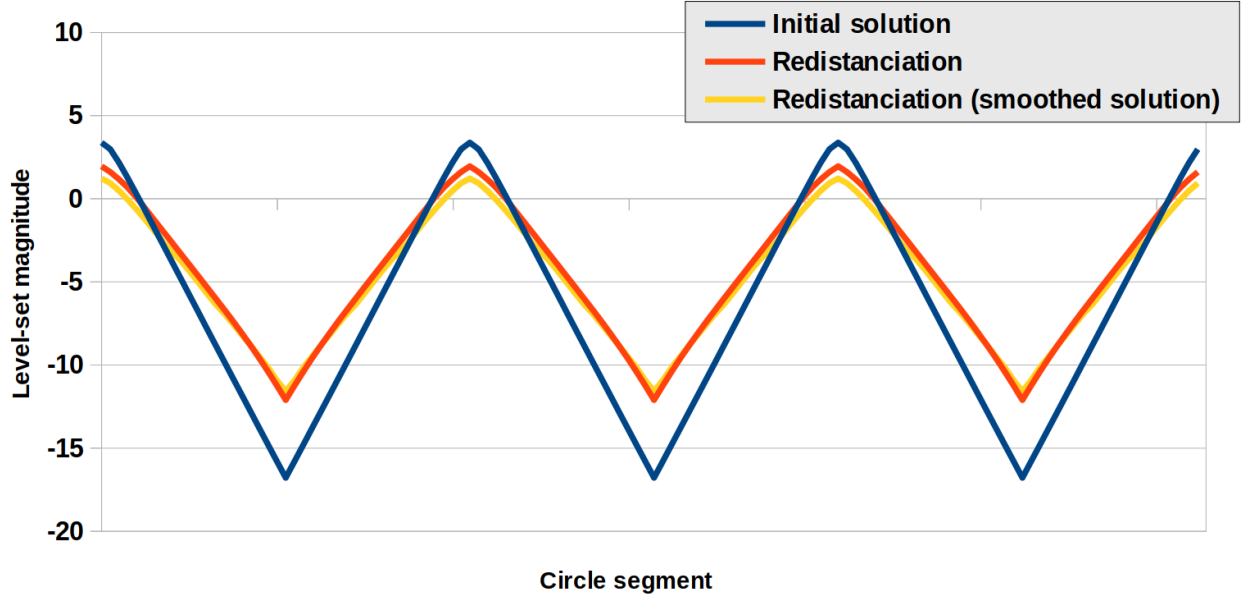
Figure A.8: Level set magnitude on the mean radius of the domain (right semi-circle segment crossing the hole centers).

A.3.3   Setting choice

The steps for the different treatments must be judiciously chosen to efficiently bring regularity on the level set function without disturbing it. As written previously, the 0-curve must not be displaced to accurately describe the geometry. Two tests are performed with the same geometry whose level set function gradient was initialized to $|\nabla\psi| = 1.5$. For the first test, the level set is only redistanced whereas for the second test, the level set is redistanced and smoothed.

Redistancing step

In Figure A.9, a zoom is performed on a unique hole to observe more precisely the level set gradient and the 0-curve behaviors. The bigger is the redistancing step, the more the 0-curves displaced are. On the other hand, the level set redistancing spreads if the redistancing step is high. For $\delta_r = h_T/200$, the redistancing is not significant enough to bring stability. The redistancing step $\delta_r = h_T/100$ seems sufficient. What's more, the 0-curve is slightly displaced. For $\delta_r = h_T/20$ and $\delta_r = h_T/50$ the redistancing process is too high as the accuracy on the 0-curve might be lost.
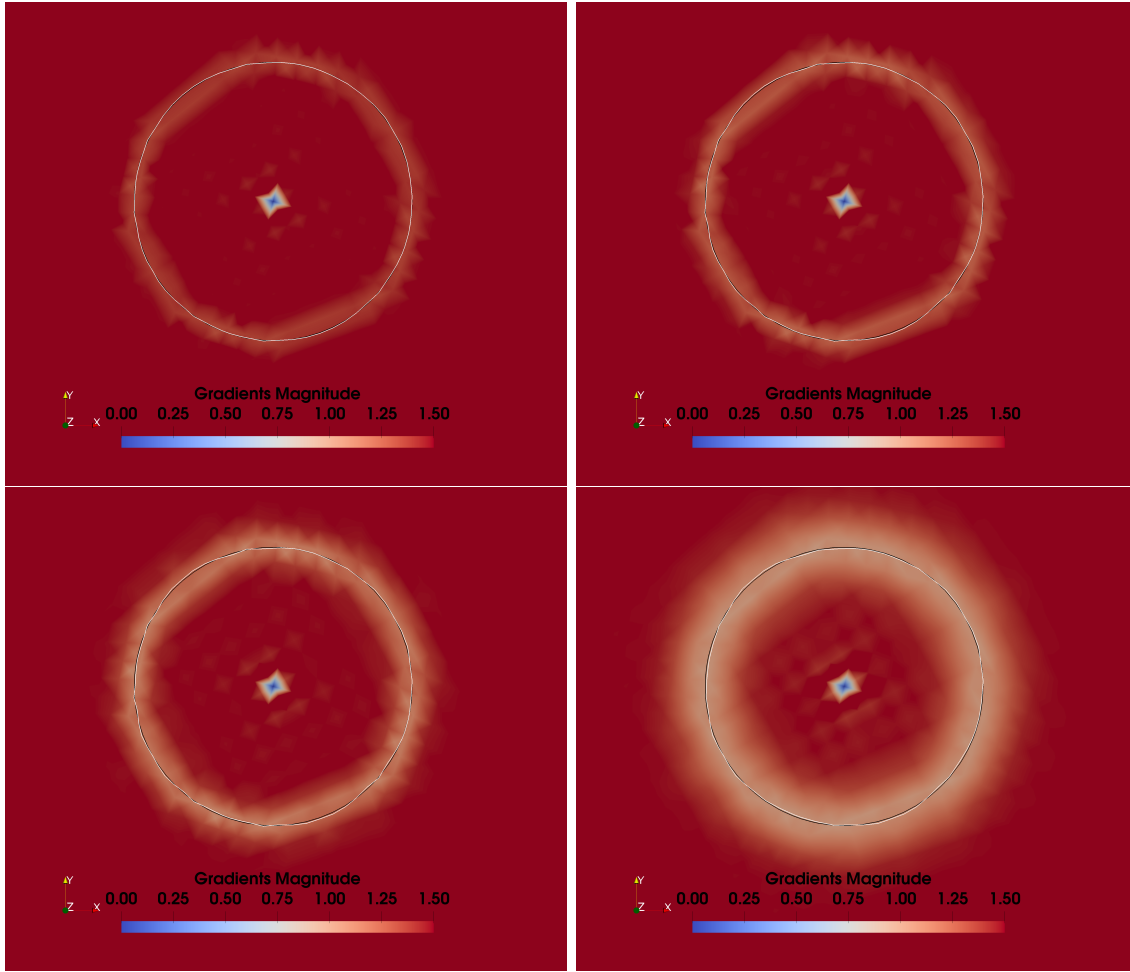
Figure A.9: Comparison of level set gradient according to the redistancing step on the level set function, 50 iterations. From top left to bottom right: the redistancing step is successively set to $\delta_r = [h_T/200, \ h_T/100, \ h_T/50 \text{ and } h_T/20]$. The black curve stands for the initial 0-curve whereas the white curve is the 0-curve of the redistanced level set function.

Smoothing step

The same test is performed but that time with the smoothing step. 50 iterations are performed on the redistancing and the smoothing algorithm with different smoothing steps according to the mesh size h. The redistancing step is fixed to $\delta_r = h_T/100$.

In Figure A.10, the smoothing process tends to spread the redistancing as previously expected. However, if the smoothing step is too high, the algorithm displaces the 0-curve of the level set function which is strongly inappropriate, as the representation of the geometry changes. For $\delta_s = h_T/100$, the 0-curve is too displaced. For $\delta_s = h_T/1000$, the smoothing step does not visually affect the level set gradient. A smoothing step set to $\delta_s = h_T/500$ is

more appropriate. Below this value, the smoothing process does not significantly affect the treatment on the level set function. Above this value, the smoothing displaces the 0-curve.
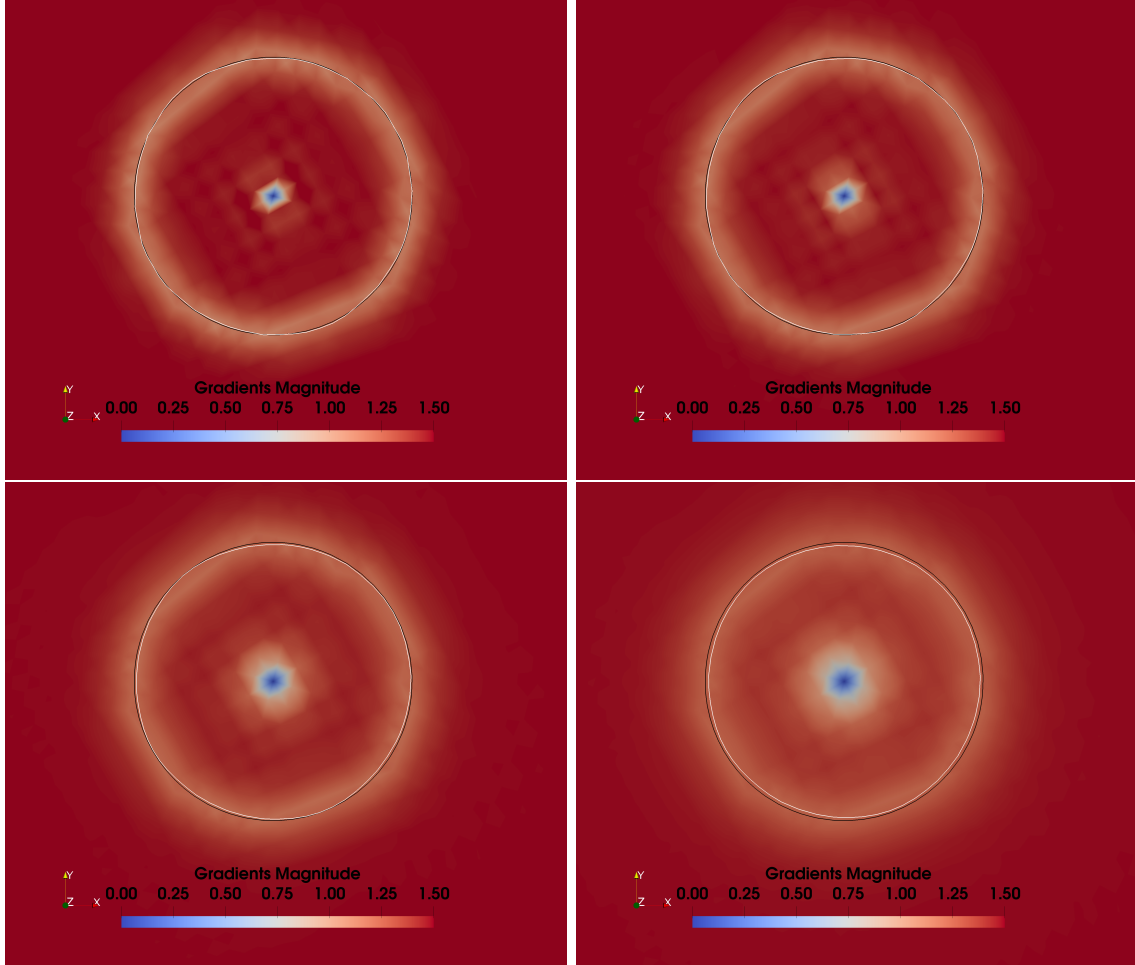
Figure A.10: Comparison of level set gradient according to the smoothing step on the level set function, redistancing step $\delta_r = h_T/100$, 50 iterations. From top left to bottom right: the smoothing step is successively set to $\delta_s = [h_T/1000, h_T/500, h_T/200, h_T/100]$. The black curve stands for the initial 0-curve whereas the white curve is the 0-curve of the redistanced and smoothed level set function.

A.3.4 Boundaries treatments

In the following section, a special geometry is set. This geometry - presented in figure A.11 - shows six sectors where for each, one hole is crossing the interior radius R_i and the other the exterior radius R_e.
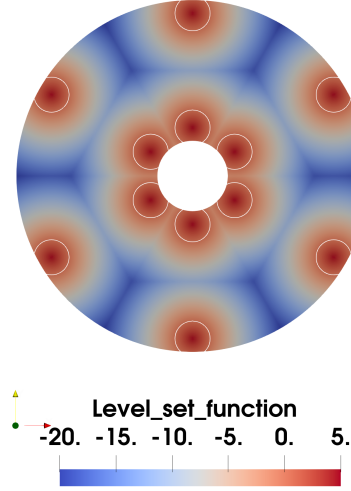
Figure A.11: Level set function for a ring drilled in 12 positions.

That representation only aims at showing the treatments of limit conditions on the boundaries R_i and R_e. Indeed, bad boundary conditions could have an undesired effect on a 0-curve crossing a domain boundary. Concerning the redistancing, two boundaries treatments must be done. First, a periodicity condition is imposed in the angular direction. Second, on R_i and R_e of the drilled ring, the treatment $|\nabla \psi(x)| = 1$ is applied and gives

$$D_r \psi(x) = \sqrt{1 - (D_\theta \psi(x))^2}, \ \forall x \in (r = R_i \text{ or } R_e, \theta).$$

As previously performed, we initialize in Figure A.12 the level set function with $|\nabla \psi(x)| = 1.5$ and we force its redistancing and smoothing.
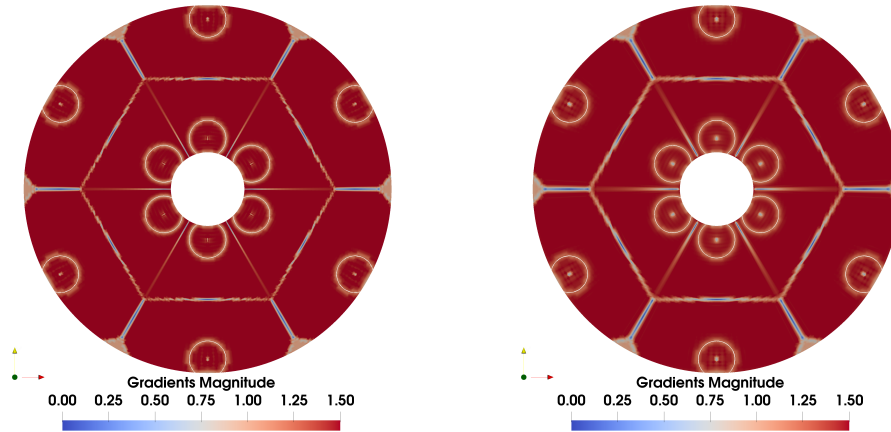
Figure A.12: Level set gradient initialised to $|\nabla \psi| = 1.5$. On the left: the level set is only redistanciated and on the right: the level set is redistanciated and smoothed. 50 iterations, redistancing step $\delta_r = h_T/100$, smoothing step $\delta_s = h_T/500$.

It is judicious to correctly deal with the boundaries conditions on the smoothing process, for the same reasons announced above for the redistancing. The matrix system solved in (A.4) is adjusted to impose correct boundary conditions. In that case, a Dirichlet condition is imposed on the inner and outer radii.

A.4   Conclusion

The level set function is easily treated thanks to the schemes introduced in this section. Its transport is efficient to convert the evolution of the geometry in the optimization process. The redistancing and smoothing steps prevent from the deprecation of the level set function quality although it extends the duration of the calculations. Another method could have been used, called the fast marching method (see for instance [90]). The Sethian's schemes adapted to a polar configuration are both used for the transport and the redistancing of the level set. They lead, for the redistancing stake, to a satisfying control of the level set function accuracy.

Bibliography

[1] R. Abgrall. Numerical discretization of the first-order hamilton-jacobi equation on triangular meshes. *Communications on pure and applied mathematics*, 49(12):1339–1373, 1996.

[2] R. A Adams and J. JF Fournier. *Sobolev spaces*. Elsevier, 2003.

[3] P. Alart and A. Curnier. A mixed formulation for frictional contact problems prone to Newton like solution methods. *Computer methods in applied mechanics and engineering*, 92(3):353–375, 1991.

[4] G. Allaire. *Conception optimale de structures*. Mathématiques et Applications. Springer Berlin Heidelberg, 2006.

[5] G. Allaire, C. Dapogny, and P. Frey. Topology and geometry optimization of elastic structures by exact deformation of simplicial mesh. *Comptes Rendus Mathematique*, 349(17-18):999–1003, 2011.

[6] G. Allaire, C. Dapogny, and P. Frey. A mesh evolution algorithm based on the level set method for geometry and topology optimization. *Structural and Multidisciplinary Optimization*, 48(4):711–715, 2013.

[7] G. Allaire, C. Dapogny, and P. Frey. Shape optimization with a level set based mesh evolution method. *Computer Methods in Applied Mechanics and Engineering*, 282:22–53, 2014.

[8] G. Allaire, F. Jouve, and A.-M. Toader. A level-set method for shape optimization. *Comptes Rendus Mathematique*, 334:1125–1130, 06 2002.

[9] G. Allaire, F. Jouve, and A.-M. Toader. Structural optimization using sensitivity analysis and a level-set method. *Journal of Computational Physics*, 194(1):363 – 393, 2004.

[10] A. Amassad, D. Chenais, and C. Fabre. Optimal control of an elastic contact problem involving Tresca friction law. *Nonlinear Analysis*, 48(8):1107–1135, 2002.

[11] N.V. Banichuk. Introduction to optimization of structures,(1990) p. 32-35.

[12] V. Barbu. Optimal control of variational inequalities. *Research Notes in Math.*, 100, 1984.

[13] J. Bonet and R. D. Wood. *Nonlinear continuum mechanics for finite element analysis.* Cambridge university press, 1997.

[14] Elie Bretin, Julien Chapelat, Pierre-Yves Outtier, and Yves Renard. Shape optimization of a linearly elastic rolling structure under unilateral contact using nitsche's method and cut finite elements. *Computational Mechanics*, pages 1–20, 2022.

[15] E. Burman and P. Hansbo. Edge stabilization for the generalized stokes problem: a continuous interior penalty method. *Computer methods in applied mechanics and engineering*, 195(19-22):2393–2410, 2006.

[16] E. Burman and P. Hansbo. Fictitious domain finite element methods using cut elements: I. a stabilized Lagrange multiplier method. *Computer Methods in Applied Mechanics and Engineering*, 199(41-44):2680–2686, 2010.

[17] E. Burman and P. Hansbo. Fictitious domain finite element methods using cut elements: Ii. a stabilized Nitsche method. *Applied Numerical Mathematics*, 62(4):328–341, 2012.

[18] J. Cea. Conception optimale ou identification de formes, calcul rapide de la dérivée directionnelle de la fonction coût. *ESAIM: Mathematical Modelling and Numerical Analysis - Modélisation Mathématique et Analyse Numérique*, 20(3):371–402, 1986.

[19] B. Chaudet-Dumas and J. Deteix. Shape derivatives for the penalty formulation of elastic contact problems with Tresca friction. *SIAM Journal on Control and Optimization*, 58(6):3237–3261, 2020.

[20] B. Chaudet-Dumas and J. Deteix. Shape derivatives for an augmented Lagrangian formulation of elastic contact problems. *ESAIM: Control, Optimisation and Calculus of Variations*, 27:S14, 2021.

[21] F. Chouly. An adaptation of Nitsche 's method to the Tresca friction problem. *Journal of Mathematical Analysis and Applications*, 411(1):329–339, 2014.

[22] F. Chouly, M. Fabre, P. Hild, R. Mlika, J. Pousin, and Y. Renard. An overview of recent results on Nitsche's method for contact problems. In *Geometrically unfitted finite element methods and applications*, pages 93–141. Springer, 2017.

[23] F. Chouly and P. Hild. A Nitsche-based method for unilateral contact problems: numerical analysis. *SIAM J. Numerical Analysis*, 51:1295–1307, 2013.

[24] F. Chouly, P. Hild, V. Lleras, and Y. Renard. Nitsche-based finite element method for contact with Coulomb friction. In *European Conference on Numerical Mathematics and Advanced Applications*, pages 839–847. Springer, 2017.

[25] F. Chouly, P. Hild, and Y. Renard. Symmetric and non-symmetric variants of Nitsche's method for contact problems in elasticity: theory and numerical experiments. *Mathematics of Computation*, 84(293):1089–1112, 2013.

[26] P. G. Ciarlet. *Three-dimensional elasticity.* Elsevier, 1988.

[27] U. Clarenz, U. Diewald, and M. Rumpf. *Anisotropic geometric diffusion in surface processing.* IEEE, 2000.

[28] M. Cocu. Existence of solutions of Signorini problems with friction. *International journal of engineering science*, 22(5):567–575, 1984.

[29] M. C. Delfour and J.-P. Zolésio. *Shapes and geometries: metrics, analysis, differential calculus, and optimization.* SIAM, 2011.

[30] B. Desmorat. Structural rigidity optimization with frictionless unilateral contact. *International Journal of Solids and Structures*, 44(3-4):1132–1144, 2007.

[31] J. Dolbow, N. Moës, and T. Belytschko. An extended finite element method for modeling crack growth with frictional contact. *Computer methods in applied Mechanics and engineering*, 190(51-52):6825–6846, 2001.

[32] G. Duvaut and J.-L. Lions. *Les inéquations en mécanique et en physique.* Dunod, 1972.

[33] C. Eck and J. Jarusek. Existence results for the static contact problem with Coulomb friction. *Mathematical Models and Methods in Applied Sciences*, 8(03):445–468, 1998.

[34] I. Ekeland and R. Temam. *Convex analysis and variational problems.* SIAM, 1999.

[35] M. Fabre, J. Pousin, and Y. Renard. A fictitious domain method for frictionless contact problems in elasticity using Nitsche's method. *The SMAI journal of computational mathematics*, 2:19–50, 2016.

[36] G. Fichera. Problemi elastostatici con vincoli unilaterali: il problema di Signorini con ambigue condizioni al contorno, atti acc. *Naz. Lincei, Memoria presentata il*, 1964.

[37] A. Fortin and A. Garon. Les éléments finis: de la théorie à la pratique. *Université Laval*, 2011.

[38] S. Geniaut, P. Massin, and N. Moës. A stable 3d contact formulation using x-fem. *European Journal of Computational Mechanics/Revue Européenne de Mécanique Numérique*, 16(2):259–275, 2007.

[39] R. Glowinski and P. Le Tallec. *Augmented Lagrangian and operator-splitting methods in nonlinear mechanics*. SIAM, 1989.

[40] M. E. Gurtin. *An introduction to continuum mechanics*. Academic press, 1982.

[41] J. Hadamard. *Mémoire sur le problème d'analyse relatif à l'équilibre des plaques élastiques encastrées*, volume 33. Imprimerie nationale, 1908.

[42] W. Han and M. Sofonea. *Quasistatic contact problems in viscoelasticity and viscoplasticity*. Number 30. American Mathematical Soc., 2002.

[43] J. Haslinger. Signorini problem with Coulomb's law of friction. shape optimization in contact problems. *International Journal for Numerical methods in engineering*, 34(1):223–231, 1992.

[44] J. Haslinger, I. Hlavácek, and J. Necas. Handbook of numerical analysis (eds. pg ciarlet and jl lions), vol. iv, 1996.

[45] J. Haslinger and A. Klarbring. Shape optimization in unilateral contact problems using generalized reciprocal energy as objective functional. *Nonlinear Analysis: Theory, Methods & Applications*, 21(11):815–834, 1993.

[46] J. Haslinger and R.A.E. Mäkinen. *Introduction to shape optimization: theory, approximation, and computation*. SIAM, 2003.

[47] J. Haslinger and P. Neittaanmäki. On the existence of optimal shapes in contact problems. *Numerical Functional Analysis and Optimization*, 7(2-3):107–124, 1985.

[48] J. Haslinger and P. Neittaanmäki. Shape optimization in contact problems. approximation and numerical realization. *ESAIM: Mathematical Modelling and Numerical Analysis*, 21(2):269–291, 1987.

[49] J. Haslinger and P. Neittaanmäki. *Finite element approximation for optimal shape, material, and topology design*. John Wiley & Sons, 1996.

[50] J. Haslinger, P. Neittaanmäki, and T. Tiihonen. Shape optimization in contact problems based on penalization of the state inequality. *Aplikace matematiky*, 31(1):54–77, 1986.

[51] J. Haslinger, J. V. Outrata, and R. Pathó. Shape optimization in 2D contact problems with given friction and a solution-dependent coefficient of friction. *Set-Valued and Variational Analysis*, 20(1):31–59, 2012.

[52] J. Haslinger and Y. Renard. A new fictitious domain approach inspired by the extended finite element method. *SIAM Journal on Numerical Analysis*, 47(2):1474–1499, 2009.

[53] P. Hauret and G. Noyel. Les mathématiques au service du pneumatique. *Centre de Technologies MICHELIN*, 2014.

[54] A. Henrot and M. Pierre. *Variation et optimisation de formes: une analyse géométrique*, volume 48. Springer Science & Business Media, 2006.

[55] A. Henrot and M. Pierre. *Shape variation and optimization*, volume 28 of *EMS Tracts in Mathematics*. European Mathematical Society (EMS), Zürich, 2018.

[56] P. Hild. Non-unique slipping in the Coulomb friction model in two-dimensional linear elasticity. *Quarterly Journal of Mechanics and Applied Mathematics*, 57(2):225–235, 2004.

[57] P. Hild. Multiple solutions of stick and separation type in the Signorini model with Coulomb friction. *ZAMM-Journal of Applied Mathematics and Mechanics/Zeitschrift für Angewandte Mathematik und Mechanik: Applied Mathematics and Mechanics*, 85(9):673–680, 2005.

[58] D. Hilding, A. Klarbring, and J. Petersson. Optimization of structures in unilateral contact. 1999.

[59] M. Hintermüller and A. Laurain. Optimal shape design subject to elliptic variational inequalities. *SIAM journal on control and optimization*, 49(3):1015–1047, 2011.

[60] J. Jarušek. Contact problems with bounded friction. coercive case. *Czechoslovak Mathematical Journal*, 33(2):237–261, 1983.

[61] N. Kikuchi and J. T. Oden. *Contact problems in elasticity: a study of variational inequalities and finite element methods*. SIAM, 1988.

[62] N. H. Kim, K. K. Choi, and J. S. Chen. Shape design sensitivity analysis and optimization of elasto-plasticity with frictional contact. *AIAA journal*, 38(9):1742–1753, 2000.

[63] N. H. Kim, K. K. Choi, and J. S. Chen. Structural optimization of finite deformation elastoplasticity using continuum-based shape design sensitivity formulation. *Computers & Structures*, 79(20-21):1959–1976, 2001.

[64] N. H. Kim, Y. H. Park, and K. K. Choi. Optimization of a hyper-elastic structure with multibody contact using continuum-based shape design sensitivity analysis. *Structural and multidisciplinary optimization*, 21(3):196–208, 2001.

[65] T. A. Laursen. *Computational contact and impact mechanics: fundamentals of modeling interfacial phenomena in nonlinear finite element analysis.* Springer Science & Business Media, 2003.

[66] J.-L. Lions and P. Lelong. *Contrôle optimal de systèmes gouvernés par des équations aux dérivées partielles*, volume 1. Dunod Paris, 1968.

[67] B. S. Massey. *Measures in science and engineering: their expression, relation and interpretation.* Ellis Horwood, 1986.

[68] A. Maury. *Shape optimization for contact and plasticity problems thanks to the level set method.* PhD thesis, Université Pierre et Marie Curie-Paris VI, 2016.

[69] A. Maury, G. Allaire, and F. Jouve. Shape optimisation with the level set method for contact problems in linearised elasticity. *The SMAI journal of computational mathematics*, 3:249–292, 2017.

[70] F. Mignot. Contrôle dans les inéquations variationelles elliptiques. *Journal of Functional Analysis*, 22(2):130–185, 1976.

[71] R. Mlika, Y. Renard, and F. Chouly. An unbiased Nitsche's formulation of large deformation frictional contact and self-contact. *Computer Methods in Applied Mechanics and Engineering*, 325:265–288, 2017.

[72] N. Moës, J. Dolbow, and T. Belytschko. A finite element method for crack growth without remeshing. *International journal for numerical methods in engineering*, 46(1):131–150, 1999.

[73] M. Mooney. A theory of large elastic deformation. *Journal of applied physics*, 11(9):582–592, 1940.

[74] F. Murat and J. Simon. Étude de problèmes d'optimal design. In *IFIP Technical Conference on Optimization Techniques*, pages 54–62. Springer, 1975.

[75] F. Murat and L. Tartar. Calcul des variations et homogénisation,(french)[calculus of variation and homogenization]. *Les méthodes de l'homogénéisation: théorie et applications en physique*, 57:319–369, 1985.

[76] I. Nistor, M.L.E. Guiton, P. Massin, N. Moës, and S. Geniaut. An x-fem approach for large sliding contact along discontinuities. *International Journal for Numerical Methods in Engineering*, 78(12):1407–1435, 2009.

[77] J. Nitsche. Über ein variationsprinzip zur lösung von Dirichlet-problemen bei verwendung von teilräumen, die keinen randbedingungen unterworfen sind. *Abhandlungen aus dem Mathematischen Seminar der Universität Hamburg*, 36:9–15, 1971.

[78] R. W. Ogden. *Non-linear elastic deformations*. Courier Corporation, 1997.

[79] S. J. Osher and Sethian J. A. Fronts propagating with curvature-dependent speed: Algorithms based on Hamilton-Jacobi formulations. *Journal of Computational Physics*, 79(1):12 – 49, 1988.

[80] S. J. Osher and F. Santosa. Level set methods for optimization problems involving geometry and constraints: I. frequencies of a two-densityinhomogeneous drum. *Journal of Computational Physics*, 171:272–288, 2001.

[81] I. Páczelt and T. Szabó. Optimal shape design for contact problems. *Structural optimization*, 7(1-2):66–75, 1994.

[82] S. Patankar. Numerical heat transfer and fluid flow, ser. *Coputational Methods Mech. Therm. Sci*, pages 1–197, 1980.

[83] O. Pironneau. Optimal shape design for elliptic systems. In *System Modeling and Optimization*, pages 42–66. Springer, 1982.

[84] K. Poulios and Y. Renard. An unconstrained integral approximation of large sliding frictional contact between deformable solids. *Computers & Structures*, 153:75–90, 2015.

[85] Y. Renard. A uniqueness criterion for the Signorini problem with Coulomb friction. *SIAM journal on mathematical analysis*, 38(2):452–467, 2006.

[86] Y. Renard. Generalized Newton's methods for the approximation and resolution of frictional contact problems in elasticity. *Computer Methods in Applied Mechanics and Engineering*, 256:38 – 55, 2013.

[87] Y. Renard and K. Poulios. GetFEM: Automated FE modeling of multiphysics problems based on a generic weak form language. *Transactions on Mathematical Software*, 47:1, 2020.

[88] R. S. Rivlin. Large elastic deformations of isotropic materials iv. further developments of the general theory. *Philosophical Transactions of the Royal Society of London. Series A, Mathematical and Physical Sciences*, 241(835):379–397, 1948.

[89] G. C. Sekhar, B. Anjaneyulu, KK. Rao, and G N. Rao. Design and analysis of four wheeler airless tire. *International Journal of Engineering Science*, 6:3365–3379, 2016.

[90] J. A. Sethian. Fast marching methods. *SIAM review*, 41(2):199–235, 1999.

[91] J. A. Sethian. *Level set methods and fast marching methods: evolving interfaces in computational geometry, fluid mechanics, computer vision, and materials science*, volume 3. Cambridge university press, 1999.

[92] J. A. Sethian and A. Wiegmann. Structural boundary design via level set and immersed interface methods. *Journal of computational physics*, 163(2):489–528, 2000.

[93] J. Simon. Differentiation with respect to the domain in boundary value problems. *Numerical Functional Analysis and Optimization*, 2(7-8):649–687, 1980.

[94] J. Sokolowski and J.-P. Zolesio. Dérivée par rapport au domaine de la solution d'un problème unilatéral. *CR Acad. Sc. Paris*, 301(4):103–106, 1985.

[95] J. Sokolowski and J.-P. Zolésio. Shape sensitivity analysis of unilateral problems. *SIAM journal on mathematical analysis*, 18(5):1416–1437, 1987.

[96] J. Sokolowski and J.-P. Zolesio. Shape sensitivity analysis of contact problem with prescribed friction. *Nonlinear Analysis: Theory, Methods & Applications*, 12(12):1399–1411, 1988.

[97] J. Sokolowski and J.-P. Zolésio. Introduction to shape optimization. In *Introduction to Shape Optimization*, pages 5–12. Springer, 1992.

[98] J. Sokolowski and J.-P. Zolesio. Shape sensitivity analysis of variational inequalities. In *Introduction to Shape Optimization*, pages 163–239. Springer, 1992.

[99] J. Sokolowski and J.-P. Zolesio. Differential stability of solutions to unilateral problems. *Free boundary problems: application and theory*, 4:537–547, 1993.

[100] N. Strömberg and A. Klarbring. Topology optimization of structures with contact constraints by using a smooth formulation and nested approach. 2009.

[101] N. Strömberg and A. Klarbring. Topology optimization of structures in unilateral contact. *Structural and Multidisciplinary Optimization*, 41(1):57–64, 2010.

[102] S. Stupkiewicz, J. Lengiewicz, and J. Korelc. Sensitivity analysis for frictional contact problems in the augmented Lagrangian formulation. *Computer methods in applied mechanics and engineering*, 199(33-36):2165–2176, 2010.

[103] A. Suhag and R. Dayal. Static analysis on custom polyurethane spokes of airless tire. *International Journal of Scientific and Research Publications*, 3(11):2250–315, 2013.

[104] M. Sussman, P. Smereka, and S. J. Osher. A level set approach for computing solutions to incompressible two-phase flow. *Journal of Computational Physics*, 114(1):146–159, 1994.

[105] L. Tartar. An introduction to the homogenization method in optimal design. *Optimal shape design*, pages 47–156, 2000.

[106] A. Touzaline. Optimal control of a frictional contact problem. *Acta Mathematicae Applicatae Sinica, English Series*, 31(4):991–1000, 2015.

[107] B. Wohlmuth. Variationally consistent discretization schemes and numerical algorithms for contact problems. *Acta Numerica*, 20:569–734, 2011.

[108] P. Wriggers. Computational contact mechanics. *Computational Mechanics*, 32(1-2):141–141, 2003.

THESE DE L'UNIVERSITE DE LYON OPEREE AU SEIN DE L'INSA LYON

NOM : CHAPELAT   DATE de SOUTENANCE : 16/12/2022
(avec précision du nom de jeune fille, le cas échéant)

Prénoms : Julien, Antoine, Paul

TITRE : Optimisation de forme multi-critère d'une structure non-linéaire complexe

NATURE : Doctorat   Numéro d'ordre : 2022ISAL0118

Ecole doctorale : MEGA (Mécanique, Energétique, Génie Civil, Acoustique)

Spécialité : Génie Mécanique

RESUME : Les pneumatiques sans air sont des structures complexes dont le comportement fait intervenir différentes physiques. Afin de proposer une conception performante, la géométrie d'un pneumatique sans air et les matériaux qui composent une telle structure font l'objet de choix de recherche rigoureux. Différentes innovations ont marqué l'histoire du pneumatique, et ce à différentes échelles : de l'échelle microscopique concernant l'adhérence et la réponse thermique de la bande de roulement à une échelle macroscopique concernant la réponse vibratoire et mécanique de la structure. A cette dernière macro-échelle, les concepteurs ont particulièrement étudié la réponse élastique du pneumatique sans air pour guider au mieux le véhicule le long de sa trajectoire. Différents outils de conception existent afin d'obtenir le meilleur compromis de performances, et en particulier, des stratégies d'optimisation de forme.
Dans notre cas particulier, nous développons l'optimisation de forme dite géométrique dans le contexte de l'élasticité. Nous proposons une méthode de gradient afin de minimiser des critères de performance. Cependant, différents aspects peuvent faire rendre l'optimisation difficile comme par exemple des non linéarités. Nous développons la complexité liée à la condition de contact entre le pneumatique sans air et le sol. En effet, cette condition introduit une non linéarité dans le problème mécanique. Le contact est approximé par la méthode de Nitsche, méthode consistante et qui ne nécessite pas l'ajout de multiplicateurs de Lagrange. Ainsi, nous étudions l'optimisation de forme géométrique à travers une formulation du problème élastique utilisant la méthode de Nitsche. La condition de contact introduit également une non différentiabilité au sens classique dans le problème d'optimisation. Une notion plus faible de la différentiabilité permet d'assurer la formulation de dérivées de forme des critères d'optimisation, et ainsi d'assurer le bon fonctionnement de la méthode de gradient. Par ailleurs, le pneumatique sans air est largement sollicité en grandes déformations, ce qui introduit de nouvelles non linéarités. Ainsi la stratégie d'optimisation de forme est présentée d'abord dans le cadre de l'élasticité linéaire afin de présenter les outils mis en place et d'analyser la sensibilité de forme permettant d'assurer l'existence de dérivées de forme. Ensuite l'étude de forme est étendue aux grandes déformations pour traiter des applications plus réalistes.

MOTS-CLÉS : optimisation de forme, contact unilatéral, méthode de Nitsche, level set, hyperélasticité, domaines fictifs

Laboratoire de recherche : LaMCoS, INSA Lyon, Université de Lyon

Directeur de thèse: Yves RENARD, Elie BRETIN

Président de jury :

Composition du jury : Nicolas MOËS, François JOUVE, Vanessa LLERAS, Eric BONNETIER, Yves RENARD, Elie BRETIN, Thomas HOMOLLE, Charlie DOUANLA-L.